THESIS FOR THE DEGREE OF LICENTIATE OF ENGINEERING

Alloys in Contact with Molten Salts for Thermal Storage Applications

ESRAA HAMDY MOHAMEDIN

Department of Chemistry and Chemical Engineering

CHALMERS UNIVERSITY OF TECHNOLOGY

Gothenburg, Sweden 2021

Alloys in Contact with Molten Salts for Thermal Storage Applications

ESRAA HAMDY MOHAMEDIN

Technical report no 2021:23

Department of Chemistry and Chemical Engineering
Chalmers University of Technology
SE-412 96 Gothenburg
Sweden
Telephone + 46 (0)31-772 1000

Cover: *Left*; Overall mass change behaviour of five alumina forming alloys immersed in alkali carbonate melt at 800 °C as a function of exposure time. *Centre*; Assembly of top-view, and cross-section SEM images of Kanthal® EF 101 in contact with alkali carbonate melt at 800 °C. *Top left*; XRD patterns of Kanthal® EF 101 after exposure to alkali carbonate melt at 800 °C. *Top right*; 3D polyhedral visualisation of α-and γ-$LiAlO_2$ crystal structures.

Chalmers Reproservice
Gothenburg, Sweden 2021

Abstract

The combination of a concentrated solar power (CSP) plant and a thermal energy storage (TES) system is a promising technology for power generation, in that it overcomes the challenges commonly faced by renewable energy systems, such as intermittency, dispatchability, and the gap between the energy supply and energy demand. The third generation (Gen3) CSP plants are designed to increase plant efficiency by using supercritical carbon dioxide (sCO_2) instead of steam for the Brayton cycle gas turbines, requiring a minimum operating temperature of 750°C for the TES materials. Operating the TES tanks at higher temperatures poses a serious challenge in terms of corrosion for the metallic tank components and risks catastrophic failure of the plant. This study aims to provide useful insights into the corrosion behaviour of metallic materials that come in contact with different salt melts.

The first part of this licentiate thesis is a comparative study of the corrosion resistance of chromia forming (316H or 304L) vs alumina forming (Kanthal® APMT) alloys that were exposed to three salt melts chosen for the current and next-generation CSP plants. The following salt melts were selected: Solar Salt, which is a commercial binary nitrate salt mixture that is utilised in currently operating CSP plants; a ternary carbonate; and a binary chloride salt mixture, which are candidate TES media for the Gen3 CSP technology. Corrosion exposures were conducted at 650 °C for the nitrate experiments and 800 °C for the carbonate and chloride experiments. The corrosion assessments of the tested alloys focused on oxidation, dissolution, and internal attack.

The main findings revealed that:

1) for nitrate exposures: alloy 316H and Kanthal® APMT showed good corrosion resistance in contact with the nitrate melts, even though an internal attack was detected on the chromia forming 316H alloy; this attack was relatively slow and predictable. The relatively good corrosion behaviour of the alloys in nitrate melt is partly due to the lower operating temperature compared to the carbonate and chloride exposures.

2) for chloride exposures: both 304L and Kanthal® APMT underwent rapid degradation upon exposure to chloride melt. The degradation of these materials is caused by leaching of elements, such as chromium and aluminium. Nonetheless, molybdenum in Kanthal® APMT affected the corrosion process by forming a Laves phase barrier to chromium leaching; however, this did not prevent the rapid leaching of aluminium from the alloy.

3) for carbonate exposures: alloys in contact with the carbonate melt behaved differently based on the type of oxide scale formed. The stainless steel 304L showed the poorest corrosion resistance among all tested alloys in the three melts, wherein severe carburisation was detected. In strong contrast to 304L, Kanthal® APMT showed good corrosion resistance because it formed a thin protective layer of α-$LiAlO_2$, which makes it a promising candidate for Gen3 CSP plants. After 168 h of exposure, a phase transition from $\alpha \rightarrow \gamma$-$LiAlO_2$ oxide scale was observed.

The second part of this thesis is dedicated to ranking five alumina-forming alloys in contact with alkali carbonate melt at 800 °C up to 1000 h. Four ferritic FeCrAl alloys: Kanthal® APMT, Kanthal® AF, Kanthal® EF 100, and Kanthal® EF 101, and one austenitic FeNiCrAl alloy, Nikrothal® PM58 were investigated in this study. All four ferritic alumina-forming alloys developed a thin, protective α-$LiAlO_2$ scale. The thermodynamically stable γ-$LiAlO_2$ nucleates on top of the α-$LiAlO_2$ scale and forms non-protective crystals. However, no severe aluminium depletion was detected for at least 1000 h. The austenitic Nikrothal® PM58 did not form a α-$LiAlO_2$ scale at 800 °C due to the relatively slow diffusion of aluminium from the alloy towards the alloy/melt interface.

Keywords: High-temperature corrosion; Alumina-forming alloys; Molten salts; Carburisation; Laves phase; Phase transition; Concentrated solar power (CSP); Thermal energy storage (TES)

List of publications

Paper I (a)

Hamdy, E., Nockert-Olovsjö, J., and Geers, C., *Perspectives on selected alloys in contact with eutectic melts for thermal storage: Nitrates, carbonates and chlorides.* Solar Energy, 2021. **224**: p. 1210-1221.

Paper I (b)

Hamdy, E., Nockert-Olovsjö, J., and Geers, C., *Additional data and experimental setups used for the study on alloys in contact to high temperature eutectic melts for thermal storage* Data in Brief, 2021: p. 107446.

Paper II

Hamdy, E., Strach, M., Nockert-Olovsjö, J., and Geers, C., *Differentiation in corrosion performance of alumina forming alloys in alkali carbonate melts.* Corrosion Science, 2021: p. 109857.

Statement of the authors' contributions

Paper I (a, b)

Esraa Hamdy: the principal author, conducted most of the exposure experiments, and sample analyses, improved setup design; **Johanna Nockert Olovsjö:** sample material advisor and supplier of Kanthal APMT, co-authored these articles; **Christine Geers**: conducted some of the exposure experiments and sample analyses, improved setup design, did the thermodynamic calculations, co-authored these articles.

Paper II:

Esraa Hamdy: the principal author, did the experimental work, and sample analyses; **Johanna Nockert Olovsjö:** Sample material advisor and main project partner for materials supplying at Kanthal, co-authored this article; **Michal Strach**: used Rietveld refinement method, TOPAS V6 software, α/γ-$LiAlO_2$ phase fraction calculations, co-authored the article. **Christine Geers**: conducted some of the sample analyses, co-authored the articles.

Acknowledgements

It is, and it will always be a pleasure to thank many people who made this work possible.

I would like gratefully to acknowledge the guidance of my supervisor, Dr. Christine Geers, who had been abundantly helpful, caring and had assisted me in numerous ways, not only during this point of research but throughout my stay in Sweden. I am happy to express my profound sense of gratitude for her guidance and support.

I would like also to thank my supervisor Prof. Jan-Erik Svensson, and my examiner Prof. Lars-Gunnar Johansson for giving me the opportunity to work on this project and be part of the High Temperature Corrosion Centre.

I also convey my gratitude to my co-authors, Johanna Nockert Olovsjö, and Dr. Michal Strach for their valuable inputs, suggestions and meticulous revisions that benefited much in completing this work.

I am very grateful to Prof. Jan Froitzheim and Itai Panas, my directors of studies, for their support, guidance, and encouragement.

I would like to extend my sincere thanks to our administrators Sandra Nayeri and Anna Oskarsson for their continuous help since I moved to Sweden. I would also like to thank our financial administrator Christina Anderson.

Special thanks go to Esa Väänänen, our talented research engineer who built the experimental set-ups used in this work. I would like to thank him for his enthusiasm and eagerness to solve challenges brought by the molten salts' experiments.

My thanks extend to my former and current officemates Dr. Özgür Gündüz, Dr. Claudia Göbel, Camilla Cossu, and Hampus Lindmark, thanks for your indefinite support.

I wish also to express my deepest gratitude to Mareddy Reddy, Dr. Alberto Visibile, Dr. Duygu Yilmaz and Luca Gagliani for their continuous motivation, endless cooperation, and true concern to accomplish this work. And to all my colleagues in OOMK1 & OOMK2, thanks for creating a positive working environment.

I would also like to thank our caretakers Fatima Joof and Kent Johansson, for their helpful advice about life in Sweden and the very nice conversations.

For Zeinab, Moufida, Rosa, Muwada, Amal, Lujain, Hanaa, Alaa, Sheetal and all my dear friends in Sweden, thanks for being my surrogate family and always being there for me whenever I need you.

My final words go equally to my family, especially my sweet parents, Faiza & Hamdy, whom I want to thank for their unconditioned love and guidance in whatever I pursue, and for their substantial moral support and infinite warmth and tenderness. Words are very few to express enormous humble thanks to them.

I would like to thank the Swedish Energy Agency for funding this work through thermal storage for SOLEL initiative under contract number 44653-1 and as a partner in the High Temperature Corrosion Competence Centre.

Table of Contents

1 Introduction

1.1 Background

In 2021, the Intergovernmental Panel on Climate Change (IPCC) published the first part of the *Sixth Assessment Report on Climate Change*. This report summarises the current climate situation and the role of humans in climate change. Since about 1750, human activities have been responsible for the observed increase in the concentrations of well-mixed greenhouse gases (GHGs). This increase in GHGs, especially in the last four decades, has warmed the climate at a rate that has not been witnessed for at least 2,000 years. Human-induced climate change has most likely induced changes in the weather patterns in almost all regions of the world, in addition to causing droughts, heatwaves, and tropical cyclones [1]. Therefore, it has become necessary to reduce these harmful GHGs. In 2015, 196 countries agreed at COP21 in Paris to limit global warming by taking serious steps and adopting strategies to reduce GHG emissions [2].

Most of the world's energy supply is provided by fossil fuels. Since 1900, the burning of fossil fuels has increased dramatically, resulting in high levels of CO_2 emissions [1, 3]. In contrast, renewable energy sources, such as solar and wind energy, have almost no CO_2 emissions. Therefore, the use of renewable energy provides a solution for reducing emissions of GHGs [3]. Concentrated solar power (CSP) plant is considered an interesting technology that utilises the sun, a clean, abundant, and inexhaustible energy source [4]. Two major technologies can be used for electrical power generation from solar energy: photovoltaic (PV) and CSP. Even though PV can be combined with batteries, in which electrical energy is stored as chemical energy, CSP is superior to PV due to its longer storage duration and better dispatchability at large scale [5, 6]. However, there is a growing need to increase the efficiency levels of CSP plants, to make them cost-competitive in relation to PV and have a higher penetration of the energy market.

Third-generation (Gen3) CSP plants are designed to increase the plant's efficiency by using supercritical carbon dioxide (sCO_2) instead of steam for the Brayton cycle gas turbines. This requires a minimum operating temperature of 750°C for the thermal energy storage (TES) materials [7-11]. The higher operating temperatures entail serious challenges in terms of the thermal stability of the respective heat transport medium and the resilience of the metal components to high-temperature corrosion. Thus, corrosivity is a major obstacle to be overcome on the path to empowering the first Brayton cycle-operated CSP plant [12, 13]. In this licentiate study, various alumina forming alloys of which some have just recently been commercialised were investigated and compared with common stainless steel alloys. The selected alloys were exposed to commercial nitrate melt and carbonate and chloride salt mixtures as potential TES material candidates for the next generation of CSP plants.

Corrosion by salt species at high temperatures is certainly not a new issue in the field. However, depending on the choice of commercial alloy, the longevity and safety of a plant module can be substantially impacted. A chemical and microstructural understanding of the reasons for differences in performance of the alloys was the goal of this licentiate study.

A novel laboratory setup was built to mimic the corrosive environment in TES hot tanks. The first part of this thesis investigates the differences in corrosivity between an alkali nitrate melt, which is known as Solar Salt and is currently used in commercial CSP plants [14], and alkali carbonate and chloride salt melts, which are potential TES materials for the Gen3 CSP plants. The experiments were conducted at temperatures that exceeded by 50°–100°C those required in the power plants. The higher exposure temperature was used to accelerate corrosion and ensure the stability levels of the metallic materials in case of heat fluctuations in the hot storage tank, receivers, and piping. The corrosion resistances in the aforementioned salt melts of the chromia-forming alloys 316H/304L and the alumina-forming alloy Kanthal® APMT were investigated.

The second part of this licentiate thesis is dedicated to evaluating the α/γ-$LiAlO_2$ transition observed during the first carbonate exposures and providing a corrosion performance ranking for the five alumina-forming alloys in the carbonate melt. Four ferritic FeCrAl alloys were tested in this study, Kanthal® APMT, Kanthal® AF, Kanthal® EF 100, and Kanthal® EF 101, as well as the austenitic FeNiCrAl Nikrothal® PM58. The corrosion exposures were conducted isothermally at 800°C and for up to 1000 h.

1.2 Concentrated Solar Power Plant Technology

Despite the fact that the CSP technology dates back to the 1970s, the majority of the commercial CSP plants have only been established in the last decade [2–4]. In the International Energy Agency (IEA) report, the CSP technology could contribute 11.3% of the world's electricity by Year 2050, assuming appropriate support [15]. However, the CSP technology is still not cost-competitive with other power generation technologies. To remedy this, the US Department of Energy (DOE) launched the SunShot Initiative roadmap in 2011, with a cost target of 6 ¢/kWh for electricity from CSP plants [14]. Reaching this goal necessitates increasing the plant's efficiency, thereby improving the performances of different CSP plant components. Before discussing the proposed approaches by the SunShot Initiative to achieve the 6 ¢/kWh cost target, an overview of how the CSP plant works is provided below.

The CSP plant is schematically illustrated in Figure 1.1. The CSP system comprises thousands of mirrors (heliostats) to track, concentrate, and reflect the solar radiation to the focal point located in a tower receiver, wherein the solar radiation is converted into thermal energy. A heat transfer fluid (HTF), also known as thermal energy storage (TES) material, is pumped into the top of the tower receiver to capture the solar radiation and collect it in the form of heat. The heat collected by the HTF is either used directly to generate electricity or transported and stored in the hot TES tank until electricity is required. When there is a demand for electrical power, the stored heat in the hot tank is used to drive a turbine, e.g., through steam or supercritical carbon dioxide, so as to drive a generator and produce electricity [4].

Since heat storage is one of the distinct advantages of the CSP technology, considerable efforts have been exerted to study materials that can act as the HTF or TES medium. The different TES storage media are classified as: i) *sensible heat storage*, where the amount of stored heat depends on the temperature, quantity of the employed TES material and its specific heat capacity without any phase change; ii) *latent heat or phase-change materials*, where thermal energy is stored during a phase change; and iii) *thermochemical heat storage*, where energy is stored/dispatched via a reversible thermochemical reaction. Despite the high storage capacity of the latent heat and thermochemical TES forms, currently active commercial plants employ sensible storage capacity due to its easier operation conditions and lower complexity level of the system [16].

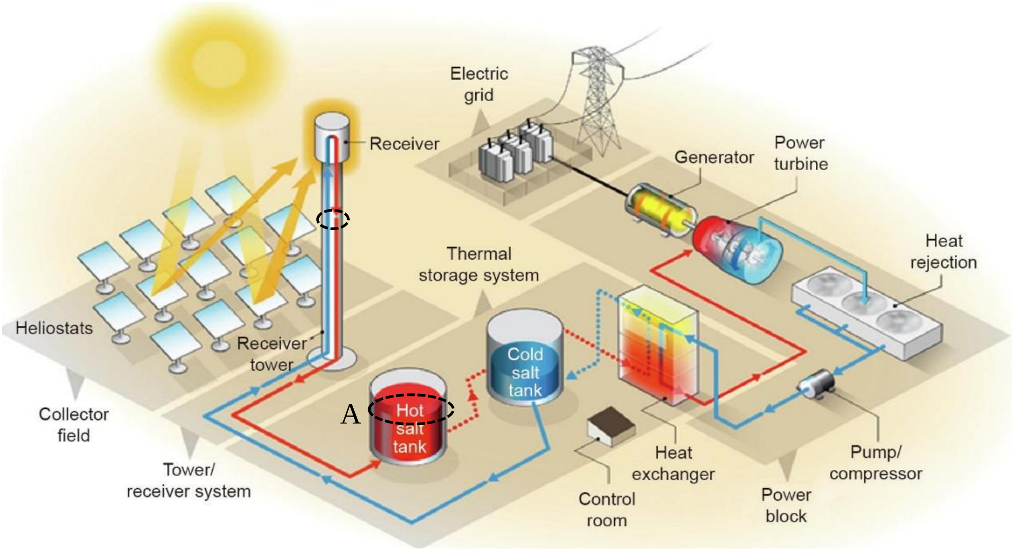

Figure 1.1 Schematic diagram illustrating components of concentrated solar power plant [14, 17].
Source: US Department of Energy Report: The Year of Concentrating Solar Power, DOE/EE-1101, May 2014.

The SunShot Initiative roadmap proposes three pathways to achieve the 6 ¢/kWh cost target and an increase in CSP plant efficiency. One of the presented approaches is to utilise sCO_2 Brayton cycle systems instead of the steam-Rankine cycle systems that are commonly used in CSP and other plants. At temperatures ≥ 700°C, the sCO_2 Brayton cycle can achieve the required heat-to-power conversion efficiency of > 50%. Pushing the operation limits of the CSP plants necessitates the use of a TES material that can function at temperatures ≥750° C [7-11].

Numerous studies have investigated TES materials for their potential to operate at such high temperatures (for reviews, see [16, 18-20]). The TES materials employed in the currently active commercial CSP plants are nitrate melts, among other commercial mixtures used. A eutectic salt mixture of (60 wt% $NaNO_3$, 40 wt% KNO_3) known as Solar Salt

A eutectic system is a homogenous mixture of two or more components that has a lower melting point than the respective pure substances at a particular ratio between the components. This temperature is called “the eutectic temperature”, E, (see Figure 1.2) [21]. For instance the T_m for pure KNO_3 is 334 °C and T_m for pure $NaNO_3$ is 308 °C while their eutectic mixture already melts at 230 °C [14].

Solar salt has been selected for its favourable thermophysical properties, e.g., melting temperature, thermal storage capacity, thermal conductivity, density, vapour pressure, stability, and corrosivity. However, alkali nitrates are unsuitable for utilisation at temperatures above 550°C due to decomposition.

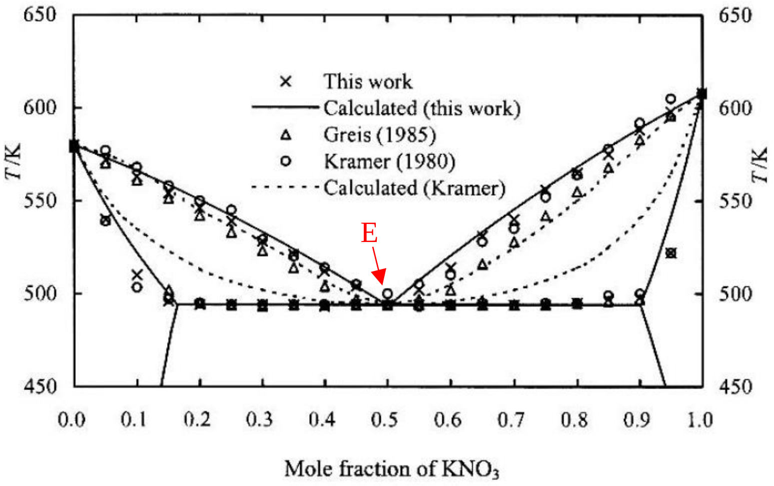

Figure 1.2. Schematic phase diagram of binary $NaNO_3$-KNO_3 eutectic system [22], where E is eutectic temperature. Source: Zhang, X., et al., Thermodynamic evaluation of phase equilibria in $NaNO_3$-KNO_3 system, 2003. Reproduced with permission from the Journal of Phase Equilibria.

Since the Gen3 CSP plants require higher operating temperatures, other potential TES materials have been investigated. Two of the most commonly proposed TES candidates are a ternary carbonate mixture (32.1 wt% Li_2CO_3 -33.4 wt% Na_2CO_3- 34.5 wt% K_2CO_3) and a binary chloride mixture (64.4 wt% KCl- 35.6% wt% $MgCl_2$). These salt mixtures differ in terms of cost, abundance, thermal stability, liquidus temperature range, and corrosivity [12, 14, 18].

Increasing the temperature of salt melts also increases their corrosivity towards metallic materials. Therefore, a significant improvement in the compatibility between the container material (tanks/pipes/heat exchangers) and the TES medium is necessary [13, 14]. Corrosion of the metallic materials in contact with the storage medium can lead to catastrophic failure of an entire CSP plant due to material loss or embrittlement.

This licentiate thesis focuses on investigating the corrosion of hot storage tank materials by salt melts (see Figure 1.1). The first part of the *Results* chapter describes the corrosion behaviour of different FeNiCr and FeCrAl alloys in alkali nitrate, carbonate, and chloride salt melts. The second part evaluates the corrosion resistance levels of five alumina-forming alloys that are in contact with promising TES materials at 800°C.

Since the corrosion of metal components in contact with molten salts is a critical aspect of the CSP technology, the following chapters present an overview of high-temperature corrosion in general, and molten salt corrosion in particular.

2 High-Temperature Corrosion and Oxidation

High-temperature corrosion is defined as the thermodynamically driven degradation of materials at temperatures ≥ 400 °C. At high temperatures, metallic materials are at risk from degradation processes, such as oxidation, nitridation, carburisation, chlorination, and hot corrosion [23]. The inclusion of high-temperature oxidation in this context of corrosion is debatable, since protective oxide layers are used to prevent other corrosive species from reacting with an alloy.

2.1 Oxide Scale

The term "oxidation of metals" is mostly used to describe the interactions of metal with the surrounding oxygen in the environment, to form a metal oxide scale. As shown in Figure 2.1, the oxide scale is initially formed by the adsorption of oxygen to the metal surface and oxygen reduction by electrons from the alloy elements to form O^{2-}. When oxide ions and metal cations occupy their respective lattice positions at the metal/gas interface, the oxide scale nucleates and grows laterally until it covers the entire metal surface. Oxide scale growth can proceed outwards through metal ion transport to cationic vacancies adjacent to the adsorbed oxygen ions or inwards when oxygen ions occupy the oxygen vacancies formed at the alloy/oxide interface [24]. These principles have been described and established by Carl Wagner [25].

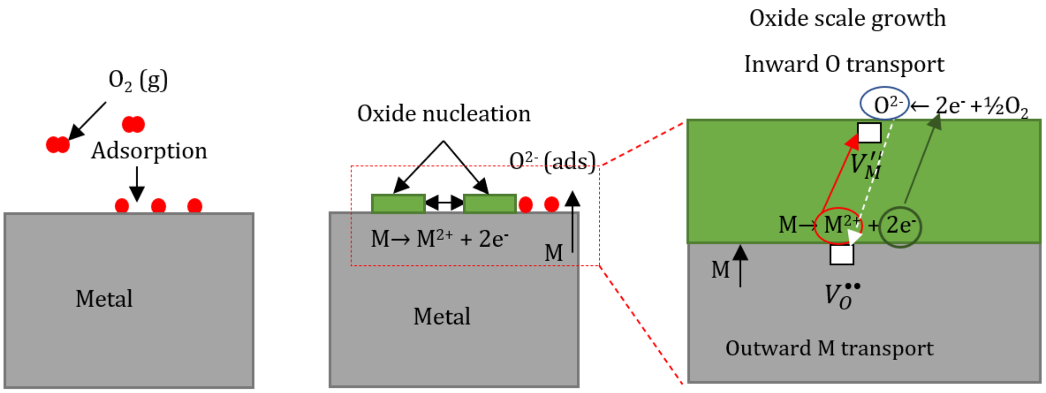

Figure 2.1 Oxide scale formation process, where $V_O^{\bullet\bullet}$ *is an oxygen vacancy and* V_M'' *is a metal vacancy.*

The oxide scale is considered beneficial because it acts as a corrosion-resistant barrier that prevents the surrounding environment from interacting with the metal. For an oxide scale to be protective, it needs to have the following characteristics: slow-growing, dense, continuous, well-adherent, and inert to reactions with the environment, such as dissolution [26].

Understanding which types of corrosion products can form as a result of high-temperature oxidation of the alloy is essential. These products include an outer scale that acts as a protective barrier against the corrosive environment. In several studies, pre-oxidation has been applied to form a protective layer to protect against more-aggressive chemical species, such as attack by molten salts [27-30].

The following sections present an overview of the thermodynamics, kinetics, and growth of the oxide scale. Certain basic concepts apply to all high-temperature corrosion processes: a sequence of spontaneous processes; electrochemical coupling of metal with the environment; and increasing entropy with increasing temperature [23, 26, 31].

2.2 Thermodynamics and Kinetics

Equation (2.1) describes the oxidation of a single metal when exposed to oxygen:

$$xM(s) + \frac{y}{2}\, O_2(g) \leftrightharpoons M_xO_y(\boldsymbol{s}, l, g) \qquad (2.1)$$

where *M* is the exposed metal and *x* and *y* are the stoichiometric constants. To form an oxide scale, only solid oxides are relevant.

Many factors influence the oxide scale formation, such as temperature, the alloy chemistry, exposure time, and the oxygen partial pressure $p(O_2)$ in the environment. To determine the comparative stabilities of metal oxide species at different temperatures, the second law of thermodynamics is used in terms of Gibbs free energy, assuming that the temperature and pressure are constant. It is important to mention that there is a minimum value of $p(O_2)$ for oxidation at each temperature. If this value is not reached, the metal remains in metallic form.

$$\Delta G = \Delta H - T\Delta S \qquad (2.2)$$

where *G* is the Gibbs free energy of the system, *H* is the enthalpy, *T* is the absolute temperature, and *S* is the entropy. When the ΔG of a reaction of a metal with oxygen in our case is <0 the reaction is thermodynamically favourable and occurs spontaneously, the oxide is stable. Whereas, when the ΔG of the system is >0 the reaction is thermodynamically unfavourable, and the metal remains metallic. If ΔG=0 the system is in at equilibrium.

The Gibbs free energy for Eq. (2.2) per mole of oxygen can be written as follows:

$$\Delta G = \Delta G° + RTIn(\frac{a\ (MxOy)}{a_M^x \cdot p_{O2}^{y/2}}) \qquad (2.3)$$

where $\Delta G°$ is the standard Gibbs free energy, R is the universal gas constant, and a is the activity of the products and reactants.

Since the activity of the solid materials equals one, the activity of the gases corresponds to their partial pressure. Equation (2.3) can be simplified as follows when the system is at equilibrium ($\Delta G = 0$):

$$\Delta G° = RTIn(p_{O_2}^{y/2}) \qquad (2.4)$$

As can be concluded from Eq. (2.4), the formation or dissociation of the oxide scale depends on the temperature and the equilibrium pO_2. Ellingham-Richardson diagrams are used to illustrate the stability of oxides as a function of temperature and pO_2 (see Figure 2.2). The lower a metal oxidations Gibbs free energy is the higher is the comparative oxide stability. Al_2O_3 is among the most stable oxides. Other relevant oxides are iron and chromium oxide.

Iron requires higher oxygen partial pressures to form its oxides compared to aluminium. Three iron oxide phases are depicted in Figure 2.2: wustite, FeO; magnetite, Fe_3O_4; and hematite, Fe_2O_3. Wustite has the poorest corrosion resistance, then comes magnetite, while hematite, with a corundum structure, is the most protective among the three oxides, depending on the corrosion environment.

Eskolaite (Cr_2O_3) has the corundum-type structure. For a corundum-type structure, oxygen anions form a hexagonal closed packed lattice in which the metal cations fill two-thirds of the octahedral holes. Chromium oxide forms a dense slow-growing scale with a high degree of stoichiometry, enabling it to be a protective corrosion barrier.

Aluminium oxide has several allotropic forms of which α-Al_2O_3 is the most desirable and thermodynamically stable with a corundum structure. Other, metastable, forms of alumina, such as γ-Al_2O_3 offer less corrosion protection compared to α-Al_2O_3.

The corundum-type oxides such as hematite, eskolaite and alumina can form solid solutions.

For this licentiate thesis, it is important to point out that the pure oxides described above can only be formed as inner oxide scale. Due to the incorporation of alkali species from the melt into outwards growing oxides, an alkali transition metal oxide (AMO_x) is produced, as discussed in Chapter 3.

The Ellingham-Richardson diagram visualizes the temperature and oxygen partial pressure dependence of the Gibbs free energy for individual element oxidation reactions.

However, due to differences in reaction rates, it is not always the oxide with the highest thermodynamic stability that forms but rapidly nucleating metastable phases. Therefore, kinetic considerations are important for a better understanding of the corrosion process. Knowing the rate of reactions not only helps in understanding the corrosion mechanism but is also essential for estimating the lifetime of an alloy implemented in certain applications and under specific conditions.

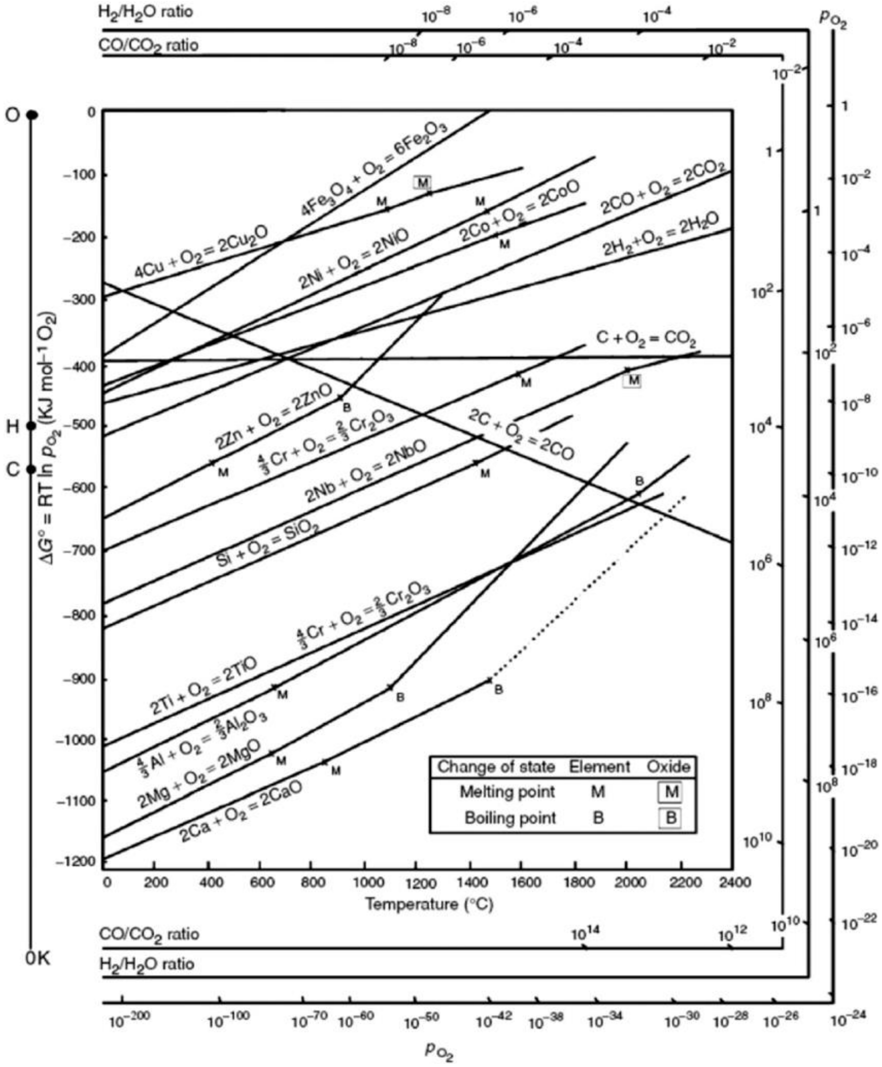

Figure 2.2 Ellingham-Richardson diagram showing the stabilities of the different oxides as a function of temperature [10].

Oxidation kinetics are generally determined by measuring the mass change of the corroded metal as a function of time. However, in some cases, and particularly in the present work, it is difficult to obtain accurate mass change measurements of the exposed samples due to the yet-unquantified dissolution of alloy elements into the liquid phase, and due to intense surface cleaning methods. In addition, the mass change values might not always refer to scale growth. Commonly, oxidation kinetics are defined in terms of ideal rate laws and are used to evaluate oxide scale growth. As depicted in Figure 2.3, kinetic laws of scale growth is often expressed by a small number of ideal behaviour: logarithmic, parabolic and combinations thereof.

Logarithmic corrosion behaviour is present when an initial rapid increase in mass change is detected, and thereafter the mass gain rate declines significantly. Initially, relatively fast oxidation forms a thin oxide scale, which decelerates with time, obeying Eq. (2.5):

$$X = k_{log} \log\ (t + t_0) + A \qquad (2.5)$$

where X is the oxide scale thickness, which can also be replaced by the measured mass gain Δm, k_{log} is the logarithmic rate constant, t is the exposure time, and A is a constant. This behaviour expresses very efficient passivation of a metal surface by scale formation. At high temperatures, α-Al_2O_3 presents similarly excellent oxidation behaviour due to the large band gap characteristic suppressing the transport of charge carriers across the oxide scale [32].

Most oxide scales formed during high-temperature oxidation are described by the parabolic kinetic reported by Carl Wagner [25], as shown in Eq. (2.6). In this process, scale growth relies on the diffusion of ions and electrons through the formed oxide scale; thus, the thicker the scale, the longer are the paths for the charged species travelling through the scale as has been shown previously in Figure 2.1.

$$X^2 = k_p\ t + C \qquad (2.6)$$

where X is the oxide thickness, k_p is the parabolic rate constant, t is the exposure time, and C is the integration constant. The mass change Δm can be employed instead of the scale thickness X.

Breakaway oxidation, which can be distinguished from the alloy's kinetic behaviour, is described in terms of a transition from a slow-growing scale to a thick non-protective fast-growing scale, reflected by high mass gain values. For this study, the mass change diagram (Figure 2.4) has been extended by a mass loss curve which occurs in a special case that will be discussed in Chapter 5.1. In this case, mass loss occurs in the absence of oxidation, nitridation, carburization, where leaching by, for example, chloride attack occurs instead.

The exponentially accelerating behaviour of the dissolution process can be attributed to the increase of area with time attributed to the increased accessibility of grain boundaries.

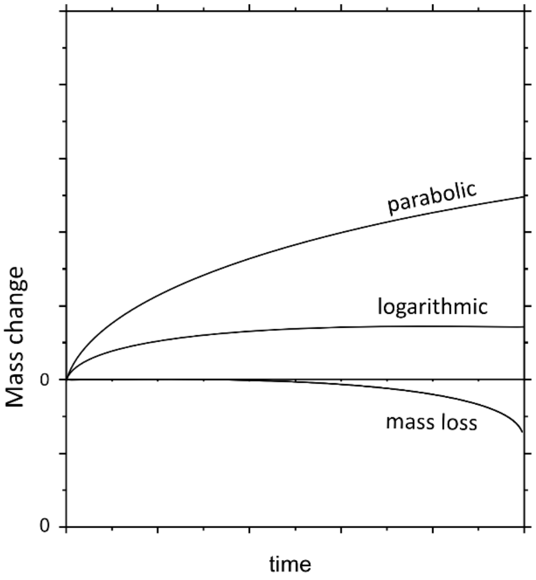

Figure 2.3 High temperature oxidation kinetic: where positive mass change values represent the kinetic behaviour for oxide scale growth [24]. Negative mass change values are attributed to mass loss due to leaching by the chlorides attack in the absence of an oxide scale.

2.3 Charge Carriers in an Oxide Scale

Following the initial rapid formation of a thin oxide scale, the thickness increases progressively through the transport of charge carriers across the scale. As shown in Figure 2.1 and described by Carl Wagner [25], the scale growth requires transporting metal cations, oxide ions, electrons, and oxygen or metal vacancies. We can distinguish between inward and outward growing oxide scales. Outward growing oxide scales grow by outward cation diffusion, while inward growing scale grows by inward anion diffusion, e.g., O^{2-}. These charged species can travel through the oxide scale lattice via solid-state diffusion, depending on the grain size or crystal defect concentration.

The diffusion paths that ions and vacancies can take are lattice diffusion and short-circuit diffusion.

In lattice diffusion, ions travel through the most common types of crystal defects, i.e., vacancies, interstitials, and impurities. As lattice-defect diffusion typically requires higher activation energies compared to short-circuit diffusion, it usually occurs at relatively higher temperatures. Short-circuit diffusion relies on extended microscopic defects, such as vacancies along grain boundaries, dislocations, or segregated phases with higher conductivity. These are relatively easy paths, and since this requires lower activation energy, these paths facilitate oxide growth even at lower temperatures.

3 Corrosion by Salt Melts

This chapter focuses on corrosion in a more complex environment, namely salt melts. An overview of the corrosion processes in nitrate, carbonate, and chloride melts is provided, covering the thermodynamics, corrosion products, kinetic processes and the roles of impurities in such corrosive environments. As discussed in Chapter 2, most high-temperature alloys form a protective oxide scale based on the selected alloying element and the specific exposure conditions. Nevertheless, high-temperature corrosion in molten salts is not that different from oxidation in a gas environment in respect with the basic anode process [Eq. (3.1)] and the reduction of oxidising species [Eq. (3.2)], resulting in metal oxide formation.

$M \rightarrow M^{n+} + ne^-$ (3.1)
$O_2 + 4e^- \rightarrow 2O^{2-}$ (3.2)

The identification of the decisive redox pairs allows us to apply, in this case, basic assumptions about the salt melt reactions with alloy species following the standard electrochemical series as well as thermochemical diagrams.

However, the level of complexity is increased by the presence of more than one potential oxidising species, more than one reacting cation at the melt/oxide interface as well as an additional aggregation state, the liquid melt. Gas environments that can cause high temperature corrosion commonly comprise more than one gas species with individual partial pressures < 1. The salt melts considered in this study are mixtures of nitrate, carbonate, and chloride salts. In these mixtures, the activity of the anion ion is 1.

in contact with a sample surface has an activity 1 for all cationic and anionic species.

The following section summarises the most relevant corrosion mechanisms in hot TES tanks.

3.1 Acid/Base Model

Molten salts are electrolytes and support electrochemical reactions. At the metal/melt interface, alloy elements can be oxidised, and salt species and impurities can be reduced. Corrosion by salt melts is referred to as a "complex corrosion environment" due to the complexity of the reactions that can occur in such environments, which contain solids, liquids, and gases, and all of these must be considered [2].

The ionic salt species play significant roles in the corrosion process. The anionic species can be categorised as: *oxyanions*, such as sulphate, nitrate, and carbonate; and *halide-based salts*, such as chloride [2]. Corrosion in such a melt can be described in terms of the acidity/basicity of the salt melt, defined by the Lewis acid/base concept. A Lewis acid is an electron pair acceptor with empty valence orbitals available. In turn, a Lewis base is an electron-pair donor. Already at this stage, we can assign a metal cation with this role as a Lewis acid.

Oxyanions (e.g., NO_3^-) in molten salts can release oxide ions upon reduction by alloy components. Relevant examples are described in Eqs. 3.2, 3.3 and 3.4 and illustrated schematically in Figure 3.1:

$CO_2 + 2e^- \rightarrow CO + O^{2-}$ (3.3)
or
$NO_3^- + 8e^- \rightarrow N^{3-} + 3O^{2-}$ (3.4)

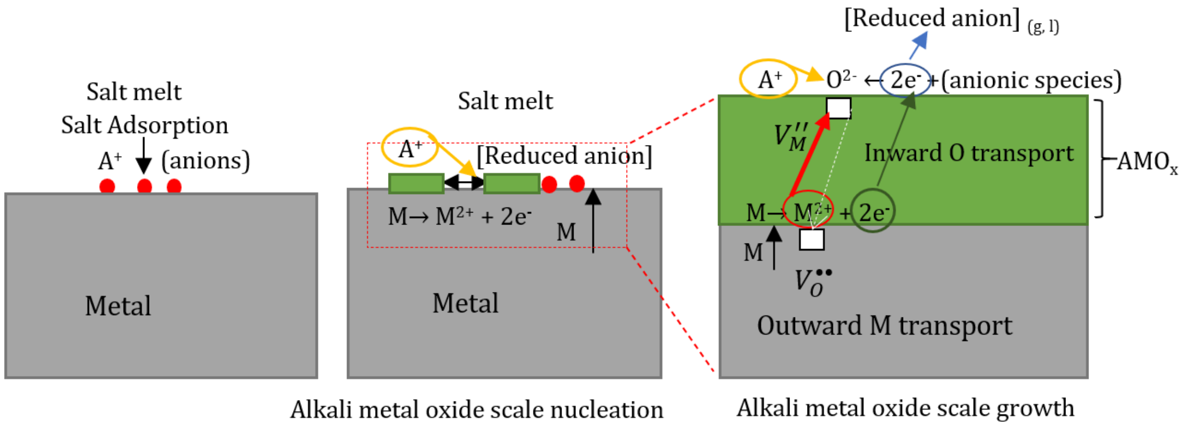

Alkali metal oxide scale nucleation

Alkali metal oxide scale growth

Figure 3.1 Alkali oxide scale formation when an alloy is exposed to alkali salt melt, where $V_O^{\bullet\bullet}$ *is an oxygen vaccancy,* V_M'' *is a metal vacancy and* A^+ *is an alkali cation.*

The last example illustrates that not only oxide ions act as a Lewis base. In the following sections, nitrogen and carbon forming metal nitrides and carbides, respectively, also plays a Lewis base role. For instance, nitrogen undergoes stepwise reduction from the oxidation state +V in the nitrate melt, via +III in the transient form of a nitrite, with possible evaporation via +II, NO(g), but is also -III as a metal nitride, e.g., chromium nitride as precipitates beneath the oxide scale (Chapter 5.1.1).

The oxide ion activity a(O^{2-}) is used as a descriptor of melt basicity and to construct thermochemical diagrams [33]. Thermochemical diagrams are useful to identify conditions for oxide scale stability and for dissolution into the melt.

Chloride melts are potential candidates as HTF and TES media for Gen3-CSP plants due to their superior thermal stability and favourable thermal properties [14]. Considering the standard electrochemical series of elements, alkali chlorides are theoretically good candidates with respect to high-temperature corrosion, due to the fact that neither the A^+ nor Cl^- ions, can be reduced by metal species from the alloy:

$$M(alloy) + A^+ + Cl^- \nrightarrow M^+ + A(metallic) + Cl^- \qquad (3.5)$$

which in turn disallows corrosion [33].

3.2 Solubility and Fluxing

Among the different corrosion mechanisms in salt melts, oxide fluxing has been extensively discussed. The fluxing process in an oxidising environment can be defined as accelerated corrosion through the dissolution and reprecipitation of metal oxides into the salt melts. The oxide fluxing process depends on the metal/metal oxide and the salt basicity/acidity [34]. Diffusion processes in liquid salts are very rapid compared to solid-state diffusion in an alloy or oxide. The activation energies for the dissolution of ionic species into a melt are generally lower than those for evaporation of molecular species into a gas stream.

3.3 Corrosion of Alloys in Chloride Melt

Indacochea et al. studied the corrosion of low-alloy steel and different stainless-steel alloys exposed in LiCl melt at 725 °C for 30 days in argon under extremely pure and dry conditions; it has been reported that corrosion is successfully suppressed under these conditions. However, after replacing argon with Ar-10% O_2, the alloys underwent severe corrosion, forming non-protective oxides [35, 36]. Thus, alloy constituents can reduce oxygen or water; we can conclude that high-temperature corrosion in alkali chlorides is driven by oxidising impurities in the melt.

Intergranular corrosion (IGC) is relatively common in molten chlorides, a form of localised corrosion defined as preferential attack on the grain boundaries. IGC is considered a type of galvanic corrosion, where some heterogeneity is observed at the grain boundary region. According to [37], in the case of IGC, *"the grain boundary is considered anodic to the bulk or adjacent alloy microstructure."*. In IGC, one of the alloying elements is depleted due to its interaction with oxidising species and further precipitation at the grain boundary [12].

Numerous studies have investigated the corrosion behaviour of several alloys in contact with chloride melts under different conditions [27, 33, 38-44]. The key findings related to this study are that $MgCl_2$-containing melts tend to precipitate MgO on the surfaces of the tested alloy and Cr depletion beneath the surface [44, 45].

As mentioned earlier, one of the envisaged eutectic melts for the operation of Gen3-CSP equipped with thermal storage capacities is the $MgCl_2$/KCl mixture. In this eutectic melt, impurities such as moisture, oxygen are potential oxidants. Thus, they significantly increase the corrosivity of the chloride melts. Therefore, chloride salt mixtures containing the highly hygroscopic $MgCl_2$ face a serious corrosion challenge due to the thermal dehydration of $MgCl_2.nH_2O$ to $MgCl_2$ and H_2O, and the hydrolysis of $MgCl_2$ to form MgOHCl which decomposes further to MgO precipitates and HCl.

Several studies have been dedicated to removing corrosive impurities by thermal and/or chemical purification methods [46-49]. For instance, the hydrolysis reaction of anhydrous $MgCl_2$ forming MgOHCl can be suppressed by applying stepwise controlled heating. Recently, Zhao and Vidal [47] have investigated a chemical purification method by adding elemental Mg to an $MgCl_2$ containing salt mixture, see Eq. (3.6), as a corrosion inhibitor, reducing the concentration of corrosive MgOHCl. The following procedure achieved the corrosion inhibition process: a) the addition of 6.5 wt% of NaCl and less than 0.1 wt% of elemental Mg to commercial $KMgCl_3$; b) applying controlled heating to reduce the impurities concentration MgOHCl and produce a eutectic salt with a lower melting temperature.

$$2MgOHCl + Mg \leftrightharpoons 2MgO + MgCl_2 + H_2 \tag{3.6}$$

Considering the massive amounts of salt (thousands of tonnes) required as TES material in a CSP plant, the purification process will entail additional costs for the power plant. In this context, many studies have been conducted to find a cost-effective way to purify the salts [2, 50, 51].

Lately, Ding and Bauer [49] have reviewed and summarised recent studies that have employed molten chlorides as HTF/TES and described the characteristic corrosion challenges that metallic components face when in contact with these salts. Some of the key points identified are: a) that salt purification in conjunction with corrosion mitigation strategies shall be adopted; and b) the importance of identifying new materials that can endure such aggressive environments.

3.4 Corrosion in Nitrate and Carbonate Melts

Since nitrate melts, mainly Solar Salt, have been utilised as HTF and TES materials for commercial CSP plants, the corrosion behaviour in these melts has been extensively studied at both laboratory and industrial scale [12]. As discussed earlier, corrosion by salt melts depends mainly on the salt's chemistry, the gas environment, and the exposure temperature.

Nitrate salts spontaneously decompose at high temperatures, as shown in equations Eqs. (3.7) and (3.8) [33].

The thermodynamics of the nitrate melts can be described in terms of equilibrium with the oxide ion and appropriate gas species [33, 38].

$$NO_3^- \leftrightharpoons NO_2^- + \frac{1}{2} O_2 \tag{3.7}$$

$$2NO_3^- \leftrightharpoons O^{2-} + 2NO + \frac{3}{2} O_2 \tag{3.8}$$

Besides the spontaneous decomposition of salt species, metal surfaces can act as an electron source for reduction as illustrated in Figure 3.1, resulting in reduced anionic species, e.g., NO_3^- which can take up two electrons forming a NO_2^- and releasing an O^{2-} ion instead of oxygen compared to Eq. (3.7).

Alkali oxide scale formation in nitrate/carbonate melts can be summarised as follows: the first step is the adsorption of the salt to the metal surface. Anions are reduced by electrons to from oxide ion. Alkali cations are attracted to the reduced anions and take part in the scale formation process. The alkali oxide scale nucleates when the reduced anions and metal cations occupy their respective sites at the metal/melt interface; the scale grows laterally with time until it covers the entire metal surface. The scale grows either outwards through metal ion transport by cationic vacancies adjacent to the adsorbed oxygen ions or inwards when oxygen ions occupy the oxygen vacancies formed at the alloy/oxide interface

Theoretical and experimental viewpoints have been adopted to study corrosion in the above-described melts. The extent of corrosion in nitrate melt depends on the acidity/basicity of the melts. The acidity/basicity of a salt melt can be defined by Eq. (3.9) as [33]:

$$pO^{2-} = -\log a_{O^{2-}} \tag{3.9}$$

The formation of corrosion products can be predicted using the pO^{2-} of the melt, in combination with electrochemical measurements, thereby defining the corroding metal and salt species and setting the exposure conditions [33].

Picard et al., used another approach by adjusting the activity of O^{2-} using different NO_3^- and NO_2^- ratios to construct a predominance diagram, iron (III) at 420-500 °C [50, 51], see Figure 3.2. In those studies, the pO^{2-} diagrams predicted mainly three solid corrosion products based on the basicity of the medium. $Na_4Fe_2O_5$(s) was expected to form in strongly basic media, whereas alkali ferrites, $NaFeO_2$(s), and iron oxide, Fe_2O_3(s), were expected to form in moderately basic and acidic media, respectively [50, 51]. What these diagrams failed to predict is, of course, the potential nitride formation, which occurs at very low oxygen partial pressures, present beneath the oxide scale, as described in the result section of this licentiate study occurs (Section 5.1.1).

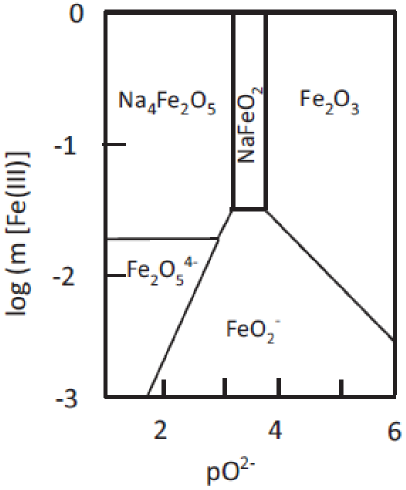

Figure 3.2 Stability diagram for iron species in nitrate-nitrite melts as a function of basicity at 500 °C [33, 51]. Source: Picard, G.S., H.M. Lefebvre, and B.L. Trémillon, 1987. Reproduced with permission from the Electrochemical Society [51].

Numerous studies have employed theoretical or experimental approaches, or a combination of both, to study the corrosion performance of alloys in nitrate melts. The metallic materials investigated in nitrate melts can be classified as carbon and low-alloy steels, stainless steel, and FeCrAl alloys [12, 52-67].

The main insoluble corrosion products formed in contact with nitrate melts and related to this licentiate study are summarised as follows: an inner scale of $(Fe,Cr)_3O_4$ [58], or an outer $NaFeO_2$ and inner Fe_3O_4, Fe_2O_3 scales [61, 62]. The corrosion products detected depend on the alloy chemical composition and the exposure conditions.

Carbonate salt mixtures are considered a potential candidate for Gen3 CSP plants. However, corrosion in this melt environment has not been as intensively studied as in nitrate melts. Nevertheless, corrosion resistance has been investigated in molten carbonate fuel cell (MCFC) applications, since carbonate salts are used as electrolytes in these processes. The carbonate salt decomposes upon temperature into the cationic alkali species (A^+), oxide ions, and CO_2. The basicity of the melts, measured by Eq. (3.10), depends on the equilibrium with the oxide ion and CO_2 [33]:

$$A_2CO_3 \leftrightharpoons 2A^+ + O^{2-} + CO_2 \qquad (3.10)$$

Since the oxide-melt interactions in carbonates are acid-base reactions, their products are expected to be similar to those produced in nitrates [33]. The stability of the corrosion products are mainly dependent upon the salt's chemistry, acidic/basic fluxing in the melts and temperature [68].

In the present study, alkali carbonates in contact with alloys have been investigated under CO_2 gas, in contrast to the cases of alkali nitrates, which were operated in air. This means that we have two sources of CO_2, one resulting from the spontaneous decomposition of alkali carbonate at the metal surface and the other in the form of CO_2 dissolved into the melt from the gas phase. Both of these sources of CO_2 can be reduced by alloy species, carbon monoxide (gas evolution), as shown in Eq. (3.11), or even inwards diffusing carbon at the metal/oxide interface, which are able to cause carburisation underneath the oxide zone [Eq. (3.12)].

$$2M + nCO_2 \longrightarrow 2M^{n+} + nCO(g) + nO^{2-} \text{ (gas evolution)} \qquad (3.11)$$

or

$$4M + nCO_2 \longrightarrow 4M^{n+} + nC + 2nO^{2-} \text{ (carburising)} \qquad (3.12)$$

Carburisation can be described as an internal corrosion attack that occurs when a scale-forming alloy component such as chromium is selectively bound to carbon in the alloy interior. Internal carbide precipitation suppresses the migration of, e.g., chromium to the oxide/metal interface to form an oxide scale. Initial internal carburisation occurs as precipitates along grain boundaries. Carburisation is not desirable, as it compromises the alloy's chemistry and changes its mechanical integrity [69, 70].

Many studies have been dedicated to the corrosion of metallic materials in carbonate melts under various conditions [34, 71-79]. The main corrosion products detected relevant to this licentiate study can be classified as: i) insoluble corrosion products, such as $LiFeO_2$ [34], $LiCrO_2$, and $FeCr_2O_4$ [40]. In addition to Al_2O_3, Fe_2O_3 or $NiFe_2O_4$ and $CrFe_2O_4$ [43]; ii) soluble corrosion products such as K_2CrO_4 [40]. The detected corrosion products depend on the alloy's chemistry and the exposure, see [34, 71-79].

All the publications concerning alkali carbonate melts point out that chromia-forming alloys at high operating temperatures do not resist rapid alkali oxide scale formation and internal attack [80]. In strong contrast, alumina-forming alloys show far better corrosion resistance to molten carbonate attack by slow alkali aluminate scale growth and limited or even absent internal carburisation.

In summary, previous studies on the corrosion resistance of chromia-forming stainless steel alloys have highlighted the need to identify alternative alloys or utilise corrosion mitigation methods for metallic components considered for use in Gen3 CSP plants [33, 43, 52, 80-84].

4 Experimental Layout

The flow chart depicted in Figure 4.1 provides an overview of the experimental work conducted in this thesis. The figure shows that two main studies have been conducted. The following sections provide detailed descriptions of the salts, alloys, experimental set-ups, and characterisation.

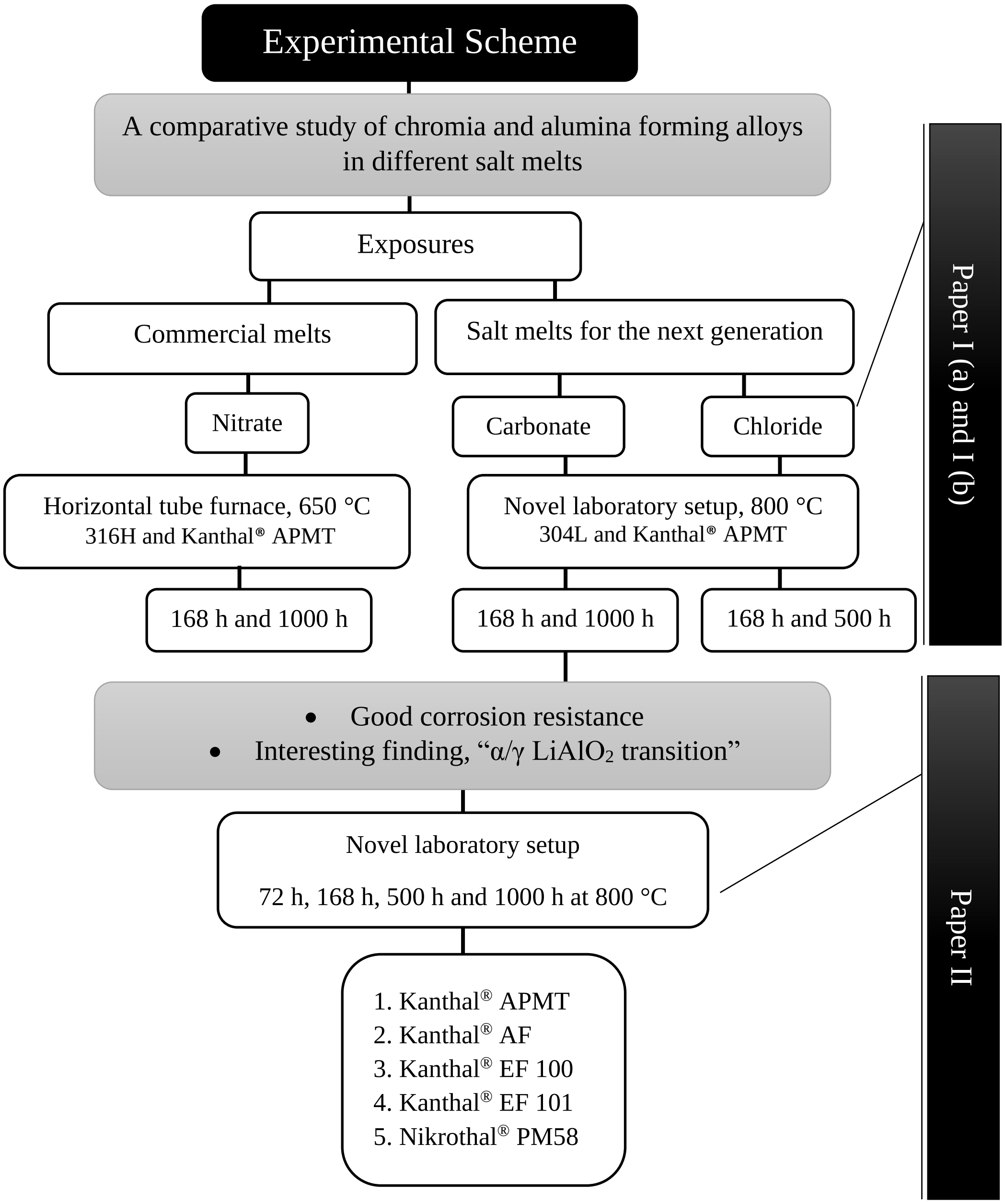

Figure 4.1 Flow chart illustrating the experimental layout for the thesis.

4.1 Materials

4.1.1 Salt Melts

As described in Chapter 1, the eutectic salt melts were selected based on their favourable thermophysical properties, cost, and other factors that recommend their potential usage in commercial CSP plants [14].

In this licentiate thesis, the following eutectic salts were chosen: a binary nitrate salt mixture, which is also known as Solar Salt (60 wt% $NaNO_3$, 40 wt% KNO_3); a ternary carbonate salt (32.1 wt% Li_2CO_3, 33.4 wt% Na_2CO_3, 34.5 wt% K_2CO_3); and a binary chloride mixture (64.4 wt% KCl, 35.6% wt% $MgCl_2$). The thermophysical properties of these salt mixtures have been discussed in several articles [44, 85-87].

Salts were purchased from the following suppliers: $NaNO_3$ (Alfa Aesar, 99.0%); KNO_3 (Alfa Aesar, 99.0%); Li_2CO_3 (VWR Chemicals, 99.0%); Na_2CO_3 (EMSURE, anhydrous, 99.9%); K_2CO_3 (ThermoFisher Scientific, 99.8%); KCl (Alfa Aesar, 99.0%); and $MgCl_2$ (Alfa Aesar, anhydrous, 99.0%). Since impurities play a vital role in the corrosion process [12, 39, 86-88], the impurities concentrations of each salt are provided in Table 4.1. The tabulated values for impurities have been obtained from the salts' chemical datasheets.

Table 4.1 The overall impurities' concentrations in the salts, as reported by the suppliers.

Salt	Moisture	Chloride (Cl^-)	Phosphate (PO_4^{3-})	Silicate (as SiO_2)	Total Sulphur (as SO_4^{2-})	Calcium (Ca^{2+})	Magnesium (Mg^{2+})	Others
$NaNO_3$	Detected	0.0006 %	1.2 ppm	-	0.0020%	0.0008%	0.0005 %	Heavy metals (e.g., $Pb^{2+/4+}$), $Fe^{2+/3+}$ 1 ppm for each
KNO_3	Detected	0.002%	5ppm	-	0.003%	0.005%	0.002%	Heavy metals 5 ppm, $Fe^{2+/3+}$ 3 ppm, IO_3^- 5 ppm, NO_2 0.001%, Na^+ 0.005%
Li_2CO_3	Detected	≤ 0.02%	-	-	≤ 0.05%	0.01%		Heavy metals (e.g., $Pb^{2+/4+}$) ≤20 ppm, $Fe^{2+/3+}$ 3 ppm
Na_2CO_3	Loss on drying ≤ 1.0%	≤ 0.002%	≤ 0.001%	≤ 0.002%	≤ 0.005 %	≤0.005 %	≤ 0.0005 %	Heavy metals (e.g., $Pb^{2+/4+}$), $Fe^{2+/3+}$, $N^{3-/3+/5+}$, Al^{3+}, K^+
K_2CO_3	0.113%	KCl 0.0043 %	-	-	K_2SO_4 12 ppm	-	-	KOH 0.106%, Na^+ 0.20%, $Fe^{2+/3+}$ 0.40 ppm
KCl	detected	Chlorate and Nitrate ≤0.003 %	≤ 5ppm		≤0.001%	≤0.002%	≤0.001 %	Ba^{2+} ≥ 0.001%, Br^- ≤0.01%, I^- ≤ 0.002%, $Fe^{2+/3+}$ ≤3 ppm, Na^+ ≤0.005%, Heavy metals (e.g., $Pb^{2+/4+}$) ≤5 ppm
$MgCl_2$	Detected 0.97%	NaCl 36 ppm $CaCl_2$ 47 ppm	-	-	-	-	-	MgO (100 ppm)

As already mentioned, the experiments in this study were conducted about 100 °C above the anticipated operation temperature in thermal storage for two reasons: 1) likely, metallic parts in a large CSP plant wetted with salt melts are experiencing temporary overheating, and 2) accelerated corrosion provides relevant results within the timeframe of this study.

The eutectic mixtures were prepared according to the following procedure. In 100-g batches, the salts were weighed and mixed to the correct ratio, then ground using a mortar and pestle. Lastly, the salts were furnace-dried at 110 °C for a period of at least 24 h.

Since the water content is critical for the corrosion experiments, chloride mixtures were prepared using a purification process under Ar to reduce the moisture content in the salts [27, 49, 89].

Based on previous studies [27, 49, 89], the chloride mixtures were purified using a stepwise thermal purification process. The purification process starts with drying the salt mixture at 110°C for at least 5 hours under an Ar flow. Then, the temperature is raised to 200°C and held for a 2-hour dwell time. Then, the temperature is increased again to 300°C for 2 hours. Thereafter, the set-up is allowed to cool to room temperature under argon flow. As the last step, an alloy sample is dipped into a salt-filled crucible before initializing the corrosion experiment. The vessels that contain the salt-filled crucible are purged with Ar for 12 h, then heated to 120°C for at least 12 h. Lastly, the temperature is raised to 750°C and held for 1 hour before the corrosion experiment starts, as described later in this chapter.

4.1.2 Alloys

Table 2. summarises the nominal compositions of the alloys investigated.

The following procedure describes how the samples were prepared. First, metal coupons of initial dimensions of 15 × 15 × 2 mm were ground using up to 1200-grit SiC abrasive paper, then polished with suspensions containing 9, 3, and 1µm diamonds till a mirror-like finish was obtained. The polished samples were cleaned in three steps with deionised water, acetone, and ethanol using an ultrasonic bath at room temperature. Finally, the coupons were dried using an air gun, and then dipped into salt-filled alumina crucibles.

Table 4.2 Nominal alloy compositions.

Alloy (publication)	**Fe**	**Ni**	**Cr**	**Al**	**Si**	**Mn**	**Mo**	**Others**
316H [**Paper I** (a and b)]	balance	11.5	17	X	0.6	1.5	2.1	C 0.05
304L [**Paper I** (a and b)]	balance	9.5	18.5	X	0.4	1.3	X	C 0,02
Kanthal® APMT [**Paper I** (a and b), **Paper II**])	balance	X	21	5	0.7	0.4	3	RE; C 0.08
Kanthal® AF (**Paper II**)	balance	X	21	5.3	0.7	X	X	RE; C 0.08
Kanthal® EF101 (**Paper II**)	balance	<0.5	11-14	3.2-4.2	1.2	<0.7	X	RE; C 0.08
Kanthal® EF100 (**Paper II**)	balance	<0.5	9.5-13	3.8-4.2	<0.5	<0.7	X	RE; C 0.08
Nikrothal® PM58 (**Paper II**)	18	balance	19	5	0.4	X	X	RE

4.2 Experimental Setup

In this work, two set-ups were used. Initially, a horizontal tube furnace was utilised for corrosion exposures in nitrate melt. Subsequently, a novel vertical set-up was designed and implemented for the exposures involving carbonate and chloride melts. Table 4.3 summarises the experimental parameters and corrosion conditions in the different environments.

Table 4.3 A summary of eutectic melting points, and decomposition temperature of the different salt mixtures, in addition to the experimental parameters for the corrosion experiments,

Eutectic salt mixture	*i.) Nitrates* (60 wt% $NaNO_3$- 40 wt% KNO_3)	*ii.) Carbonates* (32.1 wt% Li_2CO_3 -33.4 wt% Na_2CO_3- 34.5 wt% K_2CO_3)	*iii.) Chlorides* (65 wt% KCl- 35% wt% $MgCl_2$)
$T_{eutectic}$ (°C)	230 [14]	398 [90]	423 [91]
T_{max} (°C)	530-565 [14]	>650* [86]	>800 [87] [91]
Gas	filtered air	CO_2	argon
Exposure temperature	650 °C (isothermal) (72 h cyclic refilling of the salt) [**Paper I** (a and b)]	800 °C (isothermal) (336 h cyclic refilling of the salt) [**Paper I** (a and b), **Paper II**])	800 °C (isothermal) (336 h cyclic refilling of the salt) [**Paper I** (a and b), **Paper II**])
Total exposure time	168 & 1000 h [**Paper I** (a and b)]	168 & 1000 h [**Paper I** (a and b)] 72, 168, 500 and 1000 h (**Paper II**)	168 & 500 h [**Paper I** (a and b)]

** Decomposition temperature varies with atmosphere. The actual temperatures were 1000 °C, 700 °C and 670°C for the exposures in CO_2, argon, and air, respectively [86].*

The schematic in Figure 4.2 describes the first set-up employed. The horizontal tube furnace was used for the corrosion experiments conducted in nitrate melt equipped with a quartz tube (50-mm diameter). The exposures were conducted isothermally at 650°C ± 5°C with filtered air at a flow rate of 20 ml/min.

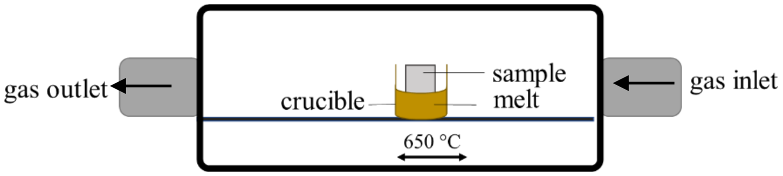

Figure 4.2 Experimental setup for horizontal-tube furnace nitrate exposures.

Among the reasons for building a new setup was the partial immersion of the coupons in the melts in the horizontal-tube furnace. The novel laboratory vertical setup was designed for complete immersion experiments. A top-loader furnace (model top 60 Nabertherm) was purchased and subsequently redesigned in the workshop by Esa Väänänen to comply with carbonate and chloride exposures in controlled gas environments. The detailed procedure for designing and building the vertical setup are provided in paper I (b) [92]; see a schematic diagram of the cylinder vessel Figure 4.3. The corrosion experiments were conducted isothermally at 800 ± 5 °C. The temperature was calibrated at the crucibles lowest point, with a gas (Ar or CO_2) at a 50 ml/min flow rate for each vessel. Each exposure was carried out at least twice to guarantee minimum reproducibility.

The novel laboratory setup is superior to the tube furnace because it provides the following advantages: i) the ability to test six coupons in each vessel in addition to providing duplicate samples. Overall 12 coupons can be tested simultaneously; (see a schematic diagram of the cylinder vessel Figure 4.3.); ii) the ability to remove coupons directly from the melts before they solidify; (see **Paper I** (b) section A5, since the solidified melts otherwise must be washed away from the tested coupons; and the washing procedure changes the alloy surface chemistry; and iii) one of the duplicate samples goes through washing for mass change measurements as described in the literature [27], [54, 93-98]. The second sample is dedicated to the cross-section analyses in unwashed form.

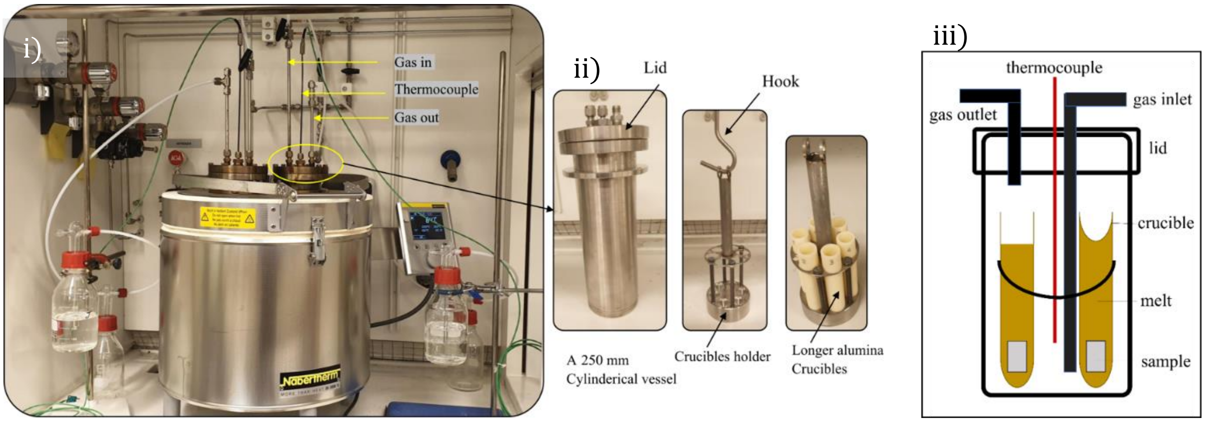

Figure 4.3 i) Novel laboratory vertical setup built for the carbonate and chloride exposures ii) Cylindrical vessel components iii) Schematic diagram of the cylindrical vessel. Reproduced with permission from Elsevier [92].

4.3 Analytical Methods

As mentioned earlier, high-temperature corrosion of metallic materials in contact with molten salts is highly complex. Different analytical techniques have been employed to attain a better understanding of the corrosion behaviour of the selected alloys. Duplicate samples were used to allow post-exposure analyses that required different sample preparation methods (see Figure 4.4), such as washing for mass change measurements, and X-ray diffraction (XRD) analysis being performed on one sample and cross-section preparation (including salt remnants) on the other sample.

After completion of the exposure experiment, the "unwashed" sample was extracted from the crucible filled with molten salt using the following procedure. After the required exposure is completed, the temperature is reduced and maintained at 50 °C higher than the mixture’s eutectic melting point. This enables pouring of the salts away from the coupons while they are in a molten state, and they are thereafter collected for further analysis. Only a small amount of the salts remains on the sample surface.

Following the standard cleaning method, the duplicate sample in the second vessel is washed, to remove all residual salts and solvable corrosion products from the sample surface [99]. At room temperature, the samples are sonicated and brushed until cleaning is complete. If any salt remains, the sonication is

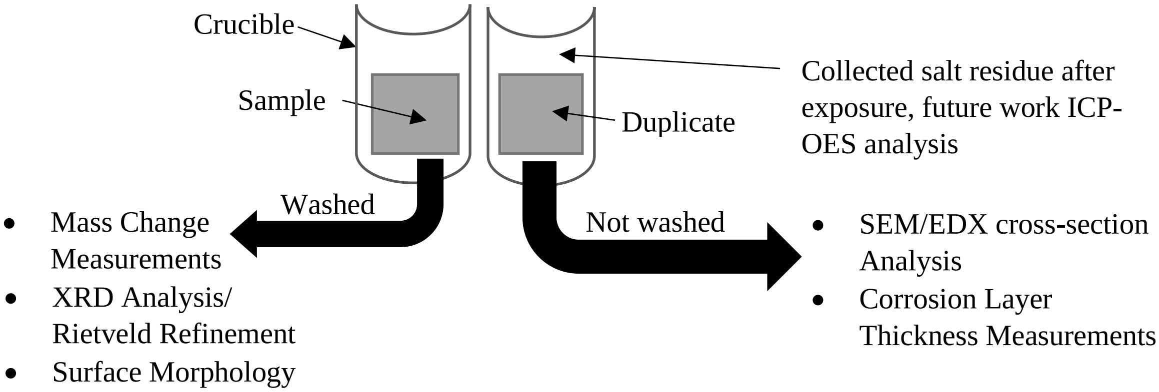

Figure 4.4 Schematic illustration showing the procedures for sample evaluation after the exposures.

interrupted, and the coupon is softly brushed to remove the salt. Thereafter, the sonication procedure is restarted to ensure that the salts are dissolved completely. It is worth noting that the results involving washed samples, such as the XRD analysis and weight change values, need to be carefully considered. Weight change measurements are not considered reliable data for corrosion evaluation, but rather as a supplement showing indications in the context of other characterisation techniques.

4.3.1 X-ray diffraction analysis

X-ray diffraction (XRD) is a non-destructive analytical technique that gives phase identification of a crystalline sample, in addition to providing information about lattice parameters and grain size. The XRD technique is based on constructive interference of a monochromatic and coherent X-ray beam with the sample, where interaction occurs between the X-rays and the sample's crystal structure. X-rays are diffracted when conditions satisfy Bragg's Law, as stated in Eq. (4.1), see Figure 4 [100].

$$n\lambda = 2d_{hkl}\, sin\theta \tag{4.1}$$

Where n is order of reflection (an integer number), λ is the wavelength of the X-rays, d_{hkl} is the interplanar spacing of lattice planes, and θ is the angle between the diffracted beam and the crystal plane.

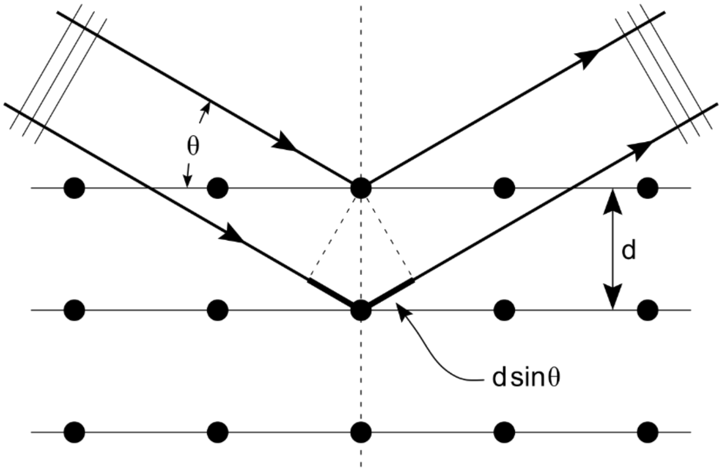

Figure 4.5 Schematic illustration of Braggs' law. An incident beam is reflected by a crystal plane at an angle θ. Source: Bragg, W.H.S., X-rays and crystal structure *ed. L.S. Bragg, 1915 [101].*

XRD analysis is used to identify the corrosion products formed. In addition to providing information about crystal structures, XRD analysis is the only tool, in this study, that is capable of detecting Li-containing corrosion products.

A Siemens D5000 grazing-incidence XRD equipped with a Cu source, a secondary Si monochromator, and a point detector was employed for the analysis of corrosion products. The grazing-incidence XRD technique uses a low incidence angle of the X-ray beam, limiting the penetration to the bulk material, thereby identifying crystalline phases in thin oxide scales. As mentioned in Figure 4.1, an interesting observation regarding the α/γ-$LiAlO_2$ phase transition detected on Kanthal APMT exposed to carbonate melt at 800 °C. To understand the α-$LiAlO_2$ to γ-$LiAlO_2$ phase transition, it is essential to quantify these crystalline phases on the sample surface with respect to the exposure time. The Rietveld refinement technique was used to quantify the crystalline phase in materials by implementing their XRD patterns.

The Rietveld refinement analysis is based on comparing the XRD patterns of a sample with a calculated diffraction pattern based on crystallographic data such as the crystalline system and atomic positions [102]. In the Rietveld method, "*refinement*" refers to the process of fine-tuning the model of parameters used to calculate a diffraction pattern to the closest observed value.

In this thesis, in collaboration with Dr. Michal Strach (Chalmers Materials Analysis Laboratory, Physics Department), the Rietveld refinement method with the acquired XRD patterns was employed using the TOPAS V6 software to calculate the α/γ-$LiAlO_2$ phase fraction ratios. More details about parameters used in this method can be found in **Paper II**.

4.3.2 Microstructural Analysis

Scanning electron microscopy (SEM) is used to investigate the microstructure of corroded samples by emitting electrons over a sample surface, where it interacts and generates signals that are translated further to produce an image. After the electron beam hits and interacts with the sample, signals are emitted and detected, providing information about the sample microstructure and elemental composition. Among these signals: i) secondary electrons (SE) are emitted upon electron interactions close to the sample surface. Accordingly, they are generally used to reveal the surface topography; and ii) backscattered electrons (BSE) have higher energy levels than the SE, which means that they have the capability to be emitted from deeper sections in the sample. The quantity of the collected BSE is influenced by the sample's density and chemical composition, apart from the operating parameters such as the electrons accelerating voltage. For instance, atoms with higher atomic numbers appear brighter in the BSE image than atoms with lower atomic numbers (Z-contrast) [103].

As illustrated in Figure 4.4, washed samples were subjected to surface morphology inspection. While unwashed samples were used in the investigation of cross-sections. The cross-section preparation procedure for the samples was as follows: i) samples underwent dry cutting with a low-speed diamond saw and were then sputter-coated with gold; ii) three methods were used before the cross-sectional microscopy analysis: cold embedding in epoxy resin, hot mounting in Bakelite or utilising broad ion beam (BIB) milling with a Leica TIC 3X instrument; and iii) before BIB milling, a thin polished silicon wafer was applied to the sample's surface to protect the oxide scale. Details of the milling parameters are provided in **Paper I** (b).

The surface and cross-section inspection were conducted using a JEOL JSM-7800F Prime or Phenom ProX Desktop SEM equipped with an energy dispersive x-ray (EDX) detector. The EDX spectra were collected using an electron beam with a 15 kV accelerating voltage.

5 Results and Discussion

Two primary aims are pursued in this licentiate thesis: 1) to compare the corrosion behaviour of chromia- and alumina-forming alloys in contact with different salt melts. The melts employed in this study are current and potential salt mixtures utilised in commercial CSPs; and 2) to understand and rank the corrosion performance of five alumina forming alloys in contact with alkali carbonate melt by investigating scale formation.

Towards these goals, the research findings in this chapter are divided into two parts.
Part I:
Comparison of the corrosion performance of FeNiCr and FeCrAl alloys in three environments.

- Corrosion of 316H and Kanthal APMT in Nitrate Melt at 650 °C
- Corrosion of 304L and Kanthal APMT in Carbonate Melt at 800 °C
- Corrosion of 304L and Kanthal APMT in Chloride Melt at 800 °C

Part II:
Ranking of five alumina-forming alloys in terms of their corrosion performance in contact with alkali carbonate melt at 800 °C. Lithium ions in the mixed alkali melt induce the formation of lithium aluminate ($LiAlO_2$) at the alloy/melt interface. Alumina-forming alloys have an ability to prevent internal corrosion by forming α-$LiAlO_2$ layer. Thus, Part II focusses on the characteristics of the $LiAlO_2$ layer and distinguishes between:

- "Normal" formation and transformation of $LiAlO_2$
- "Deviating" formation and transformation of $LiAlO_2$

In this work, a combination of quantitative and qualitative approaches was adopted to evaluate samples after exposure. Weight change and scale thickness measurements of exposed samples provide a quantitative overview. Compositional and microstructural investigations and Rietveld analysis provide qualitative and semi-quantitative analysis. As described in Chapter 4, mass change was measured after rinsing the samples with water, entailing the loss and dissolution of soluble corrosion products. Therefore, the evaluation of corrosion is based mainly on top-view and cross-section microscopy investigations, while the mass change values are used as complementary data.

Figure 4.4 gives an overview of how the corroded samples are evaluated after exposure.

As discussed earlier, high-temperature corrosion of metallic materials in contact with salt melts is highly complex. While Chapter 3 gives an overview of the corrosion mechanisms related to salt melts, Figure 5.1 (Path A) summarises the corrosion propagation steps identified in this work for the nitrate and carbonate exposures. Figure 5.1 (Path B) describes the corrosion in the chloride melt, as discussed in Section 5.1.3.

Path A comprises: alkali oxide nucleation at the metal/melt interface and formation of alkali metal oxide scale. This path can progress either in the absence of internal corrosion following Case I and II, i.e., AMO_x scale growth and eventually $\alpha \rightarrow \gamma$-$LiAlO_2$ phase transformation. Alternatively, an internal attack can occur following Case III and IV by inwards diffusion of oxidising species simultaneously to the AMO_x growth.

Path B comprises: Case V) no oxide scale formation; and Case VI) formation of cavities due to leaching and environmentally induced intermetallic precipitation.

In Path A, during oxide scale growth, a depletion zone is created adjacent to the growing oxide scale, depending on whether or not the oxidising alloy element replenishes rapidly. Furthermore, the bulk diffusion of, e.g., Al can be compromised by precipitation of AlN. The scale-forming elements derived from the alloys are Al and Cr in the first publication and mainly Al in the second one. The availability of Al and Cr at the metal/melt interface defines the elemental composition of the oxide scale. Thus, the bulk diffusivities and grain boundary diffusivities are decisive for the formation process.

Notably, if a melt interacts with metal and forms an insoluble corrosion product, this means the possibility of this corrosion product to be protective for the alloy [104].

Another mechanism discussed in Section 5.2 is "oxide transformation", as shown for Case II in Figure 5.1, where a phase transition in the oxide scale is observed.

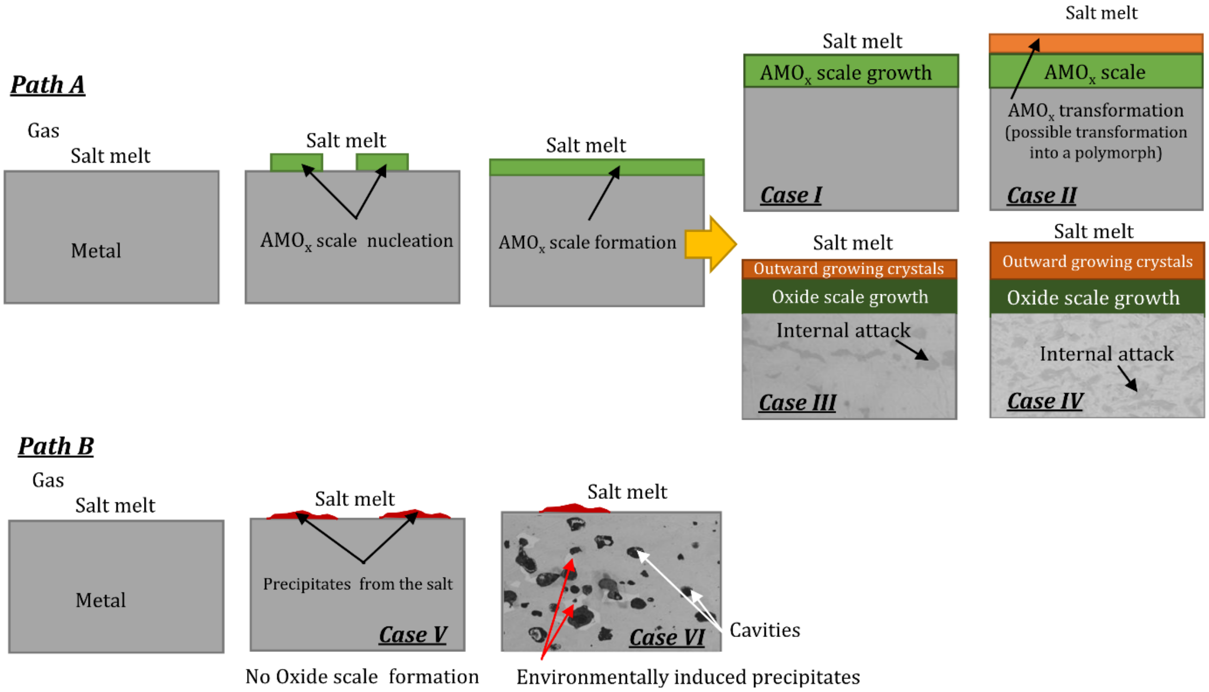

Figure 5.1 Schematic illustration of paths A and B for scale nucleation, growth, possible transformation, and degradation in the alloys exposed to salt melts.

Finally, as discussed in Chapter 3, the bulk alloy may suffer from an internal attack, as shown for Case III and IV in Figure 5.1. The attack occurs via the diffusion and permeation of specific reactants, such as carbon in the case of carbonate melts. Carbon interacts with the alloy to form internal chromium carbide precipitates. These precipitates alter the alloy chemistry and raise technical challenges.

In the following sections, the corrosion of the alloys will be discussed based on these mechanisms.

5.1. Comparative Study of the Corrosion Performance of Chromia- and Alumina-Forming Alloys in Three Different Salt Melts

Figure 5.2 shows an overview of a corrosion assessment of chromia- and alumina-forming alloys exposed to different salt melts. This evaluation is based on measurements of corrosion zone thickness. The alloys tested in the nitrate melt were 316H (a chromia-forming alloy) and Kanthal® APMT (an alumina forming alloy), while 304L (a chromia-forming alloy) and Kanthal® APMT were used for exposures to alkali carbonate and chloride. In the same Figure, the materials are ranked based on three main features: outward growing zone, inward growing zone, and internal oxidation/attack. Figure 5.2 shows the significant differences in corrosion behaviour between the chromia-forming and the alumina-forming alloys, particularly with respect to internal attack.

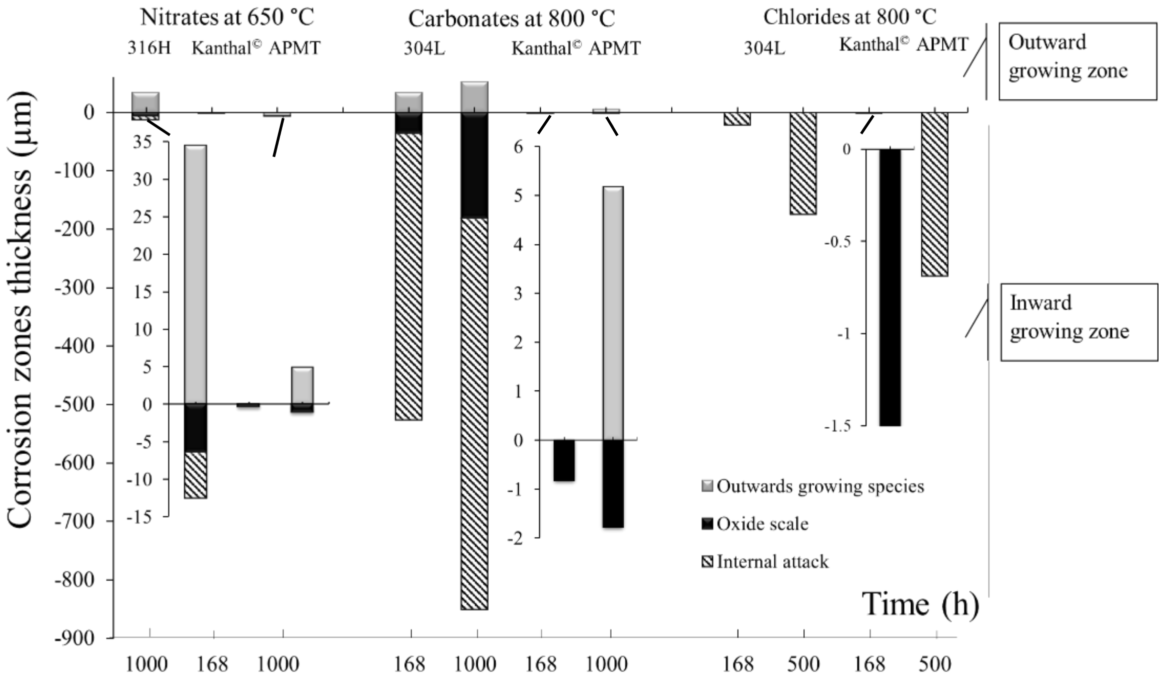

Figure 5.2 Comparative schematic for all the corrosion layer thickness measurements made in this study. The differences between the outward-growing and inward-growing zones are distinguished. The horizontal axis is placed at the apparent initial material surface. Reproduced with permission from Elsevier [77].

Figure 5.3 shows the mass change for 304L and Kanthal® APMT exposed to carbonate and chloride melts. Mass change data in nitrate melt were not collected due to the partial immersion of the samples, as described in Section 4.2. Due to the post-exposure treatment of samples before the mass change measurements (see Section 4.3), the observed mass change trends (dashed trendlines in Figure 5.3) need to be interpreted with caution.

For exposures to carbonate melt, Kanthal APMT showed a significantly lower mass gain than 304L, indicating a sub-parabolic behaviour. However, after 1000 h, the mass gain values for Kanthal APMT deviated from the indicated curve; this aspect will be addressed in Section 5.1.2.
When alloy 304L was exposed to the carbonate melt, it maintained a steady-state behaviour after a rapid initial mass gain.

Whereas the carbonate melt caused a mass gain for the exposed samples, the chloride melt caused mass loss for both tested alloys. However, the mass loss was lower for the Kanthal APMT samples. The chloride melt was the only environment where a notable loss of sample thickness was detected, as discussed in Section 5.1.3.

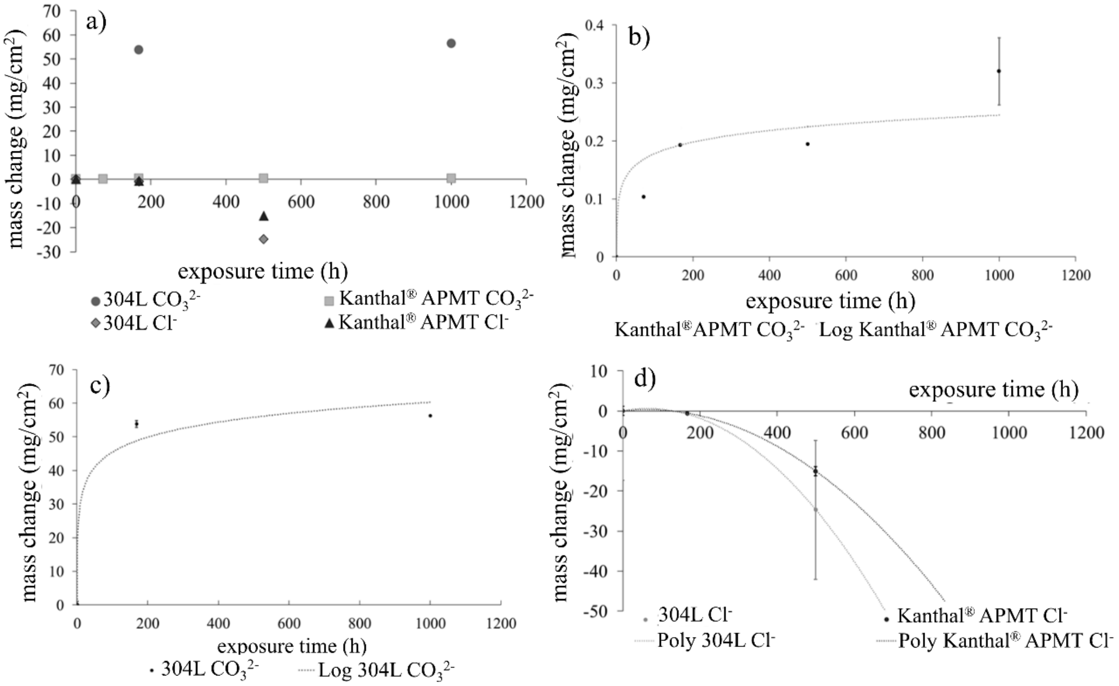

*Figure 5.3 **a**) Mass change plots for 304L and Kanthal® APMT in carbonate and chloride melts at 800°C. **b**) Mass gain of Kanthal® APMT in carbonate melt, showing the trend line. **c**) Mass gain of alloy 304L in carbonate melt, showing the trend line. **d**) Mass losses of 304L and Kanthal® APMT in chloride melt, with trend line. Note the difference in the scales. **b**)-**d**) The error bars indicate the minimum and maximum values around the average value; In the cases when error bars are not shown, the scatter in mass change are smaller than the apparent size of the symbols used. Reproduced with permission from Elsevier [77].*

5.1.1 Corrosion Performance of 316H and Kanthal$^{®}$ APMT in Nitrate Melt at 650 °C

Electron microscopy and XRD analysis were used to assess the corrosion performance of the alloys in Solar Salt. In addition, the FactSage databases and software were used to calculate the Gibbs' free energy for potential corrosion reactions to illustrate our findings.

Table 5.1 summarises the XRD analyses of the chromia- and alumina-forming alloys exposed to alkali nitrate, carbonate, and chloride melts (see **Paper I** (a)). The detection of alloy signals, for example, for Kanthal$^{®}$ APMT in alkali carbonate melt, indicates a thin scale.

Table 5.1 Summary of the XRD analyses from Paper I (a) for chromia- and alumina-forming alloys exposed to different salt melts.

Exposure conditions	Alloys	Exposure time	Corrosion products detected via XRD-analysis	XRD alloy signal
Nitrate melt, air, 650 °C	316H	168	$NaFeO_2$	Not detected
		1000		
	Kanthal$^{®}$ APMT	168	$NaAlO_2$ and $NaFeO_2$	Detected
		1000		
Carbonate melt, CO_2, 800 °C	304L	168	$LiFeO_2$	Not detected
		1000		
	Kanthal$^{®}$ APMT	168	α-$LiAlO_2$	Detected
		1000	α- and γ-$LiAlO_2$	
Chloride melt, Ar, 800 °C	304L	168	MgO	Detected
		500		
	Kanthal$^{®}$ APMT	168	$MgAl_2O_4$, $MgCr_{0.086}Al_{1.914}O_4$ (traces) and Laves phase $MoFe_2$	
		500		

Table 5.2 summarises the SEM/EDX findings for the chromia- and alumina-forming alloys exposed to the different salt melts. Based on the SEM/EDX investigations together with XRD analysis, the corrosion propagation of alloys immersed in molten alkali nitrate at 650°C can be schematically depicted, as in Figure 5.1 Path A Case I for Kanthal$^{®}$ APMT and Case III for 316H, respectively. Both alloys 316H and Kanthal APMT formed an AMO_x scale at the alloy/melt interface. The oxide scale was comprised of an outwards growing alkali-bearing species, either sodium aluminate or sodium ferrite, and an inner oxide zone, which is protective in the case of Kanthal APMT and a permeable chromia layer in the case of 316H. Finally, internal nitridation was noted in the case of 316H. However, the degree of protection provided by each alloy differed remarkably. Exposing 316H to Solar Salt for at least 1000 h resulted in four corrosion zones, (see **Paper I** (a)).

The EDX mapping reveals Cr-rich precipitates beneath the oxide scale. Internal nitridation, the capture of chromium by the nitrogen diffusion into the bulk alloy, also inhibits further formation of a protective chromia scale.

Kanthal APMT exhibited good corrosion behaviour compared to 316H. A smooth sodium aluminate scale covered the surface of the Kanthal APMT samples after exposure to Solar Salt at 650 °C for 168 h and 1000 h, as shown in Figure 5.5. After 1000 h of exposure, local nodules of sodium ferrite were found; in agreement with the XRD findings. However, the presence of an alumina scale beneath these nodules indicated an early stage of sodium ferrite formation and the inability of these nodules to grow further.

Unlike 316H, no internal nitridation was detected in Kanthal APMT samples. However, it is essential to pinpoint that AlN formation is thermodynamically spontaneous, and in case of defects in the outer scale allow for nitrogen ingress into the alloy. This means that the aluminium activity in the bulk may decrease through AlN formation. Therefore, it is paramount to sustain the aluminium oxide scale at the surface. See the thermodynamic calculations in Table 5.3 for relevant Gibb's free reaction energies at 650°C.

Table 5.2 Summary of SEM/EDX inspections of chromia and alumina-forming alloys in different salt melts.

Exposure conditions	Alloys	Outward growing zone	Inward growing zone (inner)	Internal attack
Nitrate melt, air, 1000 h, 650 °C	316H	$NaFeO_2$	Mn, Ni-enriched oxide zone and Cr-rich scale	Nitridation, 6 μm beneath the oxide scale (Case III, Figure 5.1)
	Kanthal® APMT	$NaFeO_2$ (nodules)	$NaAlO_2$	Not detected
Carbonate melt, CO_2, 1000 h, 800 °C	304L	$NaFeO_2$	Heterogeneous oxide zone: Cr-rich Fe-Cr spinel, Fe oxide, and high Ni-fractions zone	Detected, severe attack (increase with time), Case III (168 h) and IV (1000 h), Figure 5.1
	Kanthal® APMT	γ-$LiAlO_2$	α-$LiAlO_2$	Not detected
Chloride melt, Ar, 1000 h, 800 °C	304L	Magnesium oxide (Case V, Figure 5.1)		Cavities
	Kanthal® APMT	$MgAl_2O_4$, MgCrAl oxide (traces) (Case V, Figure 5.1)	Molybdenum-rich intermetallic phase (Laves phase $(Fe_{0.75}Cr_{0.25})_2Mo$), and traces of Al_2O_3	Cavities surrounded by environmentally induced precipitates (Case VI, Figure 5.1)

Table 5.3 Gibb's free energy of selected corrosion reactions in a nitrate melt at 650°C.The experimentally verified species are highlighted in bold font. $NaCrO_2$ was not observed in the outwards growing oxide scale, supposedly due to further oxidation to Cr(VI) and dissolution into the melt. On the other hand, CrN has been detected. FactSage 7.3 databases were used [105].

No	Reaction	ΔG_{923K} kJ /[mol metal]
(1)	Al (s) + $NaNO_3$ (l) → **$NaAlO_2$ (s)** + NO (g)	-676
(2)	Cr (s) + $NaNO_3$ (l) → $NaCrO_2$ (s) + NO (g)	-376
(3)	Fe (s)+ $NaNO_3$ (l) → **$NaFeO_2$ (s)** + NO (g)	-258
Considering internal nitridation: Only CrN was observed		
(4)	8 Al (s) + 3 $NaNO_3$ (l) → 3 $NaAlO_2$ (s) + Al_2O_3 (s) + 3 AlN (s)	-539
(5)	8 Cr (s)+ 3 $NaNO_3$ (l) → 3 $NaCrO_2$ (s) + Cr_2O_3 (s) + 3 **CrN (s)**	-299
(6)	23 Fe (s) + 4 $NaNO_3$ (l) → 4 $NaFeO_2$ (s) + Fe_3O_4 (s) + 4 Fe_4N (s)	-88

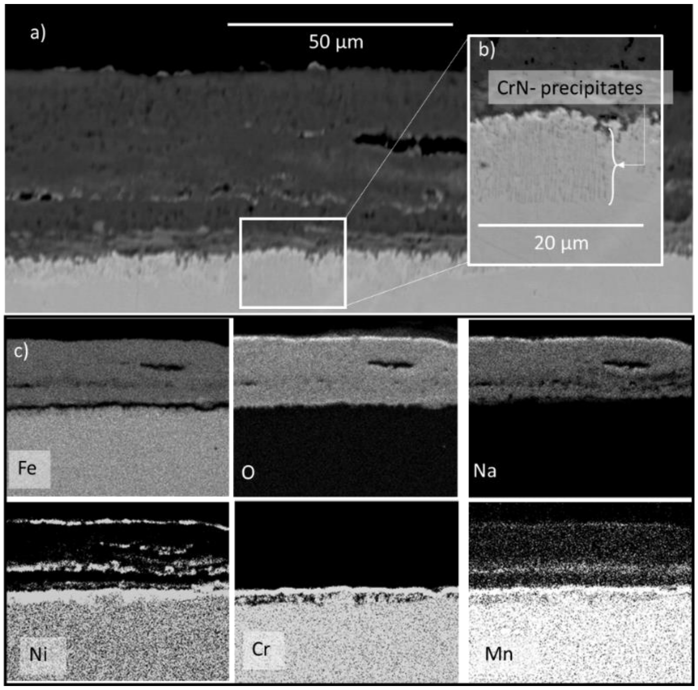

Figure 5.4. a) Backscatter electron microscopy image of 316H sample cross-section after 1000 h exposure to Solar Salt. b) Higher magnification of the zone beneath the oxide layer highlighted in image a). c) Element maps of the oxide scale corresponding to image a). Reproduced with permission from Elsevier [77].

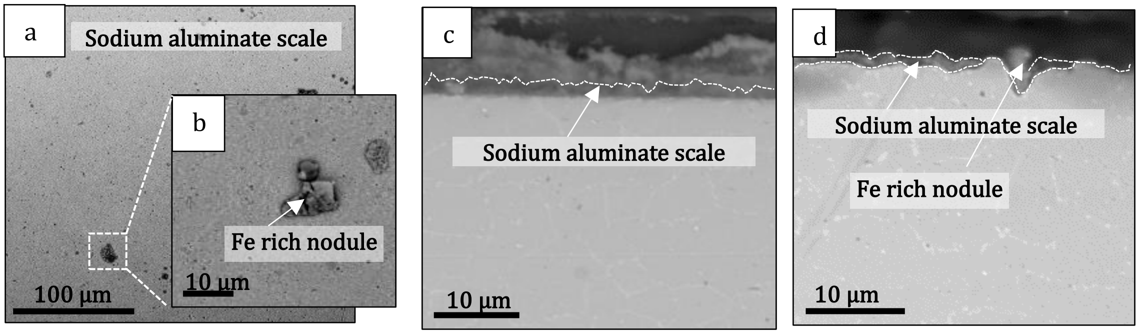

Figure 5.5 Backscatter electron images of Kanthal® APMT samples after exposure to solar salt. a) and b) top view after 168 h. Cross-section after c) 168 h and d) 1000 h. Reproduced with permission from Elsevier [77].

5.1.2 Corrosion Performance of 304L and Kanthal® APMT in Carbonate Melt at 800 °C

The XRD analysis of 304L showed spinel oxide and lithium-containing oxides, in agreement with findings in the literature [106, 107]. The Kanthal APMT diffractograms showed signals for only one crystal structure after 168 h exposure, which was identified as α-lithium aluminate. After 1000 h, an additional crystal structure signal was detected, which was identified as γ-lithium aluminate (see **Paper I** (a)).

Figure 5.6 (a and b) shows large octahedral crystallites completely covering the 304L alloy surface after 168 h of exposure to alkali carbonate melt. XRD identified these fast-growing crystallites as lithium ferrite, which agrees with previous studies [108-111]. This finding was supported by the reaction energies calculated in **Paper I (**b), Section C. The corrosion propagation of 304L in carbonate melt after 168 h and 1000 h are schematically illustrated in Figure 5.1, Cases III and IV, respectively. For a detailed analysis of the corrosion products' microstructures, topography, and chemistry, see Table 5.1 and **Paper I** (a).

Gibb’s free reaction energy for lithium ferrite formation by reacting iron with lithium carbonate was found to be exothermic, whereas $NaFeO_2$ was endothermic considering the same reactants apart from the alkali ion species. This also clarifies the absence of $NaFeO_2$ in the corrosion products, see Table 5.4. For the detailed calculations, see **Paper** I (b), section C [Eqs. (7) and (8)].

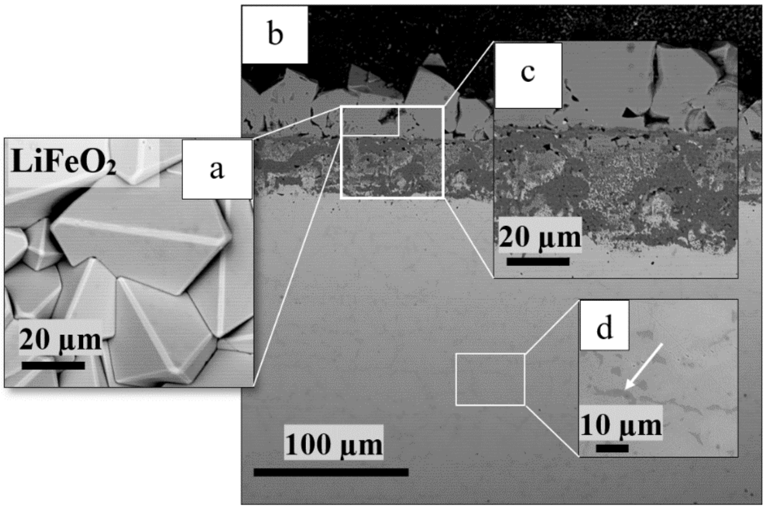

Figure 5.6 ***a****) SEM image of surface morphology,* ***b****) SEM image of a cross-section of the 304L alloy after exposure to carbonate melt at 800°C for 168 h. Higher magnification cross-section showing the internal oxidation zone after168 h* ***c)****, and chromium carbide precipitates after 168 h* ***d****). Reproduced with permission from Elsevier [77].*

Figure 5.6 (d)) shows that carbon permeates these non-protective oxides and captures chromium by precipitating chromium carbide particles. The precipitation of chromium carbides is critical for sample corrosion resistance. It lowers the chromium activity in the alloy, thereby hindering the outward diffusion of chromium to the metal oxide interface and, consequently, forming a protective chromia oxide scale. In addition, these chromium carbide precipitates change the microstructure and mechanical properties of the alloy [112].

The severe internal attack observed for 304L in the carbonate melt point towards a high mass gain. However, the mass gain is stagnant in Figure 5.3 (c). This could be due to the dissolution of metal ions into the carbonate melt. This is substantiated by the melt colour observed after the exposures; the salt has been collected for future ICP-OES analysis. In addition, thermodynamic calculations show that chromia reacts exothermically with lithium carbonate and CO_2 at 800°C to form lithium chromate (see **Paper I** (b), section C). These findings are in agreement with a previous study [113].

In strong contrast to 304L, Kanthal APMT showed a high corrosion resistance in the carbonate melt by forming a thin slow-growing oxide scale. Thermodynamic calculations were made to predict the corrosion products that can form. It was found that both aluminium and chromium can interact with sodium and lithium carbonates exothermally, which means that the reaction is spontaneous. However, the formation of lithium aluminate has the highest exothermicity, (see Section C; Eqs. (9-11)).

Table 5.4 Gibb's free energy of selected corrosion reactions in a carbonate melt at 800 °C. Experimentally verified species are highlighted in bold font. $NaFeO_2$, $NaCrO_2$ and $NaAlO_2$ were not observed in the outwards growing oxide scale, while $Cr_{23}C_6$ has been detected. Databases from Factsage 7.3 were used [105].

No	**Reaction**	**ΔG_{1073K} kJ /[mol metal]**
(7)	$2\ Fe\ (s) + Na_2CO_3\ (l) + 2\ CO_2\ (g) \rightarrow 2\ NaFeO_2\ (s) + 3\ CO\ (g)$	+22
(8)	$2\ Fe\ (s) + Li_2CO_3\ (l) + 2\ CO_2\ (g) \rightarrow \mathbf{2\ LiFeO_2\ (s)} + 3\ CO\ (g)$	-7
(9)	$2\ Al\ (s) + Li_2CO_3\ (l) + 2\ CO_2\ (g) \rightarrow \mathbf{2\ LiAlO_2\ (s)} + 3\ CO\ (g)$	-414
(10)	$2\ Al\ (s) + Na_2CO_3\ (l) + 2\ CO_2\ (g) \rightarrow 2\ NaAlO_2\ (s) + 3\ CO\ (g)$	-393
(11)	$2\ Cr\ (s) + Na_2CO_3\ (l) + 2\ CO_2\ (g) \rightarrow 2\ NaCrO_2\ (s) + 3\ CO\ (g)$	-99
(12)	$69\ Cr\ (s) + 23\ Na_2CO_3\ (l) + 40\ CO_2\ (g) \rightarrow 46\ NaCrO_2\ (s) + \mathbf{Cr_{23}C_6\ (s)} + 57\ CO\ (g)$	-70

Unlike 304L, the Kanthal® APMT sample surface was covered by a smooth layer comprising very small α-$LiAlO_2$ crystallites, as shown in Figure 5.7 (a). Interestingly, after 1000 h of exposure, some large prismatic crystallites appeared (see Figure 5.7 (b)). The appearance of these prismatic crystals is associated with the second phase signal that arises in the XRD analysis, defined as γ-$LiAlO_2$. Several groups have investigated the thermophysical properties of the two lithium aluminate polymorphs [114-117]. α-$LiAlO_2$ was found to be stable at temperatures up to ~747°–777°C, after which the $\alpha \rightarrow \gamma$-$LiAlO_2$ phase transformation occurs. This transformation is influenced by different parameters, such as the operating temperature, environment, and exposure time. It is essential to monitor this $\alpha \rightarrow \gamma$-$LiAlO_2$ transformation from the corrosion perspective, since the small α- $LiAlO_2$ crystallites form a protective film [16], while the large γ-$LiAlO_2$, which nucleates and grows individually, does not confer the same level of corrosion resistance. Therefore, the $\alpha \rightarrow \gamma$-$LiAlO_2$ phase transformation is undesirable. This transformation may explain the greater uncertainty related to the mass change value of Kanthal® APMT, which increased to the end of the exposure after 1000 h. The mass gain is accelerating [Figure 5.3 (b)] simultaneously with the appearance of the γ-$LiAlO_2$ phase. The corrosion propagation patterns of Kanthal® APMT in carbonate melt after 168 h and 1000 h are schematically illustrated in Figure 5.1 Case I and II, respectively.

Compared to 304L, the overall mass gain of Kanthal® APMT was two orders of magnitude lower, and neither aluminium nor chromium leaching from the alloy into the melt was detected after 1000 h. However, the impact of the $\alpha \rightarrow \gamma$-$LiAlO_2$ phase transformation on the long-term performance of the alloy must be considered.

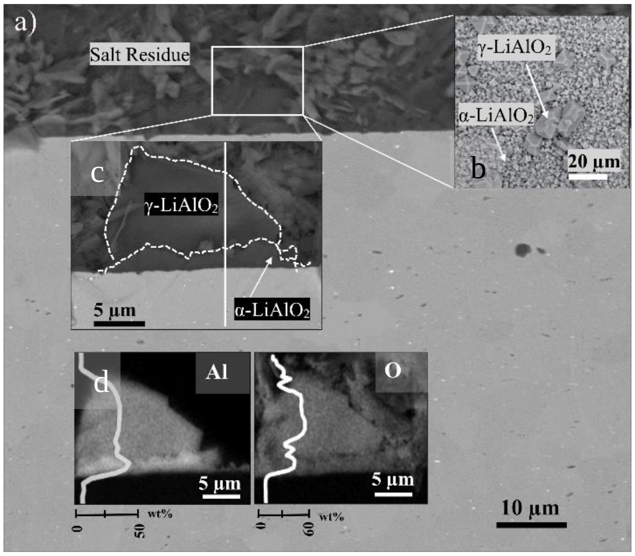

Figure 5.7 ***a****) Overview back-scatter electron microscopy image of a cross-section of Kanthal® APMT exposed to molten carbonate salt mixture at 800°C for 1000 h.* ***b****) Top-view image of the surface.* ***c****) Higher magnification of the cross-section.* ***d****) Aluminium and oxygen elemental maps of position* ***c****) and corresponding line-scans. Reproduced with permission from Elsevier [77].*

5.1.3 Corrosion Performance of 304L and Kanthal® APMT in Chloride Melt at 800 °C

As shown in Table 5.1, Kanthal® APMT exhibited a distinct diffraction pattern from a molybdenum-rich intermetallic phase, a so-called ‘Laves phase’. The position and role of the Laves phase will be discussed later in this section. For a description of the XRD analyses of 304L and Kanthal® APMT immersed in chloride melt, see **Paper I** (a).

It is important to emphasize that the oxidation reactions that occur during the chloride melt exposures are limited by the contaminating oxygen in the Ar gas and the residual humidity of the salt, as clarified in Section 4.2. The only oxides that can form under these extreme conditions must have very high thermodynamic stability. Among these oxides are magnesium oxide and magnesium aluminate [9].

Recalling the mass change data presented in Figure 5.3 (d), both tested alloys underwent accelerating mass loss, with a more pronounced effect on 304L compared to Kanthal® APMT. In addition, the overall coupon thickness decreased as documented in **Paper I (b)**, Section B. The dissolution processes of alloy elements have also been reported in previous studies [118].

Microstructural analysis of the 304L samples revealed that the chloride melt immediately leached the alloy elements, (see **Paper I** (a)). The $MgCl_2$ /KCl eutectic melt reacted with oxygen impurities to induce MgO precipitation on the alloy surface. The SEM/EDX analyses revealed the presence of MgO precipitates all over the surfaces of the 304L samples after 168 h of exposure. EDX elemental mappings detected alloy species, such as chromium and nickel, in the salt residue covering the top of the sample, which is in agreement with the Ding et *al.*, who reported chromium dissolution into chloride melt [45, 55]. As these metals leached from the bulk alloy, cavities were formed and reached a depth of ~10 µm into the alloy's microstructure after 168 h. After 500 h, a chromium depletion zone with depth >100 µm was observed in the EDX maps [see Figure 5.8 (c)]. The chromium concentration within this zone was only 2%; see line-scan Figure 5.8 (c). In addition, cavities were found within the depletion zone and reached more than 150 µm into the alloy. The cavities were filled with MgO and traces of chlorides; these findings are similar to those of a previous study [45], and might indicate a three-dimensional cavity network into the specimen.

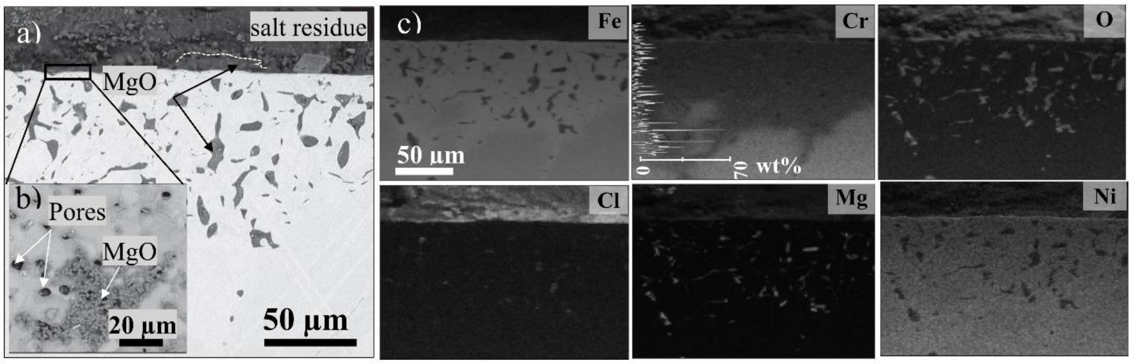

Figure 5.8 Alloy 304L cross section after exposure to molten chlorides at 800 °C,500 h, and corresponding EDX element maps c). The chromium element map in c) is extended by a line scan to highlight chromium depletion. The higher magnification in the top view image b) shows magnesium oxide and pores distributed over the surface of the sample. With permission from Elsevier [77].

The corrosion propagation patterns of 304L and Kanthal® APMT in chloride melt after 168 h, and 1000 h are schematically illustrated in Figure 5.2, Path B (Case V). No oxide scale was formed; instead, cavities and environmentally induced precipitates were formed, Figure 5.2, (Case VI).

It is important to bear in mind the crucial effect that humidity (as an impurity) has on the alloys. Previous publications have identified water as an impurity that has the greatest acceleration effect on stainless steel corrosion [91, 119-121]. Despite the use of an additional drying step for the chloride salts in inert gas before exposure, the influence of residual humidity was significant. However, as discussed in Chapter 3.3, controlling the humidity is a significant cost factor for CSP plants, wherein thousands of tons of salt are required for the TES tanks.

As mentioned above, the XRD spectra of Kanthal® APMT revealed the presence of a molybdenum-rich intermetallic phase, in addition to $MgAl_2O_4$. EDX cross-section spot analysis confirmed the presence of alumina particles on the top surface of the sample [Figure 5.9 (a, b)]. A bright Z-contrast in the subsurface region was also observed [Figure 5.9 (b)]. Interestingly this bright Z-contrast region was due to molybdenum enrichment. This enrichment was sufficient to stabilise the Laves-phase precipitates.

Detailed thermodynamic calculations regarding the stability of the Laves phase are provided in **Paper I** (b), Section D. The thermodynamic calculations confirm the presence of a two-phase regime at 800°C, comprising BCC and C14 Laves phase with the approximate composition of $(Fe_{0.75}Cr_{0.25})_2Mo$ deduced for the latter.
After 168 h of exposure, the Kanthal® APMT had not yet suffered from an internal attack. However, after 500 h, the chloride melt managed to attack the alloy and change its integrity by selectively leaching aluminium, creating a cavity network to a depth of 280 µm.

Figure 5.9 (c-e) shows that only fragments of alumina remained at the surface. In addition, a pattern of pores was detected at the alloy surface. The line-scan in Figure 5.9 (h) shows the deep depletion of the aluminium in a cross-sectional analysis of the attacked sample. Similar to what was observed for 304L, the cavities were filled with MgO and traces of chlorides. Aluminium leached most efficiently through the cavity network, leaving a molybdenum-rich Laves-phase rim around several individual cavities. After 500 h, these Laves-phase rims around cavities were measured at the minimum distance of ~100 µm from the metal/salt interface. In conclusion, the Laves-phase precipitates appeared transiently during the overall leaching process. It was observed that they had already disappeared from the upper region of the sample, indicating delayed chromium leaching from the said phase.

As shown in Figure 5.3 (d), the overall mass loss for Kanthal APMT was lower than that for 304L. This difference in mass loss between the two alloys can be attributed to the lower degree of chromium leaching found for Kanthal APMT. However, Kanthal APMT suffered from a deeper internal attack which compromised the integrity of the alloy. Gomez-Vidal *et al.* have studied the corrosion performance of a pre-oxidised Kanthal APMT in contact with the chloride melt and shown that this procedure did not result in Laves-phase precipitates [44].

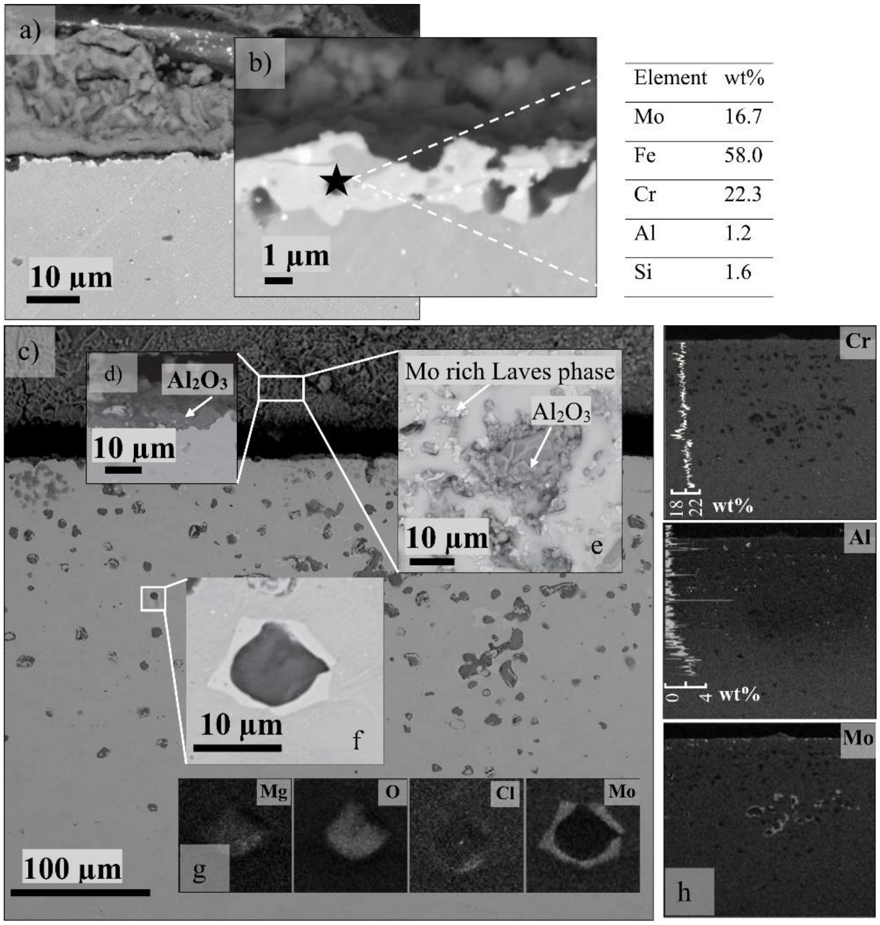

Element	wt%
Mo	16.7
Fe	58.0
Cr	22.3
Al	1.2
Si	1.6

*Figure 5.9 Cross-section of Kanthal® APMT after exposure to molten chlorides at 800 °C for: **a**) 168 h, and **c**) 500 h, and the corresponding EDX elemental maps **b**) and **g, h**). The aluminium and chromium elemental maps in **h**) are extended with line-scans to highlight the aluminium depletion and the lower degree of chromium leaching. Higher magnification of the top-view image **e**), showing how magnesium oxide and pores are distributed over the surface. The higher magnification cross-section in **d**) shows a fragment of the alumina scale remaining at the surface. **f**) Laves-phase rims around the voids. Reproduced with permission from Elsevier [77].*

5.2 Ranking the Corrosion Performance of Five Alumina-Forming Alloys in Carbonate Melt at 800 °C

As discussed earlier [**Paper I** (a and b)], Kanthal® APMT showed potential for applications in contact with carbonate melt, particularly for the next-generation CSP plants. Therefore, it is essential to address the following questions: *Will all alumina-forming alloys show the same good corrosion behaviour? Do the different chemical compositions of the alloys play a role in their resistance to corrosion by the carbonate melt?* Moreover, there is a need to monitor the interesting α/γ-$LiAlO_2$ transition.

In this context, referring to **Paper II**, the scale formation and phase transition for five alumina-forming alloys in contact with carbonate melt were investigated, and the α/γ–$LiAlO_2$ phase fractions were assessed using the XRD Rietveld refinement. Cross-sectional and top-view electron microscopy images were combined with these results. The mass change values were calculated and used as complementary data. As cleaning the samples of salt residues is challenging, these mass change values are difficult to acquire. Combining the results of all of these analyses generates a comprehensive picture of the corrosion behaviour of the selected alloys.

This study focuses on the oxide scale transformation mechanism and the α/γ-$LiAlO_2$ phase transition.

It is important to note that the concept adopted here was introduced by Evans et al. in 1978, who proposed the stress-assisted formation concept for a duplex oxide scale; this duplex oxide scale consisted of tetragonal and monoclinic zirconia polymorphs on zircaloy-1 [122]. Following the same principle, the growth of both α-$LiAlO_2$ and γ-$LiAlO_2$ at 800°C was discussed in this licentiate study. Evans et al. reported that, upon oxidation of zircaloy under compressive stress, a stress-stabilised tetragonal zirconia morphology emerged at the metal/oxide interface, which subsequently relaxed to a monoclinic lattice. As shown in the Temperature–Pressure phase diagram in Figure 5.10 [123], tetragonal ZrO_2 is allowed to form at a substantially lower temperature than its ambient pressure phase transition point, depending on the magnitude of the compressive stress. To date, several research studies have investigated and predicted a limiting scale thickness (also known as "steady-state thickness") [124, 125]. Such detailed investigations are crucial given their technological importance in various nuclear power applications [124].

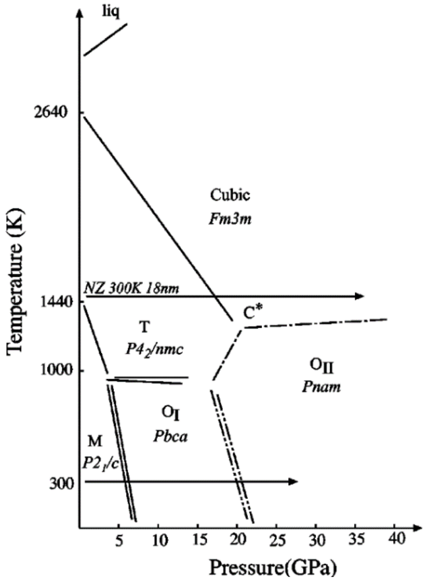

Figure 5.10 Pressure-Temperature phase diagram of zirconia. Source: Bouvier, P., et al, 2000. Reproduced with permission from Physical review. B [123]. https://doi.org/10.1103/PhysRevB.62.8731.

In the study of Evans et al. [122], the emphasis was on the universality of their concept of a stress-stabilised inner oxide scale underneath another stress-relieved polymorph. In our case, the stress stabilisation could contribute to the otherwise thermodynamically unstable α-$LiAlO_2$ crystal structure at 800°C. We assumed a limiting steady-state thickness of the α-$LiAlO_2$ inner oxide layer based on our belief that the $\alpha \rightarrow \gamma$-$LiAlO_2$ transformation is one of the examples proposed by Evans et al. [122] It is worth mentioning that the density of γ-$LiAlO_2$ is 25% lower than that of α-$LiAlO_2$. In Figure 5.11, the crystal structures of α- and γ-$LiAlO_2$ are visualised. For α-$LiAlO_2$, the layered packing of aluminium and lithium ion polyhedrons is highlighted along the *c*-axis. In contrast, the γ-$LiAlO_2$ crystal structure consists of alternating Li/Al tetrahedrons [126].

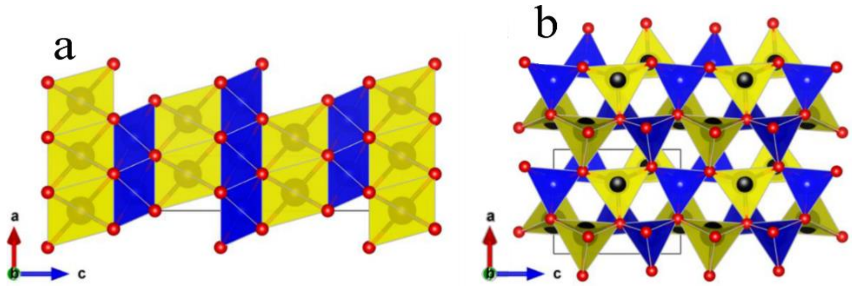

Figure 5.11 Three-dimensional polyhedral visualisation of a) α-$LiAlO_2$ and b) γ-$LiAlO_2$ crystal [126, 127]. Reproduced with permission from Elsevier [128].

Mass change measurements are used to evaluate sample corrosion. However, as illustrated in Chapter 4.3, the mass change data must be interpreted carefully due to the loss of soluble corrosion products upon sample rinsing. Nonetheless, mass change data, combined with other observations, provide insights into scale formation and growth.

It is clear from Figure 5.12, that all the five Fe(Ni)CrAl alloys have somewhat low mass gain values. After 1000 h of exposure, Nikrothal$^{®}$ PM58 obtained the highest mass gain. Lower but similar mass gains were seen in Kanthal$^{®}$ APMT and Kanthal$^{®}$ AF, and the lowest mass gain was obtained for Kanthal$^{®}$ EF 101. Kanthal$^{®}$ EF 100, in contrast, showed an initial mass loss.

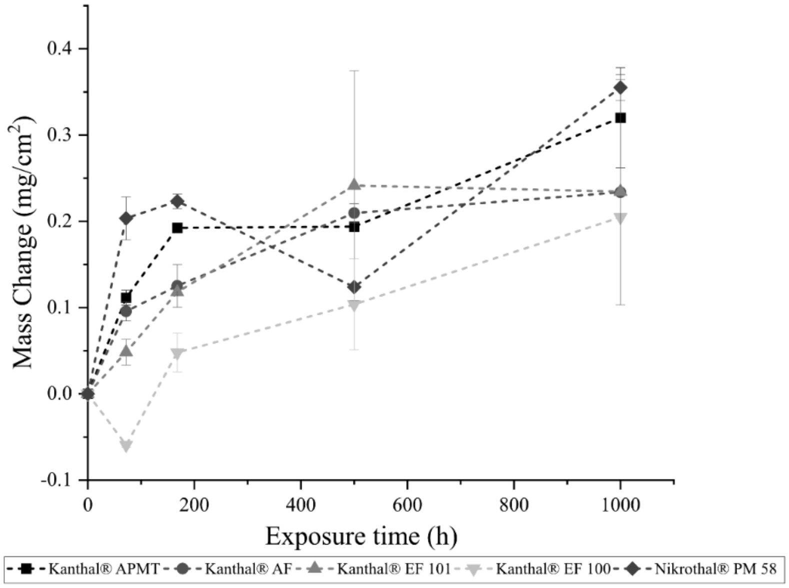

Figure 5.12 Overall mass change behaviour of the selected alumina forming alloys immersed in alkali carbonate at 800 °C as a function of exposure time. Reproduced with permission from Elsevier [128].

Table 5.5 depicts and utilises the mass change values, and α-$LiAlO_2$ scale thickness measurements obtained from microscopy investigations. The obtained values are compared to phase fractions determined by XRD Rietveld analysis.

The corrosion performance of the selected alumina-forming alloys can be differentiated into two behaviour categories. The first behaviour was referred to as the "normal" $LiAlO_2$ formation without additional cations, e.g., Fe or Cr ions. Transformation of an inner α-$LiAlO_2$ scale growth into a dominating outwards growth of γ-$LiAlO_2$ crystals has been documented. The second behaviour was referred to as the "deviating" formation and transformation of $LiAlO_2$, where the oxidation of Fe(Ni)CrAl alloys involved transient alkali oxide formation and pegging incorporating ternary cationic species.

5.2.1 "Normal" Formation and Transformation of $LiAlO_2$

This section will present, discuss and summarise the main findings regarding the corrosion behaviour of FeCrAl alloys that have "normal" formation and transformation of $LiAlO_2$. As stated earlier, besides the aluminium, no other cationic species from the alloy were found as scale components. Basically, the $LiAlO_2$ formed was as pure as in the synthesis route of Lehmann and Hasselbarth [129]. Since the results showed very similar corrosion behaviour among the three "normal" behaving alloys, XRD spectra of only one "normal" behaving alloy are presented. These alloys were Kanthal® APMT, Kanthal® AF and Kanthal® EF 101.

Figure 5.13 shows the XRD analysis of Kanthal® EF 101 exposed to carbonate melt at 800 °C. Short-term exposure (72 h and 168 h) revealed that only α-$LiAlO_2$ was formed. With longer exposure durations (500 h and 1000 h), signals for the γ-$LiAlO_2$ phase appeared. The α/γ $LiAlO_2$ phase ratios were measured and quantified by Rietveld analysis, and are summarised in Table 5.5.

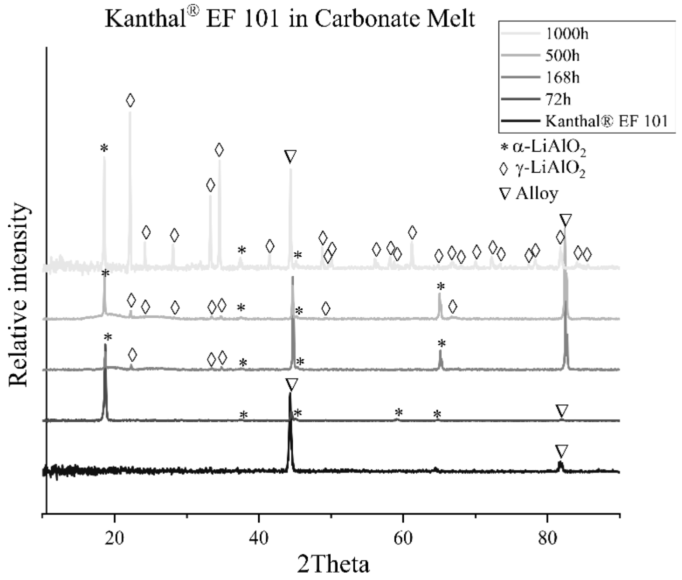

Figure 5.13 XRD patterns of Kanthal® EF 101 after exposure to alkali carbonates in CO_2 at 800 °C for different exposure times. Reproduced with permission from Elsevier [128].

Key top-view images of Kanthal® APMT, Kanthal® AF, and Kanthal® EF 101 exposed to ternary carbonate melt over time are plotted in Figure 5.14. The three "normally" behaving alloys showed very similar features, where small α-$LiAlO_2$ crystals entirely covered the surface after short term exposures (72 h and 168 h), Case I (Figure 5.1). The larger prismatic γ-$LiAlO_2$ crystals emerged after longer exposure times, such as 500 h and 1000 h, Case II (Figure 5.1)

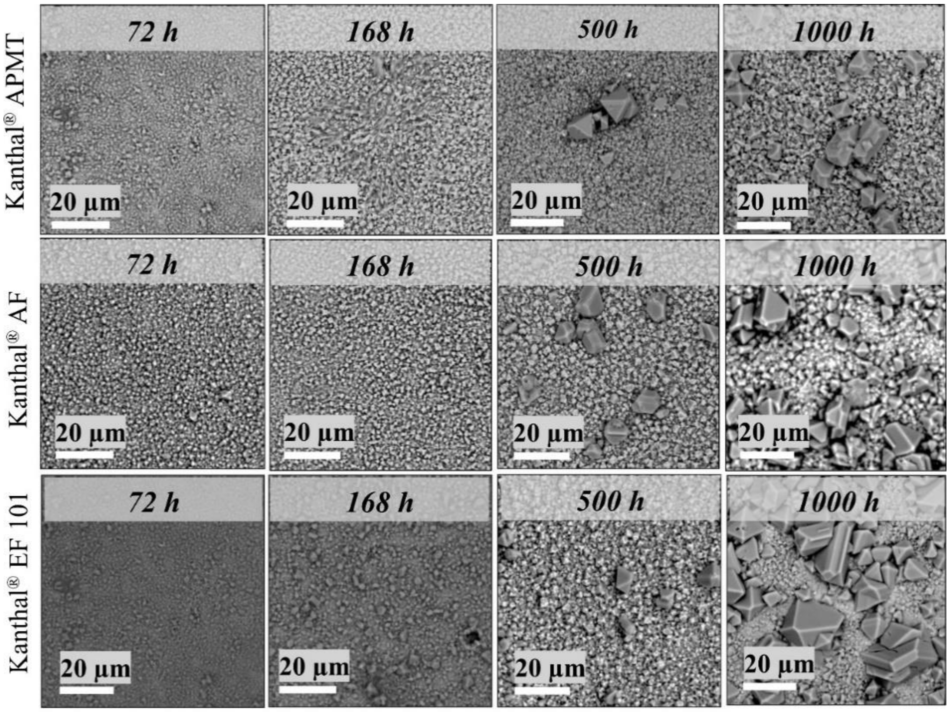

Figure 5.14 Top view electron microscopy images for the three alloys with a "normal" $LiAlO_2$ formation behaviour in the carbonate melt for different exposure times. The large crystals are γ- $LiAlO_2$, small crystals are attributed to α- $LiAlO_2$. Reproduced with permission from Elsevier [128].

Investigations of cross-sectional samples of Kanthal® EF101 showed a distinct double-layer structure composed of a compact inner α-$LiAlO_2$ scale and outer γ-$LiAlO_2$ crystals (see **Paper II**). The slight variance in the Z-contrast between the inner and outer layers corresponds to the density difference between the α- and γ-$LiAlO_2$. Since both forms of $LiAlO_2$ have the same atomic composition, the backscattered electrons will have a higher probability of scattering back into the detector when interacting with a more densely packed structure [103].

The average scale thicknesses of the "normal" behaving $LiAlO_2$-forming alloys were measured (Table 5.5). It is clear that Kanthal® APMT has the thickest α-$LiAlO_2$ scale among the "normal" behaving alloys and that its thickness increases over time.

In the scenario with "normal" formation of $LiAlO_2$, the measured mass gain $\Delta m_{(measured)}$ represents the oxygen and lithium uptake into the scale. To calculate the amount of $LiAlO_2$ substance (n), the mass gain measured for the contribution of aluminium from the alloy (41% of the molar mass M_{LiAlO2}) is corrected, and then divided by the total M_{LiAlO2}, as in Eq. (5.1). A homogeneous scale is formed at the surface with the α-$LiAlO_2$ phase exhibiting the "normal" formation behaviour with a mean thickness X(α). An approximate total mass of α-$LiAlO_2$ and, consequently, an amount of substance, n(α), can be determined by multiplying the mean thickness X(α) by the α-$LiAlO_2$ theoretical density, which is derived from the crystallographic database [126], and the sample area.

$$n\,(LiAlO_2\;total) = \;n(\alpha) + n(\gamma) = \frac{\Delta m(measured) \cdot 1.69}{M(LiAlO_2)} \qquad (5.1)$$

By combining the gravimetric and microscopy data, the α/γ-phase ratio was calculated for each sample in the "normal" $LiAlO_2$ formation scenario using Eq. (5.1). Such calculated ratios can quantify the contribution of the α-$LiAlO_2$ scale to the total mass gain. In addition, quantification of the α/γ-$LiAlO_2$ ratios was performed using the Rietveld refinement for the XRD patterns of each sample. These two methods of calculating α/γ-$LiAlO_2$ ratios were compared, to ensure confidence in the findings and more-accurate assumptions. Such quantification provides information about the evolution of the γ-$LiAlO_2$ coverage of the sample surfaces. Of note, the scale thickness and mass gain used for the calculations were derived from two different coupons; however, they were exposed simultaneously under the same conditions.

Figure 5.15 depicts the evolution of the α- and γ-$LiAlO_2$ phases over time, as represented by the Rietveld-refinement α/γ-phase ratio and the scale thickness. It is noteworthy that the Rietveld-derived α/γ-phase ratio, decreases after 500 h in the cases of Kanthal® APMT and Kanthal® EF101. In contrast, the average thickness continues to increase steadily. Despite the steady increase in the average thickness, such deceleration in terms of fraction percentages can be explained by the top-view images in Figure 5.14. Although individual γ-$LiAlO_2$ crystallites continue to grow significantly over time, the number of nucleation sites does not increase concomitantly; this may have influenced the slope of the Rietveld phase fraction curve shown in Figure 5.15. The rapid increases in the size and phase fraction of γ-$LiAlO_2$ might have led to the depletion of Al in the alloy. Therefore, all the 1000 h exposed samples underwent a line-scan analysis; however, the results revealed the invalidity of this assumption. Furthermore, growth of the α-$LiAlO_2$ scale was found to decelerate over time.

Table 5.5 Mean scale thicknesses for α- and γ-$LiAlO_2$, mass change Δm, gravimetrically and microscopically derived α/γ-phase ratio (calc. Eq.5.1) and Rietveld derived phase ratios (α to γ % Rietveld). The Table's n.a. (not available) data is attributable to duplicate sample loss in the repeated experiment due to alumina crucible breakdown during cooling.

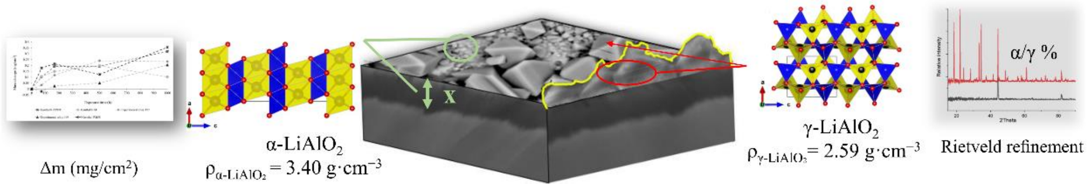

Exposure Time		Δm (mg/cm^2)	$X_{measured}$ (µm)	α to γ % calc.	α to γ % Rietveld
Kanthal® APMT					
72 h	α	0.11±0.008	0.30 (Max 0.6)	97	100
	γ		-	3	0
168 h	α	0.19±n.a	0.75 (Max 2.4)	77	100
	γ		-	23	0
500 h	α	0.19±0.002	0.95 (Max 3.2)	96	63.9 ± 0.9
	γ		1.60 (Max 2.3)	4	36.1± 0.9
1000 h	α	0.32±0.06	1.80 (Max 3.2)	94	78.1 ± 1.1
	γ		5.2 (Max 8.8)	6	21.9± 1.1
Kanthal® AF					
72 h	α	0.10±0.01	0.45 (Max 0.7)	94	100
	γ		-	6	0
168 h	α	0.13±0.02	0.5 (Max 0.7)	66	85.5±2.5
	γ		0.42 (Max 0.6)	34	14.5±1.9
500 h	α	0.21±0.01	0.6 (Max 0.7)	48	70±1
	γ		0.85 (Max 4.4)	52	30±1
1000 h	α	0.23±0.13	1.13 (Max 1.8)	34	9.8±2.5
	γ		3.0 (Max4.3)	66	90.2±2.4
Kanthal® EF 101					
72 h	α	0.05±0.01	0.45 (Max 1.2)		100
	γ		-		0
168 h	α	0.12±n.a	0.47 (Max 0.6)	76	64±0.9
	γ		0.75 (Max 1.25)	24	36±0.9
500 h	α	0.24±0.13	0.52 (Max 0.7)	27	18±5
	γ		1.4 (Max 2.7)	73	82±5
1000 h	α	0.23±n.a	0.6 (Max 1.1)	51	20.2±3.8
	γ		1.7 (Max 3.5)	49	79.8±3.3

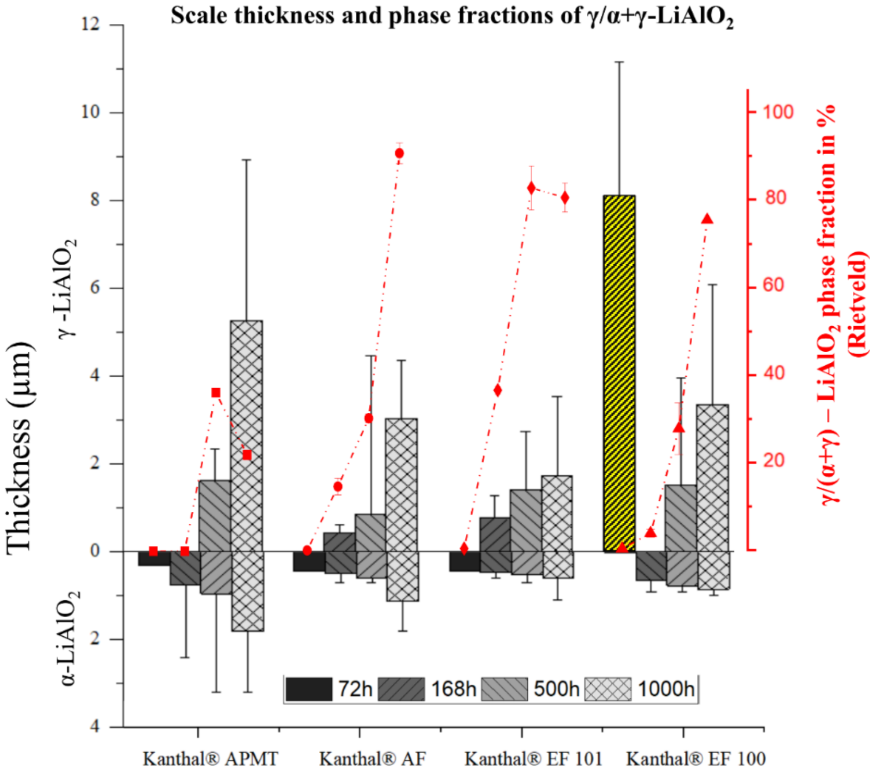

Figure 5.15 Thickness of α- and γ-$LiAlO_2$ for the four ferritic FeCrAl alloys and the corresponding results of the Rietveld analysis, Yellow column represents $LiFeO_2$ cf. section 5.2.2. Reproduced with permission from Elsevier [128].

To sum up “normal behaving alloy section” in **Paper II**, Kanthal® AF, Kanthal® APMT and Kanthal® EF101 alloys showed a "normal" $LiAlO_2$ formation behaviour. Minor deviations were observed with respect to scale thickness, crystal size, and surface roughness among the tested alloys. After 72 h of exposure to alkali carbonates at 800°C, a homogeneous covering of α-$LiAlO_2$ scale was formed, which protected against the internal oxidation and carburisation of the bulk alloy.

It is worth noting that α-$LiAlO_2$ is not thermodynamically favoured at 800°C C [114]. This raises the question as to why the α-$LiAlO_2$ scale is present at this temperature and grows with time. For this, it is essential to recall the oxidation mechanism proposed by Evans et al. for phase stabilisation under compressive growth stress [122]. Since α-$LiAlO_2$ is significantly denser than γ-$LiAlO_2$, the growing α-$LiAlO_2$ scale can accommodate higher numbers of oxygen and lithium ions in the same volume compared to γ-$LiAlO_2$, which results in absorbing growth stresses. In terms of corrosion, α-$LiAlO_2$ is the preferential crystal morphology because it forms a dense and protective scale that maintains a slow oxidation process.

In the present study, a signal for undesirable γ-$LiAlO_2$ morphology was detected in the XRD patterns after 168 h for all the ferritic alumina-forming alloys, in conjugation with the appearance of larger-faceted crystallites at the surface. The γ-$LiAlO_2$ crystallites are free-standing at the melt/oxide interphase and do not experience compressive growth stresses.

Figure 5.15 shows that the thicknesses of α- and γ-$LiAlO_2$ layers increase over time. At an earlier corrosion stage, α-$LiAlO_2$ forms and grows slowly, after which the γ-$LiAlO_2$ predominates. As discussed above, the formation and growth of α-$LiAlO_2$ rely on the presence of compressive stresses. Therefore, a steady-state behaviour of the inner scale is expected to be reached. The stress relaxation defines the limiting inner α-scale thickness into γ-$LiAlO_2$ modification at the gas/oxide interface. While the limiting α-scale thickness had not yet been reached in the present study, the rate of scale growth had already declined significantly after 1000 h, while the γ-crystallites kept on growing. The Rietveld refinement also confirmed increasing surface coverage by γ-$LiAlO_2$ over time.

According to Ribeiro et al. [130], the steady-state thickness of the α-$LiAlO_2$ layer appears to be temperature-dependent. Since α-$LiAlO_2$ is thermodynamically favourable at temperatures below 750 °C, γ-$LiAlO_2$ nucleation is unlikely to occur. Thus, it can be concluded that the formation of γ-$LiAlO_2$ results in limitation of the alloy lifetime in two ways. First, the absence of the protective α-$LiAlO_2$ scale leaves the alloy surface vulnerable to attacks by various corrosive species. Second, the rapid growth of γ-$LiAlO_2$ accelerates Al depletion from the bulk alloy and, subsequently, compromises the formation of a protective α-$LiAlO_2$ scale.

5.2.2 "Deviating" Formation and Transformation of $LiAlO_2$

Unlike the Kanthal® AF, Kanthal® APMT and Kanthal® EF101 alloys, the corrosive behaviour of the Kanthal® EF100 and Nikrothal® PM58 alloys do not follow the "normal" $LiAlO_2$ formation pattern. The so-called "deviating" formation and transformation behaviour is particularly noticeable after short-term exposure. For instance, the Kanthal® EF100 alloy surface was entirely covered with $LiFeO_2$ crystals after 72 [Figure 5.16 (c)], as confirmed by XRD analysis (see **Paper II**). Such "deviating" behaviour, however, does not seem to predominate with longer exposure times. In the case of Kanthal® EF100, the $LiFeO_2$ crystals covering the alloy surface disappeared after 168 h of exposure. This is likely due to $LiFeO_2$ dissolution into the carbonate melt, as depicted in Figure 5.16 (d) and Figure 5.16 (g).

This observation matches the observed mass loss demonstrated in Figure 5.12. Upon the dissolution of $LiFeO_2$, small crystals of α-$LiAlO_2$ start to grow. Furthermore, the growth pattern of γ-$LiAlO_2$ crystals was observed to follow the "normal" formation behaviour after exposures longer than 500 h and 1000 h.
Of note, calculation of the α/γ-$LiAlO_2$ phase ratio using the coupled gravimetric/microscopic approach via Eq. (5.1) was not applicable due to the observed mass loss by the dissolution of the initially formed $LiFeO_2$. Therefore, Rietveld refinement of the XRD patterns was employed to obtain the α/γ-$LiAlO_2$ phase ratios after exposures for 168 h, 500 h, and 1000 h. Figure 5.15demonstrates the obtained Rietveld-derived data and the mean scale thicknesses. Based on these observations, Kanthal® EF 100 alloy is classified as a "normal" behaving-$LiAlO_2$ forming alloy, after an initial transient "deviating" state. The long-term behaviour is controlled by γ-$LiAlO_2$ crystallite nucleation on the slow-growing protective α-$LiAlO_2$ scale.

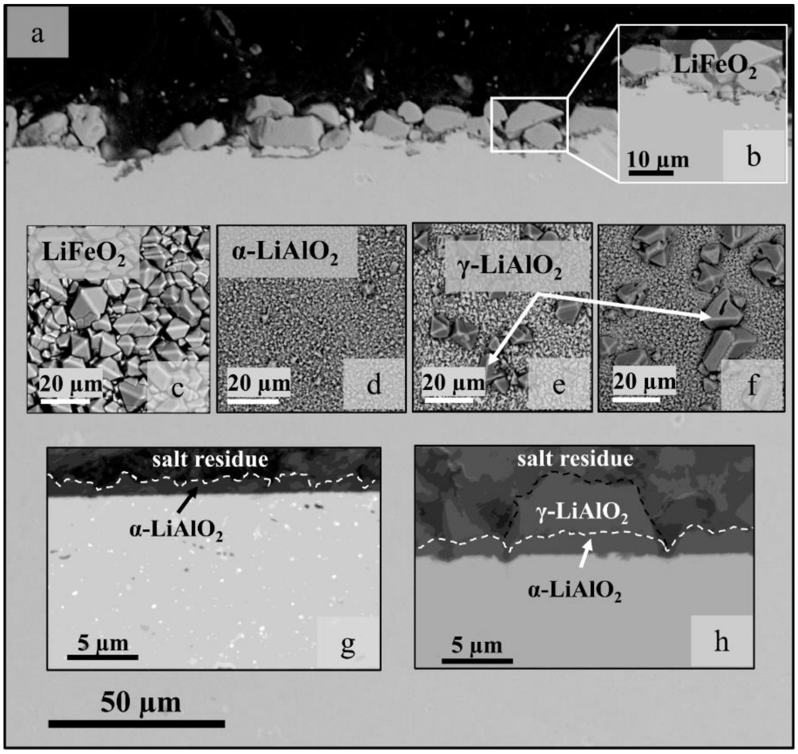

Figure 5.16 Top-view of Kanthal® EF 100 exposed to alkali carbonate melt at 800 ºC, ***a, b****) Cross-section after 72 h. Top-view image of* ***c****) 72 h, LiFeO$_2$ covers the surface,* d*)168 h, only α-LiAlO$_2$ covers the surface,* ***e****) 500 h, γ-LiAlO$_2$ crystallites appear, f)1000 h, γ-LiAlO$_2$ crystallites size increased. Cross-section after* ***g****) 168 h, and* ***h****) 1000 h. Reproduced with permission from Elsevier [128].*

A rather different "deviating" behaviour was observed for Nikrothal® PM58. Although α-LiAlO$_2$ is commonly formed during exposures at 750ºC [131], the formation of Li(Cr,Al)O$_2$ (instead of the protective α-LiAlO$_2$ scale) was observed with the austenitic alloy Nikrothal® PM58 at 800°C. Nikrothal® PM58 exposed to alkali carbonate melt for 1000 h or longer develops pegs that are filled mainly with Li(Cr,Al)O$_2$ in the sub-oxide zone, as demonstrated by the XRD (see **Paper II**) and cross-sectional microscopy analyses presented in Figure 5.17. Some fractions of aluminium-enriched scale were observed, [see Figure 5.17 (d-e)]. Point analysis of the surface, depicted in [Figure 5.17 (c-e)], demonstrated the presence of nickel and iron particles at the oxide/melt interface. These transported or overgrown alloy particles can be leached into the alkali carbonate melt. In addition, we noted an aluminium-depletion zone at a depth of approximately 14 µm in the sub-oxide region of the alloy. The aluminium content observed beneath the oxide layer was lower than the nominal composition by 1.2 wt% [Figure 5.17 (f)].

To summarise these results, the two alumina-forming alloys investigated in this study, namely Kanthal® EF100 and Nikrothal® PM58, were found to follow a "deviating" LiAlO$_2$ scale evolution.

In the case of Kanthal® EF100, the alloy adopts an initial "deviating" behaviour, forming external lithium ferrite (LiFeO$_2$) crystallites after 72 h at 800°C. For longer exposure times, a protective α-LiAlO$_2$ scale is formed, and thereafter the *α→γ*-LiAlO$_2$ transformation occurs, as described in Section 5.2.1. These findings are very similar to the observations made by Asokan et al. when comparing the oxidation behaviour of Kanthal® EF100 and Kanthal® EF101 in dry air [132]. Despite their similar chemical compositions, the Si contents of these alloys are significantly different. In the study of Asokan et al., Kanthal® EF101 grew an aluminium oxide scale in dry air, whereas Kanthal® EF100 rapidly grew iron oxide [132].

Si plays a role in forming the protective alumina scale, which possibly indicates a so-called 3rd element effect.

In this work, when Kanthal® EF101 was in contact with the carbonate melt, the 3rd element effect of Si contributed to the formation of the protective α-$LiAlO_2$. In contrast, Kanthal® EF100, which lacks the Si content, rapidly grows a covering $LiFeO_2$ scale. After reaching a sufficient thickness (~8.0 µm after 72 h), the oxygen and lithium activities are low enough to nucleate a slow-growing $LiAlO_2$ at the metal/scale interface, thereby decreasing the scale growth significantly. $LiFeO_2$ completely dissolves into the melt before 168 h, revealing a pure α-$LiAlO_2$ scale. This $LiAlO_2$ undergoes further $\alpha \rightarrow \gamma$-transformation, as described in the section on "normal" $LiAlO_2$ formation.

Nikrothal® PM58 exhibits a unique "deviating" behaviour that differs from those of the FeCrAl alloys studied. Being an austenitic alloy, the diffusion of aluminium towards the metal/scale interface is slower than is the case for the ferritic alloys [133]. The slower aluminium diffusion process is evident in Figure 5.17 (f) in the suboxide region. Even after exposure to alkali carbonates at 800°C, a covering α-$LiAlO_2$ scale failed to form; this is attributed to the fact that a steady-state supply of aluminium to the metal/scale interface is a prerequisite for maintaining an intact α-$LiAlO_2$ scale. Temperature plays a critical role, since the findings obtained at 800°C are strongly discrepant with the results of an earlier study performed in the same laboratory at 750°C, where Nikrothal® PM58 formed a slow-growing, protective α-$LiAlO_2$ scale that was sustained for at least 740 h [131].

This observation strongly agrees with the temperature-dependence of the $LiAlO_2$ phase transition studied by Danek et al. [114], where the lower temperature limit for γ-$LiAlO_2$ formation was 750°C.

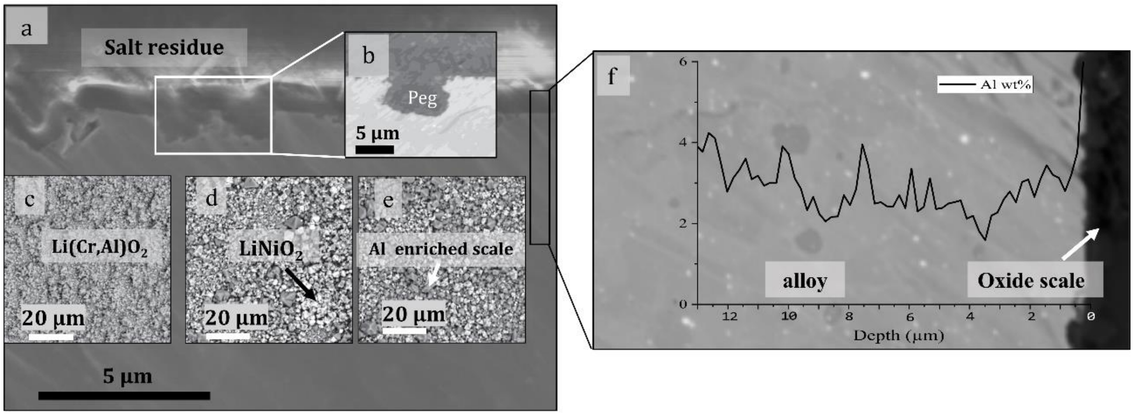

*Figure 5.17 Nikrothal® PM58 exposed to alkali carbonate melt at 800ºC. Cross-section after **a**)1000 h, visualised with SEM contrast; and **b**) peg formation after 1000 h, visualised with back-scatter contrast. Top-view image after exposure for: **c**) 72 h, with Li(Cr,Al)O_2 covering the surface; **d**) 500 h, showing the presence of nickel- and iron-rich particles; and **e**) 1000 h, showing Al-enriched scale fractions, and **f**) Line-scan for the sub-oxide zone after 1000 h. Reproduced with permission from Elsevier [128].*

6 Conclusions and Outlook

6.1. Comparative study of a FeNiCr vs FeCrAl Alloys in Different Salt Melts

Evaluation of corrosion of the tested alloys showed that both the chromia- and alumina-forming alloys had acceptable resistance to corrosion by Solar Salt at 650 °C compared to the other eutectic salt exposures at higher temperatures. However, the stainless-steel alloy 316H showed gradual growth of the oxide scale and penetration of nitrogen into the alloy, forming chromium nitride precipitates, and thereby lowering the chromium activity in the alloy. Kanthal® APMT developed a thin protective $NaAlO_2$scale. Despite the absence of an internal attack underneath the $NaAlO_2$-scale, the alloy is considered to be susceptible to nitridation.

The poorest corrosion behaviour among all the alloys tested in the three melts was observed for the stainless steel alloy 304L exposed to the alkali carbonate melt at 800°C. The chromia-forming 304L alloy suffered severe carburisation, whereby chromium carbide precipitates reached several hundreds of micrometres into the alloy, altering the chemistry and mechanical properties of the alloy. In strong contrast, Kanthal® APMT developed a protective α-$LiAlO_2$ scale, and no internal carburisation was detected for at least 1000 h. Interestingly, a phase transition from α-$LiAlO_2$ to γ-$LiAlO_2$ oxide scale was observed after 168 h of exposure to alkali carbonate melt.

Relatively fast material degradation was detected after exposure to the eutectic chloride melt together with mass loss. Both 304L and Kanthal® APMT alloys suffered mass loss due to leaching of elements into the melt, resulting in cavities in the alloy microstructure that were filled with melt components. After 168 h, Kanthal® APMT formed a magnesium aluminate scale on the alloy surface, preventing leaching of metals into the melt. Nonetheless, after 500 h, the magnesium aluminate was degraded. Furthermore, Al has been selectively leached from the Kanthal APMT. On the other hand, chromium has been leached selectively from 304L. In the bulk of Kanthal® APMT, cavities formed due to the leaching of metals. Those cavities were filled with magnesium oxide and chloride, surrounded by a $(Fe_{0.75}Cr_{0.25})_2Mo$ Laves phase. This indicates that molybdenum was leached much slower than chromium and aluminium. Laves-phase rims, rich in molybdenum and chromium, appeared to protect Kanthal® APMT against rapid chromium leaching compared to alloy 304L. This may explain the overall lower mass loss measured for Kanthal® APMT.

In summary, and considering the potential risks, the alkali nitrate melt seems to be the best option so far; even though the nitrogen internally attacks the chromia-forming alloy, it is acceptably slow and predictable.

6.2. Comparative Study of Five Alumina-Forming Alloys in Alkali Carbonate Melt

Five alumina-forming alloys were investigated in contact with carbonate melt at 800°C for up to 1000 h under CO_2. Based on their corrosion behaviour, the alloys were differentiated as exhibiting "normal" or "deviating" α-$LiAlO_2$ formation and transformation. A "normal" α-$LiAlO_2$ formation behaviour refers to the absence of additional cations in the process, e.g., Fe or Cr ions. On the other hand, does a "deviating" α-$LiAlO_2$ behaviour summarise all other possibilities of formation, when, e.g., initially a transient alkali oxide formation or pegging occurs incorporating ternary cationic species, such as iron and chromium ions.

The "normal" α-$LiAlO_2$-forming alloys had similar corrosion behaviour, exemplified by the formation of a thin, protective α-$LiAlO_2$ scale. The thermodynamically stable γ-$LiAlO_2$ nucleated on top of the α-$LiAlO_2$ scale forming large, non-protective crystals. Detrimental aluminium depletion from the alloys was not detected for at least 1000 h, until the experiment ended.

The investigated Kanthal® EF100 and Nikrothal® PM58 were classified as "deviating" $LiAlO_2$ scale evolution alloys. However, Kanthal® EF100 exhibited only an initial "deviating" behaviour by forming an external lithium ferrite after 72 h at 800°C. Upon longer exposure, it followed the "normal" $\alpha \rightarrow \gamma$-$LiAlO_2$ transformation process. Lastly, and due to the austenitic structure of Nikrothal® PM58, aluminium diffusion from the alloy towards the alloy/melt interface was relatively slow, and the alloy did not grow the desirable α-$LiAlO_2$ scale at 800°C.

6.3. Outlook

In this work, the corrosion assessment of the tested alloys depended only on the bare alloy behaviour when exposed to certain conditions without applying any corrosion mitigation methods. In future work, corrosion mitigation strategies will be adopted, such as pre-oxidation of the samples.

Longer exposures will be conducted on the alumina forming alloys to evaluate better their corrosion resistance, in addition to studying the effect of pre-oxidation of samples.

Chemical analysis for the salts residues that have been collected after exposures will be conducted using inductively coupled plasma optical emission spectroscopy (ICP-OES).

References

1. Masson-Delmotte, V., et al., *IPCC, 2021: Summary for Policymakers. In: Climate Change 2021: The Physical Science Basis. Contribution of Working Group I to the Sixth Assessment Report of the Intergovernmental Panel on Climate Change*. 2021. p. 4-36.
2. unfccc.int. *The Paris Agreement*. 2015 [cited 2021 07-09]; Available from: https://unfccc.int/process-and-meetings/the-paris-agreement/the-paris-agreement.
3. Achkari, O. and A. El Fadar, *Latest developments on TES and CSP technologies – Energy and environmental issues, applications and research trends.* Applied Thermal Engineering, 2020. **167**: p. 114806.
4. Lovegrove, K. and J. Pye, *Fundamental principles of concentrating solar power (CSP) systems*, in *Concentrating Solar Power Technology*. 2012, © Woodhead Publishing Limited. p. 16-67.
5. Alva, G., et al., *Thermal energy storage materials and systems for solar energy applications.* Renewable and Sustainable Energy Reviews, 2017. **68**: p. 693-706.
6. Köberle, A.C., D.E.H.J. Gernaat, and D.P. van Vuuren, *Assessing current and future techno-economic potential of concentrated solar power and photovoltaic electricity generation.* Energy, 2015. **89**: p. 739-756.
7. Zhao, Y., P. Li, and H. Jin, *Heat Transfer Performance Comparisons of Supercritical Carbon Dioxide and NaCl–KCl–ZnCl2 Eutectic Salts for Solar s-CO2 Brayton Cycle.* Energy Procedia, 2017. **142**: p. 680-687.
8. Hoeven, M., *IEA Technology Roadmaps for Solar Electricity*. International Energy Agency, 2014.
9. Ellingham, J.T., *Transactions and Communications.* Journal of the Society of Chemical Industry, 1944. **63**(5): p. 125-160.
10. Yin, J.M., et al., *Review of supercritical CO2 power cycles integrated with CSP.* International Journal of Energy Research, 2019. **44**(3): p. 1337-1369.
11. Ho, C.K., et al., *Technoeconomic Analysis of Alternative Solarized s-CO2 Brayton Cycle Configurations.* Journal of Solar Energy Engineering, 2016. **138**(5).
12. Walczak, M., et al., *Materials corrosion for thermal energy storage systems in concentrated solar power plants.* Renewable and Sustainable Energy Reviews, 2018. **86**: p. 22-44.
13. Sarvghad, M., T.A. Steinberg, and G. Will, *Corrosion of stainless steel 316 in eutectic molten salts for thermal energy storage*, in *Solar Energy*. 2018. p. 198-203.
14. Mehos, M., et al., *Concentrating Solar Power Gen3 Demonstration Roadmap.* Nrel/Tp-5500-67464, 2017: p. 1-140.
15. *Concentrating Solar Power*. 2010: International Energy Agency
16. Palacios, A., et al., *Thermal energy storage technologies for concentrated solar power – A review from a materials perspective.* Renewable Energy, 2020. **156**: p. 1244-1265.
17. *US Department of Energy Report: The Year of Concentrating Solar Power*. 2014.
18. Sarvghad, M., et al., *Materials compatibility for the next generation of Concentrated Solar Power plants*, in *Energy Storage Materials*. 2018. p. 179-198.
19. Khare, S., et al., *Selection of materials for high temperature sensible energy storage.* Solar Energy Materials and Solar Cells, 2013. **115**: p. 114-122.
20. Gasia, J., L. Miró, and L.F. Cabeza, *Review on system and materials requirements for high temperature thermal energy storage. Part 1: General requirements.* Renewable and Sustainable Energy Reviews, 2017. **75**: p. 1320-1338.
21. Campbell, F.C., *Phase Diagrams - Understanding the Basics*. 2012, ASM International.
22. Zhang, X., et al., *Thermodynamic evaluation of phase equilibria in NaNO3-KNO3 system.* Journal of Phase Equilibria, 2003. **24**(5): p. 441-446.
23. Baker, B.A., *1.16 - Types of Environments*, in *Shreir's Corrosion*, B. Cottis, et al., Editors. 2010, Elsevier: Oxford. p. 399-406.

24. Chevalier, S., *1.07 - Mechanisms and Kinetics of Oxidation*, in *Shreir's Corrosion*, B. Cottis, et al., Editors. 2010, Elsevier: Oxford. p. 132-152.
25. Wagner, C., *Beitrag zur theorie des anlaufvorgangs.* Zeitschrift für physikalische Chemie, 1933. **21**(1): p. 25-41.
26. Khanna, A.S., *Chapter 6 - High-Temperature Oxidation*, in *Handbook of Environmental Degradation of Materials (Third Edition)*, M. Kutz, Editor. 2018, William Andrew Publishing. p. 117-132.
27. Gomez-Vidal, J.C., et al., *Corrosion resistance of alumina-forming alloys against molten chlorides for energy production. I: Pre-oxidation treatment and isothermal corrosion tests*, in *Solar Energy Materials and Solar Cells*. 2017. p. 222-233.
28. Gomez-Vidal, J.C., et al., *Corrosion resistance of alumina forming alloys against molten chlorides for energy production. II: Electrochemical impedance spectroscopy under thermal cycling conditions*, in *Solar Energy Materials and Solar Cells*. 2017, Elsevier B.V. p. 234-245.
29. Abu Kassim, S., et al., *High temperature corrosion of Hastelloy C22 in molten alkali salts: The effect of pre-oxidation treatment.* Corrosion Science, 2020. **173**: p. 108761.
30. Ding, W., A. Bonk, and T. Bauer, *Molten chloride salts for next generation CSP plants: Selection of promising chloride salts & study on corrosion of alloys in molten chloride salts.* AIP Conference Proceedings, 2019. **2126**(1): p. 200014.
31. Young, D.J., *Chapter 1 - The Nature of High Temperature Oxidation*, in *High Temperature Oxidation and Corrosion of Metals (Second Edition)*, D.J. Young, Editor. 2016, Elsevier. p. 1-30.
32. Geers, C. and I. Panas, *Impact of Grain Boundary Density on Oxide Scaling Revisited.* Oxidation of Metals, 2019. **91**(1): p. 55-75.
33. Young, D.J., *Corrosion in Complex Environments*, in *High Temperature Oxidation and Corrosion of Metals*. 2016. p. 603-645.
34. Hsu, H., J.H. Devan, and M. Howell, *Solubilities of LiFeO2 and (Li , K) 2CrO4 in Molten Alkali Carbonates at 650°C.* Journal of The Electrochemical Society, 1987. **134**: p. 2146-2150.
35. Indacochea, J., et al., *Corrosion performance of ferrous and refractory metals in molten salts under reducing conditions.* Journal of Materials Research, 1999. **14**(5): p. 1990-1995.
36. Lee, H.-Y. and K.-H. Baik, *Comparison of corrosion resistance between Al2O3 and YSZ coatings against high temperature LiCl-Li2O molten salt.* Metals and Materials International, 2009. **15**(5): p. 783.
37. Engelberg, D.L., *2.06 - Intergranular Corrosion*, in *Shreir's Corrosion*, B. Cottis, et al., Editors. 2010, Elsevier: Oxford. p. 810-827.
38. Sridharan, K. and T.R. Allen, *Corrosion in Molten Salts*, in *Molten Salts Chemistry*. 2013, Elsevier Inc. p. 241-267.
39. Bell, S., T. Steinberg, and G. Will, *Corrosion mechanisms in molten salt thermal energy storage for concentrating solar power*, in *Renewable and Sustainable Energy Reviews*. 2019, Elsevier Ltd. p. 109328.
40. Ravi Shankar, A., et al., *Corrosion and Microstructure Correlation in Molten LiCl-KCl Medium.* Metallurgical and Materials Transactions A, 2010. **41**(7): p. 1815-1825.
41. Hofmeister, M., et al., *Corrosion behaviour of stainless steels and a single crystal superalloy in a ternary LiCl–KCl–CsCl molten salt.* Corrosion Science, 2015. **90**: p. 46-53.
42. Gomez-Vidal, J.C. and R. Tirawat, *Corrosion of alloys in a chloride molten salt (NaCl-LiCl) for solar thermal technologies.* Solar Energy Materials and Solar Cells, 2016. **157**: p. 234-244.
43. Fernández, A.G., et al., *Corrosion evaluation of alumina-forming alloys in carbonate molten salt for CSP plants.* Renewable Energy, 2019. **140**: p. 227-233.
44. Gomez-Vidal, J.C., et al., *Corrosion resistance of alumina forming alloys against molten chlorides for energy production. II: Electrochemical impedance spectroscopy under thermal cycling conditions.* Solar Energy Materials and Solar Cells, 2017. **166**: p. 234-245.

45. Ding, W., et al., *Hot corrosion behavior of commercial alloys in thermal energy storage material of molten MgCl2/KCl/NaCl under inert atmosphere*, in *Solar Energy Materials and Solar Cells*. 2018, Elsevier B.V. p. 22-30.
46. Vidal, J.C. and N. Klammer, *Molten chloride technology pathway to meet the U.S. DOE sunshot initiative with Gen3 CSP*, in *AIP Conference Proceedings*. 2019.
47. Zhao, Y. and J. Vidal, *Potential scalability of a cost-effective purification method for MgCl2-Containing salts for next-generation concentrating solar power technologies.* Solar Energy Materials and Solar Cells, 2020. **215**.
48. Kipouros, G.J. and D.R. Sadoway, *A thermochemical analysis of the production of anhydrous MgCl2.* Journal of Light Metals, 2001. **1**(2): p. 111-117.
49. Ding, W. and T. Bauer, *Progress in Research and Development of Molten Chloride Salt Technology for Next Generation Concentrated Solar Power Plants.* Engineering, 2021. **7**(3): p. 334-347.
50. Picard, G.S., T.A. Flament, and B.L. Trémillon, *Acidity and Thermochemical Stability of Molten Sodium Nitrate and Nitrite Mixtures.* Journal of The Electrochemical Society, 1985. **132**(4): p. 863-868.
51. Picard, G.S., H.M. Lefebvre, and B.L. Trémillon, *Thermodynamic Study of Corrosion of Iron in NaNO3 - NaNO2 Mixtures.* Journal of The Electrochemical Society, 1987. **134**(1): p. 52-58.
52. S.H. Goods, R.W.B., M. R. Prairie, J. M. Chavez, *Corrosion of Stainless and Carbon Steels in Molten Mixtures of Industrial Nitrates*. 1994: Sandia National Laboratorie.
53. Goods, S.H. and R.W. Bradshaw, *Corrosion of Stainless Steels and Carbon Steel by Molten Mixtures of Commercial Nitrate Salts.* Journal of Materials Engineering and Performance, 2004. **13**(1): p. 78-87.
54. Bradshaw, R.W. and W.M. Clift, *Effect of chloride content of molten nitrate salt on corrosion of A516 carbon steel*. 2010, Sandia National Laboratories: Albuquerque, New Mexico 87185 and Livermore, California 94550. p. 1–27.
55. Liu, M., et al., *Review on concentrating solar power plants and new developments in high temperature thermal energy storage technologies*, in *Renewable and Sustainable Energy Reviews*. 2016, Elsevier. p. 1411-1432.
56. Grosu, Y., O. Bondarchuk, and A. Faik, *The effect of humidity, impurities and initial state on the corrosion of carbon and stainless steels in molten HitecXL salt for CSP application.* Solar Energy Materials and Solar Cells, 2018. **174**: p. 34-41.
57. Li, H., et al., *Effect of Chloride Impurity on Corrosion Kinetics of Stainless Steels in Molten Solar Salt for CSP Application: Experiments and Modeling.* Oxidation of Metals, 2021. **95**(3): p. 311-332.
58. Cheng, W.-J., D.-J. Chen, and C.-J. Wang, *High-temperature corrosion of Cr–Mo steel in molten LiNO3–NaNO3–KNO3 eutectic salt for thermal energy storage.* Solar Energy Materials and Solar Cells, 2015. **132**: p. 563-569.
59. Goods, S.H., et al., *Corrosion of stainless and carbon steels in molten mixtures of industrial nitrates*. 1994, ; Sandia National Lab. (SNL-CA), Livermore, CA (United States). p. 37 p.
60. Bradshaw, R.W. and S.H. Goods, *Corrosion of Alloys and Metals by Molten Nitrates*. 2001, Sandia National Laboratories.
61. Bradshaw, R.W. and S.H. Goods, *Corrosion resistance of stainless steels during thermal cycling in alkali nitrate molten salts*. 2001, ; Sandia National Laboratories (SNL), Albuquerque, NM, and Livermore, CA (United States). p. Medium: ED; Size: 39 p.
62. Fernández, A.G., et al., *Corrosion of stainless steels and low-Cr steel in molten Ca(NO3)2–NaNO3–KNO3 eutectic salt for direct energy storage in CSP plants.* Solar Energy Materials and Solar Cells, 2015. **141**: p. 7-13.
63. Fernández, A.G., M.I. Lasanta, and F.J. Pérez, *Molten Salt Corrosion of Stainless Steels and Low-Cr Steel in CSP Plants.* Oxidation of Metals, 2012. **78**(5-6): p. 329-348.

64. Kruizenga, A. and D. Gill, *Corrosion of Iron Stainless Steels in Molten Nitrate Salt.* Energy Procedia, 2014. **49**: p. 878-887.
65. Fernández, A.G., et al., *Corrosion of alumina-forming austenitic steel in molten nitrate salts by gravimetric analysis and impedance spectroscopy*, in *Materials and Corrosion*. 2014. p. 267-275.
66. Yamamoto, Y., et al., *Alloying effects on creep and oxidation resistance of austenitic stainless steel alloys employing intermetallic precipitates.* Intermetallics, 2008. **16**(3): p. 453-462.
67. Meißner, T.M., et al., *Improving the corrosion resistance of ferritic-martensitic steels at 600 °C in molten solar salt via diffusion coatings.* Solar Energy Materials and Solar Cells, 2021. **227**.
68. Mohan, G., M.B. Venkataraman, and J. Coventry, *Sensible energy storage options for concentrating solar power plants operating above 600 °C.* Renewable and Sustainable Energy Reviews, 2019. **107**: p. 319-337.
69. Gleeson, B., *1.09 - Thermodynamics and Theory of External and Internal Oxidation of Alloys*, in *Shreir's Corrosion*, B. Cottis, et al., Editors. 2010, Elsevier: Oxford. p. 180-194.
70. Young, D.J., *Chapter 6 - Alloy Oxidation II: Internal Oxidation*, in *High Temperature Oxidation and Corrosion of Metals (Second Edition)*, D.J. Young, Editor. 2016, Elsevier. p. 261-333.
71. Shores, D.A. and P. Singh. *Department of Chemical Engineering and Materials Science*. in *Proceedings of the Symposium on Molten Carbonate Fuel Cell Technology*. 1984. Electrochemical Society.
72. Yuh, C.-Y., et al., *Status of Carbonate Fuel Cell Materials.* ECS Transactions, 2012. **41**: p. 21-33.
73. Ni, C.S., et al., *Electrochemical impedance studies of the initial-stage corrosion of 310S stainless steel beneath thin film of molten (0.62Li,0.38K)2CO3 at 650°C.* Corrosion Science, 2011. **53**(3): p. 1018-1024.
74. de Miguel, M.T., et al., *Corrosion resistance of HR3C to a carbonate molten salt for energy storage applications in CSP plants.* Solar Energy Materials and Solar Cells, 2016. **157**: p. 966-972.
75. Frangini, S. and S. Loreti, *The role of temperature on the corrosion and passivation of type 310S stainless steel in eutectic (Li + K) carbonate melt*, in *Journal of Power Sources*. 2006. p. 800-804.
76. Gomez-Vidal, J.C., J. Noel, and J. Weber, *Corrosion evaluation of alloys and MCrAlX coatings in molten carbonates for thermal solar applications.* Solar Energy Materials and Solar Cells, 2016. **157**: p. 517-525.
77. Hamdy, E., J.N. Olovsjö, and C. Geers, *Perspectives on selected alloys in contact with eutectic melts for thermal storage: Nitrates, carbonates and chlorides.* Solar Energy, 2021. **224**: p. 1210-1221.
78. Frangini, S., *Corrosion Behavior of AISI 316L Stainless Steel and ODS FeAl Aluminide in Eutectic Li2CO3–K2CO3 Molten Carbonates under Flowing CO2–O2 Gas Mixtures.* Oxidation of Metals, 2000. **53**(1): p. 139-156.
79. Randström, S., C. Lagergren, and P. Capobianco, *Corrosion of anode current collectors in molten carbonate fuel cells.* Journal of Power Sources, 2006. **160**(2): p. 782-788.
80. Zeng, C. and Y. Liu, *A comparative study of the corrosion behavior of three stainless steels in an eutectic (Li, Na, K) 2CO3 melt with and without (Na, K) Cl Additives at 973K in Air.* 2011.
81. Prieto, C., et al., *Carbonate molten salt solar thermal pilot facility: Plant design, commissioning and operation up to 700 °C.* Renewable Energy, 2020. **151**: p. 528-541.
82. Spiegel, M., P. Biedenkopf, and H.-J. Grabke, *Corrosion of iron base alloys and high alloy steels in the Li2CO3-K2CO3 eutectic mixture.* Corrosion Science, 1997. **39**(7): p. 1193-1210.
83. Perez, F., et al., *Hot-corrosion studies of separator plates of AISI-310 stainless steels in molten-carbonate fuel cells.* Oxidation of metals, 2000. **53**(3): p. 375-398.
84. Ahn, S., et al., *Electrochemical analysis on the growth of oxide formed on stainless steels in molten carbonate at 650° C.* international journal of hydrogen energy, 2014. **39**(23): p. 12291-12299.
85. Li, C.-j., et al., *Survey of Properties of Key Single and Mixture Halide Salts for Potential Application as High Temperature Heat Transfer Fluids for Concentrated Solar Thermal Power Systems*. 2014. p. 133-157.

86. Vignarooban, K., et al., *Heat transfer fluids for concentrating solar power systems - A review*, in *Applied Energy*. 2015, Elsevier Ltd. p. 383-396.
87. Ding, W., A. Bonk, and T. Bauer, *Corrosion behavior of metallic alloys in molten chloride salts for thermal energy storage in concentrated solar power plants: A review*, in *Frontiers of Chemical Science and Engineering*. 2018. p. 564-576.
88. Guillot, S., et al., *Corrosion effects between molten salts and thermal storage material for concentrated solar power plants*, in *Applied Energy*. 2012. p. 174-181.
89. Phillips, W., Z. Karmiol, and D. Chidambaram, *Effect of Metallic Li on the Corrosion Behavior of Inconel 625 in Molten LiCl-Li 2 O-Li* in *Journal of The Electrochemical Society*. 2019. p. C162-C168.
90. Wu, Y.-t., et al., *Experimental study on optimized composition of mixed carbonate salt for sensible heat storage in solar thermal power plant.* Solar Energy, 2011. **85**(9): p. 1957-1966.
91. Ding, W., A. Bonk, and T. Bauer, *Molten Chloride Salts for Next Generation CSP Plants : Selection of Promising Chloride Salts & Study on Corrosion of Alloys in Molten Chloride Salts.* 2018.
92. Hamdy, E., J.N. Olovsjö, and C. Geers, *Additional data and experimental setups used for the study on alloys in contact to high temperature eutectic melts for thermal storage* Data in Brief, 2021: p. 107446.
93. Ding, W., et al., *Molten chloride salts for next generation concentrated solar power plants: Mitigation strategies against corrosion of structural materials*, in *Solar Energy Materials and Solar Cells*. 2019, Elsevier B.V. p. 298-313.
94. Fähsing, D., et al., *Corrosion testing of diffusion-coated steel in molten salt for concentrated solar power tower systems*, in *Surface and Coatings Technology*. 2018, Elsevier B.V. p. 46-55.
95. Soleimani Dorcheh, A., R.N. Durham, and M.C. Galetz, *Corrosion behavior of stainless and low-chromium steels and IN625 in molten nitrate salts at 600 °c*, in *Solar Energy Materials and Solar Cells*. 2016, Elsevier. p. 109-116.
96. Gomes, A., et al., *High-temperature corrosion performance of austenitic stainless steels type AISI 316L and AISI 321H, in molten Solar Salt*, in *Solar Energy*. 2019, Elsevier. p. 408-419.
97. Palacios, A., et al., *High-temperature corrosion behaviour of metal alloys in commercial molten salts.* Solar Energy, 2020. **201**: p. 437-452.
98. Encinas-Sánchez, V., et al., *Electrochemical impedance spectroscopy (EIS): An efficient technique for monitoring corrosion processes in molten salt environments in CSP applications.* Solar Energy Materials and Solar Cells, 2019. **191**: p. 157-163.
99. *Standard Practice for Preparing, Cleaning, and Evaluating Corrosion Test Specimens*, in *Methods for Cleaning After Testing*. 2017, © ASTM International.
100. Epp, J., *X-ray diffraction (XRD) techniques for materials characterization*, in *Materials characterization using nondestructive evaluation (NDE) methods*. 2016, Elsevier. p. 81-124.
101. Bragg, W.H.S., *X-rays and crystal structure* ed. L.S. Bragg. 1915, London: G. Bell and Sons, Ltd.
102. Kniess, C.T., et al., *Quantitative Determination of the Crystalline Phases of the Ceramic Materials Utilizing the Rietveld Method.* Materials Science Forum, 2010. **660-661**: p. 164-169.
103. Joseph Goldstein, et al., *Scanning Electron Microscopy and X-ray Microanalysis*. 3 ed. Scanning. Vol. 27. 2005, Boston, MA: Springer. XIX, 689.
104. Sequeira, C.A.C., *Corrosion in Molten Salts*, in *High Temperature Corrosion*. 2019. p. 296-324.
105. Bale, C.W., et al., *FactSage Thermochemical Software and Databases - Recent Developments.* Calphad, 2009. **33**: p. 17.
106. Cruchley, S., H. Evans, and M. Taylor, *An overview of the oxidation of Ni-based superalloys for turbine disc applications: surface condition, applied load and mechanical performance*. Vol. 33. 2016. 1-11.
107. Sah, S.P., E. Tada, and A. Nishikata, *Corrosion behaviour of austenitic stainless steels in carbonate melt at 923 K under controlled CO2-O2 environment*, in *Corrosion Science*. 2018, Elsevier Ltd. p. 310-317.

108. Attia, A.A., S.A. Salih, and A.M. Baraka, *Corrosion and passivation behaviors of some stainless steel alloys in molten alkali carbonates.* Electrochimica Acta, 2002. **48**(2): p. 113-118.
109. Sarvghad, M., T.A. Steinberg, and G. Will, *Corrosion of steel alloys in eutectic NaCl+Na2CO3 at 700 °C and Li2CO3 + K2CO3 + Na2CO3 at 450 °C for thermal energy storage.* Solar Energy Materials and Solar Cells, 2017. **170**: p. 48-59.
110. Spiegel, M., P. Biedenkopf, and H.J. Grabke, *Corrosion of iron base alloys and high alloy steels in the Li2CO3-K2CO3 eutectic mixture.* Corrosion Science, 1997. **39**(7): p. 1193-1210.
111. Evans, H.E., D.A. Hilton, and R.A. Holm, *Internal attack during the oxidation of nitrided stainless steels.* Oxidation of Metals, 1977. **11**(1): p. 1-21.
112. Grosse, M., *9 - High-temperature oxidation in nuclear reactor systems*, in *Nuclear Corrosion Science and Engineering*, D. Féron, Editor. 2012, Woodhead Publishing. p. 265-300.
113. Encinas-Sánchez, V., et al., *Corrosion resistance of Cr/Ni alloy to a molten carbonate salt at various temperatures for the next generation high-temperature CSP plants.* Solar Energy, 2018. **171**: p. 286-292.
114. Danek, V., M. Tarniowy, and L. Suski, *Kinetics of the α → γ phase transformation in LiAlO2 under various atmospheres within the 1073–1173 K temperatures range.* Journal of Materials Science, 2004. **39** p. 2429– 2435.
115. Heo, S.J., et al., *Role of Exposure Atmospheres on Particle Coarsening and Phase Transformation of LiAlO2.* Journal of The Electrochemical Society, 2017. **164**(8): p. H5086-H5092.
116. Bennett, M.J., R. Newton, and J.R. Nicholls, *The behaviour of commercial FeCrAIRE alloys in nitrogen-oxygen - water vapour bioxidant environments.* Materials at High Temperatures, 2003. **20**(3): p. 347-356.
117. Choi, H.J., et al., *Phase and Microstructural Stability of Electrolyte Matrix Materials for Molten Carbonate Fuel Cells.* Fuel Cells, 2010. **10**(4): p. 613-618.
118. Ding, W.J., et al., *Molten chloride salts for next generation CSP plants: Electrolytical salt purification for reducing corrosive impurity level.* Solar Energy Materials and Solar Cells, 2019. **199**: p. 8-15.
119. Tian, Y. and C.Y. Zhao, *A review of solar collectors and thermal energy storage in solar thermal applications.* Applied Energy, 2013. **104**: p. 538-553.
120. Ge, Z., Y. Huang, and Y. Ding, *Eutectic composition-dependence of latent heat of binary carbonates (Na2CO3/Li2CO3).* Solar Energy Materials and Solar Cells, 2018. **179**: p. 202-206.
121. Copson, H.R., *Corrosion of Heating Electrodes in Molten Chloride Baths.* Journal of The Electrochemical Society, 1953. **100**(6): p. 257.
122. Evans, H.E., D.J. Norfolk, and T. Swan, *Perturbation of parabolic kinetics resulting from the accumulation of stress in protective oxide layers.* Journal of the Electrochemical Society, 1978. **125**(7): p. 1180-1185.
123. Bouvier, P., et al., *High-pressure structural evolution of undoped tetragonal nanocrystalline zirconia.* Physical Review B, 2000. **62**(13): p. 8731-8737.
124. Harlow, W., et al., *Thickness-dependent stabilization of tetragonal ZrO2 in oxidized zirconium.* Scripta Materialia, 2018: p. 95-98.
125. Spengler, D.J., et al., *Characterization of Zircaloy-4 corrosion films using microbeam synchrotron radiation.* Journal of Nuclear Materials, 2015. **464**(C): p. 107-118.
126. Lejus, A.-M., *Sur la formation à haute température de spinelles non stoechiométriques et de phases dérivées dans plusieurs systèmes d'oxydes à base d'alumine et dans le système alumine-nitrure d'aluminium*. 1964, Masson et Cie: Paris.
127. Momma, K. and F. Izumi, *VESTA 3 for three-dimensional visualization of crystal, volumetric and morphology data.* Journal of Applied Crystallography, 2011. **44**(6): p. 1272-1276.
128. Hamdy, E., et al., *Differentiation in corrosion performance of alumina forming alloys in alkali carbonate melts.* Corrosion Science, 2021: p. 109857.

129. Lehmann, H.-A. and H. Hesselbarth, *Zur Kenntnis der Lithiumaluminate. I. Über eine neue Modifikation des LiAlO2.* Zeitschrift für anorganische und allgemeine Chemie, 1961. **313**(1-2): p. 117-120.
130. Ribeiro, R., G. Silva, and N. Mohallem, *The influences of heat treatment on the structural properties of lithium aluminates.* Journal of Physics and Chemistry of Solids, 2001. **62**(5): p. 857-864.
131. Landberg, E., et al., *New alumina-forming steels for future energy production with focus on solar power*. 2016: Jernkontoret, Stockholm.
132. Asokan, V., et al., *The influence of Si on the primary protection of lean FeCrAl model alloys in O2 and O2+H2O at 600 °C—A microstructural investigation.* Corrosion Science, 2021. **179**: p. 109155.
133. Young, D.J., *Chapter 5 - Oxidation of Alloys I: Single Phase Scales*, in *High Temperature Oxidation and Corrosion of Metals (Second Edition)*, D.J. Young, Editor. 2016, Elsevier. p. 193-260.

Paper I (a)

Perspectives on selected alloys in contact with eutectic melts for thermal storage: Nitrates, carbonates and chlorides

E. Hamdy, J. N. Olovsjö, and C. Geers

Bibliography

E. Hamdy, J. N. Olovsjö, and C. Geers, "Perspectives on selected alloys in contact with eutectic melts for thermal storage: Nitrates, carbonates and chlorides" *Solar Energy*, vol. 224, pp. 1210-1221, 2021, doi: https://doi.org/10.1016/j.solener.2021.06.069.

Solar Energy 224 (2021) 1210–1221

Contents lists available at ScienceDirect

Solar Energy

journal homepage: www.elsevier.com/locate/solener

Perspectives on selected alloys in contact with eutectic melts for thermal storage: Nitrates, carbonates and chlorides

Esraa Hamdy [a,*], Johanna Nockert Olovsjö [b], Christine Geers [a]

[a] Energy and Materials, Chalmers University of Technology, Gothenburg, Sweden
[b] Kanthal AB, Hallstahammar, Sweden

ARTICLE INFO

Keywords:
Thermal storage
High temperature corrosion
Carbonates
Molten chlorides
Carburization
Laves phase

ABSTRACT

Increasing the operating temperature of molten salt-based concentrated solar power plants is of paramount importance to enable next-generation gas turbines and an overall increase in power conversion efficiency. The issue is how to mitigate the degradation of necessary metallic components in highly corrosive salt environments. In this study, three eutectic salt mixture candidates, nitrates, carbonates, and chlorides, are brought into contact with stainless steel (316H or 304L) and the FeCrAl alloy Kanthal® APMT. The post-exposure analysis is discussed in terms of the overall performance of each alloy as concerns mass change, scale growth, internal attack, and leaching. Significant reduction of corrosion is realised through the ability of Kanthal® APMT to form aluminium oxide species at the surface in contact with alkali nitrates and carbonates. On the other hand, aluminium is leached most efficiently in contact with chlorides, which causes a deeper attack on Kanthal® APMT than alloy 304L.

The overall conclusion is that only by employing a holistic perspective on all individual measurements can a long-term performance estimation be formulated.

1. Introduction

Concentrated solar power (CSP) is an appealing energy source utilising the most abundant energy source, the sun (Caitlin et al., 2019). CSP has evolved into a mature technology over the last decade and contributes to the fossil-free electricity production blend used in many countries. Low-cost thermal energy storage (TES), in other applications also referred to as heat transfer fluid (HTF), offers an extension for electrical power supply beyond sunset in CSP plants (Sarvghad et al., 2018a; Walczak et al., 2018; Mehos et al., 2017). To enable greater efficiency in energy conversion for the next generation of CSP technology, it is necessary to overcome the current temperature limit of 560 °C (Steinmann, 2015), which is the decomposition temperature of the currently used eutectic salt mixture of alkali nitrates, 'Solar Salt', which comprises sodium and potassium nitrates. Redesigning CSP plants for the Brayton cycle technology and utilising supercritical carbon dioxide instead of steam for the gas turbines, requires a minimum operating temperature of 750 °C for the TES (IEA, 2010; Zhao et al., 2017; Ellingham, 1944; Yin et al., 2019; Ho et al., 2016). Increasing the temperature of salt melts also increases their corrosivity towards metallic materials. Significant improvement in the compatibility of container material (tanks/pipes/heat exchangers) and the TES medium is therefore necessary (Sarvghad et al., 2018b; Mehos et al., 2017).

Considerable efforts have been dedicated to characterising the thermophysical properties of different types of TES media (Sarvghad et al., 2018a). While Solar Salt is already widely used, alkali carbonates or chlorides have been identified as TES candidates for the next generation CSP. However, each of these candidates differs in abundance, thermal stability, liquidus range, price, and corrosivity (Sarvghad et al., 2018a; Walczak et al., 2018; Mehos et al., 2017). Corrosivity is an apparent obstacle to enabling the first Brayton cycle operated CSP (Mehos et al., 2017). The corrosion of the materials in contact with the storage medium can lead to a catastrophic failure of an entire CSP plant due to material loss or embrittlement.

Typical high-temperature corrosion phenomena that have been reported in TES tanks are localised corrosion and mechanically assisted corrosion (Walczak et al., 2018). The most common alloys and some recently considered grades of carbon steel, stainless steel, and nickel-based alloys have been evaluated using gravimetric, metallographic, and electrochemical techniques (Goods et al., 1994). Carbon and low-alloy steels were among the first candidates considered for TES components that come in contact with molten salts. In the 1990s, Sandia

---

* Corresponding author.

https://doi.org/10.1016/j.solener.2021.06.069
Received 28 October 2020; Received in revised form 30 May 2021; Accepted 24 June 2021

National Laboratories published a report about the corrosion performance of the low-carbon steel A36, a common type of steel used in construction that come in contact with commercial Solar Salt in current CSP plants (Goods and Bradshaw, 2004). It was found that A36 was covered with a thin adherent oxide scale composed primarily of magnetite at 316 °C and over 7000 h of operation. It was concluded that the impurities found in the commercially available alkali nitrates had no significant effect on the corrosion behaviour of the alloy (Goods and Bradshaw, 2004). However, sensitivity to chloride impurities in the nitrate melt has been found with the low-alloy steel A516 gr. 70. Instead of a protective magnetite layer, a thick hematite scale forms on A516 and spalls frequently, causing rapid metal thickness loss and even local pitting attack (Goods et al., 1994; Bradshaw and Clift, 2010; Liu et al., 2016). The distinction between corrosion testing under static and flow conditions should also be emphasised. Tests in flowing TES media can easily increase corrosion rates by a factor of two (Goods et al., 1994; Bradshaw and Clift, 2010; Liu et al., 2016).

Alloy T22, which is another low-alloy steel, has been selected for use in CSP plants after showing good corrosion behaviour at 390 °C in Solar Salt. However, at 550 °C and after 800 h, the alloy was reported to exhibit 'catastrophic' behaviour due to a severe intergranular attack (Goods et al., 1994). Generally, carbon or low-alloy steels, e.g., alloy A516 gr. 70 or T22, respectively, are recommended for moderate- and low-temperature service, considering the temperature range and impurities in Solar Salt (Goods et al., 1994). Grosu, Y. et *al.* investigated humidity and impurities effects on corrosion behaviour of three alloys, carbon steel A516.Gr70 and stainless steels 304 and 316, in contact with molten HitecXL salt. A516.Gr70 alloy suffered most from humidity, while 304 and 316 alloys showed good corrosion resistance under humid conditions. Despite the very low concentrations of impurities, e.g., Mg, Zn, and Cu in HitecXL salt, it has been reported that the impurities might lower the corrosion resistance of the studied alloys (Grosu et al., 2018). Li, H. *et al.* have also studied the effect of chloride impurity on the corrosion performance of stainless steels 304 and 316L exposed to Solar Salt. Results have shown that the more the chloride content, the lower the corrosion resistance and adherence of the oxide layer for both alloys. Also, stainless steel 316L has shown better corrosion resistance than 304 alloy (Li et al., 2021).

Stepwise enhancing the chromium content, Cheng et al. reported that the corrosion resistance of steel exposed to molten $LiNO_3$–$NaNO_3$–KNO_3 at 550 °C up to 1000 h under nitrogen could be drastically improved by the addition of chromium (9 wt%) (Cheng et al., 2015). An outer $LiFeO_2$ and inner $(Fe,Cr)_3O_4$ scale have been identified (Cheng et al., 2015).

Stainless steels have been tested for higher temperatures and reliability. Most published studies describe the corrosion of stainless steels in contact with Solar Salt. It has generally been concluded that: i) the corrosion resistance of stainless steel alloys is better than that of carbon steels; and ii) corrosion increases with an increase in temperature and exposure time (Goods et al., 1994).

The main corrosion products found on stainless steels in contact with Solar Salt are $FeCrO_4$, Fe_2O_3, and a less dense and less protective outer scale of $NaFeO_2$. Of these products, the formation of Fe-Cr spinels at the alloy-oxide interface renders the rate-limiting step of the corrosion process (Walczak et al., 2018; Bradshaw and Goods, 2001; Fernández et al., 2015b). It has generally been reported that corrosion resistance increases with increasing chromium content in stainless-steel alloys (Fernández et al., 2012; Kruizenga and Gill, 2014); however, it is still inconclusive how the actual amount of chromium affects the composition of an oxide layer. Furthermore, other factors must be considered, such as the nickel and molybdenum content in the alloy chemical composition. However, the addition of molybdenum to alloys exposed to Solar Salt has not shown any effect on the corrosion of stainless-steel grades AISI 316/316L, 317L, and OC-4 with respect to Mo-free alloys (Fernández et al., 2014; Sarvghad et al., 2018a). This paper presents our findings for molybdenum effect on high-temperature corrosion caused by molten chlorides.

Another alloying element that has been found to improve corrosion resistance of alloys in chlorides melt by forming a protective oxide scale is aluminium. Fernandez et al., have conducted a comparative study of alumina-forming, chromia-forming stainless steels, and a low-Cr steel alloy. OC-4, which is an alumina-forming austenitic (AFA) alloy, showed better corrosion resistance in Solar Salt at 390 °C than the 304 stainless steel and T22 steel (Fernández et al., 2014). Also, the relatively high amount of Nb and Ni in OC-4 might have improved the stability of the oxide scale, which led to better corrosion resistance (Yamamoto et al., 2008). Meißner, T. et al. have studied corrosion mitigation by employing three different coatings, a pure Ni, a Cr and a combined Ni and Cr coating, on ferritic-martensitic X20CrMoV12-1 steel. The coated samples has been immersed in molten Solar Salt and tested isothermally at 600 °C for up to 1000 h. Results have revealed that the combined Ni and Cr coating has significantly improved the corrosion resistance of the investigated alloy (Meißner et al., 2021).

Eutectic carbonate and chloride salts have been selected as feasible candidates for higher TES operating temperatures. The corrosion performance of different alloys in contact with those salts has been investigated. Chromia-forming alloys, such as AISI 310 and HR3C, have been tested in Li_2CO_3–K_2CO_3 at 650 °C (Ni et al., 2011) and Li_2CO_3–Na_2CO_3–K_2CO_3 at 700 °C, respectively (de Miguel et al., 2016). These temperatures are still rather low. Results have shown degradation of the protective oxide, which can be explained by the lithiation process. This process has been described as the 'successive formation of different oxides and lithiated phases' (Selman, 1999). In this process, internal stresses may develop leading to crack formation that could contribute to mixed potential several oxidation and lithiation reactions (Tzvetkoff and Kolchakov, 2004). The corrosion behaviour of alloy 310 in a molten carbonate fuel cell (MCFC) has been studied at temperatures <600 °C and >675 °C, and no passive behaviour caused by the formation of porous $LiFe_5O_8$ has been reported (Frangini and Loreti, 2006). The main corrosion products detected during the performance of alloy HR3C exposed to Li_2CO_3–Na_2CO_3–K_2CO_3 for 2000 h, were $LiFeO_2$, $LiCrO_2$, NiO, and $FeCr_2O_4$. These produced a chromium-rich layer at the metal/oxide interface. Degradation was found to be enhanced by the formation of soluble chromates, such as K_2CrO_4 , in early stage of the exposure (de Miguel et al., 2016). These soluble chromates successively leach chromium from the passive scale and the alloy.

Gomez-Vidal et al., have also reported unacceptably high corrosion rates for the stainless steels 310, 321, and 347 exposed to K_2CO_3-Na_2CO_3 at 750 °C (Gomez-Vidal et al., 2016). The overall conclusions of previous studies on chromia-forming stainless steel alloys in carbonate salts have underlined the need to consider alternative alloys or coatings that can be implemented in the next generation of CSP plants. Another study conducted by Fernandez et al. aimed at evaluating the corrosion of AFA alloys; in the study, OC-4 and HR224 grades were exposed to Li_2CO_3–Na_2CO_3–K_2CO_3 at 650 °C for 1000 h (Fernández et al., 2019). Both alloys showed significantly better resistance to the corrosion attack of the salts than chromia-forming alloys (Fernández et al., 2019; Goods et al., 1994). This promising performance was attributed to the multilayer scale structure formed; two layers were identified on OC-4 composed of NiO, alumina (Al_2O_3), and hematite (Fe_2O_3). The oxidation process reached steady state through external oxidation. Alloy HR224, however, showed a more complex structure with three layers composed of NiO and two spinels ($NiFe_2O_4$ and $CrFe_2O_4$) that underwent external oxidation during the isothermal test (Fernández et al., 2019). In a recent study, Prieto et al. designed and built an experimental pilot plant for CSP that operates at a temperature higher than 650 °C; molten carbonates were used as the HTF in this pilot. In This pilot plant investigated other parameters, aspects, and materials compatibility, along with evaluating the corrosion performance of different alloys. Results showed that stainless steel 347 had the poorest corrosion resistance, while Kanthal showed sufficient stability (Prieto et al., 2020).

Eutectic chloride melts pose another potential group of candidates for the TES medium due to their superior thermal stability. However, chlorides are highly corrosive at high temperature. The stainless steel AISI 316L has shown poor corrosion resistance, with rapid formation and spallation of corrosion products, when exposed to LiCl–KCl (Ravi Shankar et al., 2010). Comparative tests on a low-carbon stainless steel (X2CrNi18–9) and a titanium-stabilised high-carbon stainless steel (X6CrNiTi18–10) in LiCl–KCl–CsCl melt in the range of 400–600 °C for up to 27 h have been conducted. It has been revealed that low carbon steel suffered from faster intergranular attack than high carbon steel 'Chlorination–oxidation' is the term used to describe this behaviour by emphasising the role of oxygen. Unlike stainless steel alloys, a Ni-based superalloy (CMSX-4) has been tested at 800 °C for 3 h and showed almost no signs of corrosion (Hofmeister et al., 2015).

Gomez-Vidal and Tirawat have also studied the corrosion behaviour of the alloys AISI 310 and 347 in NaCl–LiCl at 650 °C and 700 °C. Alloy AISI 310 showed relatively good performance, almost as good as In800H at 650 °C for 800 h, unlike alloy 347. The authors explained this the difference in corrosion performance with the alloys' respective nickel content (Gomez-Vidal and Tirawat, 2016).

High operating temperature TES media are very aggressive to common chromia-forming alloys. Recent studies have tested different alumina-forming (Fe-based or Ni-based) alloys (Fernández et al., 2019; Gomez-Vidal et al., 2017a). Industries processing aggressive chemicals at high-temperatures employed Ni-based alloys instead of stainless steels because of their superior resistance to pitting corrosion and crevice attack. Gomez-Vidal et al., have investigated corrosion mitigation by surface passivation of alumina-forming austenitic (AFA) and ferritic alloys (AFF) (Inconel 702, Haynes 224 and Kanthal® APMT) (Gomez-Vidal et al., 2017a).

The AFA alloys showed promising performance against corrosion attack by $MgCl_2$–KCl in oxygen-containing atmospheres for at least 185 h. The pre-oxidised In702 covered with a relatively thick alumina scale has shown best performance (Gomez-Vidal et al., 2017b).

Ding, W. and Bauer, T. have reviewed and summarised recent developments in an attempt to utilise molten chlorides as HTF/TES and the inherent corrosion challenges faced by metallic components in contact with these salts. Some leading suggestions have been reported, e.g., i) salt purification in conjunction with corrosion mitigation methods; ii) the identification of new materials that can withstand such harsh environments (Ding and Bauer, 2021).

In the present study, performance results and requirements for different eutectic melts at intermediate and high operation temperatures were carefully compared. The corrosion behaviour of alumina-forming Kanthal APMT and chromia-forming 304L and 316H was evaluated in alkali nitrates, carbonates, and chlorides. The carbonate and chloride salt mixtures were selected for their potential use in next generation CSP plants, whereas the nitrate mixture, Solar Salt, is currently used in CSPs and thus acts as a reference environment (Walczak et al., 2018; Mehos et al., 2017). The alloys were challenged at temperatures ~100 °C higher than the operating temperatures of the respective melts for 168 h, 500 h, and 1000 h. Here, the aim is to determine the limiting conditions for conventional alloys facing catastrophic corrosion, pitting, and internal attack causing embrittlement.

2. Experiments

We compared the corrosion results of a stainless steel, 304L or 316H, and one distinct AFF, Kanthal APMT, in three different eutectic melts. Melts were selected based on their potential use in commercial CSP plants. The three melts used were: a mixture of alkali nitrates known as Solar Salt (60 wt% $NaNO_3$- 40 wt% KNO_3), carbonates (32.1 wt% Li_2CO_3 -33.4 wt% Na_2CO_3- 34.5 wt% K_2CO_3), and chlorides (64.41 wt% KCl-35.59% wt% $MgCl_2$). The thermophysical properties of the melts can be found in other studies (Gomez-Vidal et al., 2017b; Li et al., 2014; Vignarooban et al., 2015; Ding et al., 2018a).

2.1. *Salt preparation*

Eutectic mixtures were produced from the following salts: $NaNO_3$ (Alfa Aesar 99.0%), KNO_3 (Alfa Aesar 99.0%), Li_2CO_3 (VWR chemicals 99.0%), Na_2CO_3 (EMSURE anhydrous, 99.9%), K_2CO_3 (ThermoFisher Scientific 99.8%), KCl (Alfa Aesar 99.0%), and $MgCl_2$ (Alfa Aesar anhydrous 99.0%).

The salt mixtures were prepared as follows: weighed and mixed to the proper ratio in 100 g batches, thoroughly ground using mortar and pestle, dried at 120 °C in a dry oven for at least 24 h, and finally stored in a desiccator cabinet until further use. Chloride salt mixtures were produced via a purification process under Ar to reduce water content crucial for the corrosion experiment (Phillips et al., 2019; Gomez-Vidal et al., 2017a; Ding and Bauer, 2021).

2.2. *Alloy preparation*

The nominal compositions of the substrate alloys are shown in Table 1.

Metal coupons of initial measurements 15 × 15 × 2 mm were ground and finally polished to a mirror-like finish with a 1 μm diamond suspension. The polished samples were thoroughly cleaned and dried, then dipped into the salt mixture in alumina crucibles.

2.3. *Experimental setup*

Two setups were used in this study, and different conditions were investigated, as summarised in Table 2. The first setup, a horizontal silica tube furnace for partial immersion experiments was used for the exposures to Solar Salt. The exposures were performed isothermally at 650 ± 5 °C in this setup, with a filtered air at a flow rate of 20 ml/min. The second setup used for complete immersion experiments was a top-loader furnace (model top 60 Nabertherm) purchased and redesigned in the workshop to comply with carbonate and chloride exposures in controlled gas environments. The exposures were performed isothermally at 800 ± 5 °C, calibrated at the lowest point of the crucibles, with a gas (Ar or CO_2) flow rate of 50 ml/min for each vessel. Each exposure was conducted twice.

The main purpose of building the Nabertherm setup was as follows: i) ability to test six coupons in each vessel and providing duplicate samples, with an overall of 12 samples tested at a time. ii) Ability to remove coupons directly from the melts; since an otherwise necessary washing procedure of the solidified melts changes the alloy surface chemistry. These samples are dedicated for cross-section analyses. iii) However, the duplicate samples underwent thorough washing for mass change measurements, as recommended in literature (Bradshaw and Clift, 2010; Gomez-Vidal et al., 2017a; Ding, W., 2019; Fähsing et al., 2018; Soleimani Dorcheh et al., 2016; Gomes et al., 2019; Palacios et al., 2020; Encinas-Sánchez et al., 2019).

2.4. *Sample characterisation*

Sample surfaces and cross sections were investigated. Unwashed samples were subjected to cross-section investigation. A thin salt film remained on each sample after the residual melt was poured off. Cross-sections of the exposed samples were prepared either by cold embedding in epoxy resin, hot mounting in bakelite, or by broad ion beam (BIB)

Table 1
Nominal alloy compositions.

Alloy	Fe	Ni	Cr	Al	Si	Mn	Mo	Others
316H	balance	11.5	17	X	0.6	1.5	2.1	C 0.05
304L	balance	9.5	18.5	X	0.4	1.3	X	C 0,02
Kanthal® APMT	balance	X	21	5	0.7	0.4	3	Y; C 0,08

Table 2
Experimental parameters, eutectic melting point, and decomposition temperature of the different salt mixtures. * Decomposition temperature varies with atmosphere; it is was found to be 1000 °C, 700 °C and 670 °C in exposures to CO_2, Ar and air (Vignarooban et al., 2015).

Eutectic salt mixture	*i.) Nitrates* (60 wt% $NaNO_3$- 40 wt % KNO_3)	*ii.) Carbonates* (32.1 wt% Li_2CO_3 –33.4 wt% Na_2CO_3- 34.5 wt% K_2CO_3)	*iii.) Chlorides* (65 wt% KCl- 35% wt% $MgCl_2$)
$T_{eutectic}$ (°C)	230 (Mehos et al., 2017)	398 (Wu et al., 2011)	423 (Ding et al., 2019c)
T_{max} (°C)	530–565 (Mehos et al., 2017)	>650* (Vignarooban et al., 2015)	>800 (Ding et al., 2018a) (Ding et al., 2019c)
Gas	filtered air	CO_2	argon
Exposure temperature	650 °C (72 h cyclic refilling of the salt)	800 °C (isothermal) (336 h cyclic refilling of the salt)	800 °C (isothermal) (336 h cyclic refilling of the salt)
Total exposure time	168 & 1000 h	168 & 1000 h	168 & 500 h

milling with a Leica TIC 3X instrument.

Washed samples were weighed and characterised with scanning electron microscopy (SEM) and energy-dispersive X-ray spectroscopy (EDX) using a JEOL JSM-7800F Prime or Phenom ProX Desktop SEM equipped with an EDX detector. The electron beam used to collect EDX spectra was operated at an accelerating voltage of 15 kV. A Siemens D5000 powder diffractometer with grazing-incidence geometry was used for XRD surface analysis. As it is hard to detect Li with EDX analysis because of the Li low molecular weight, it was important to use XRD to detect the Li-containing corrosion products. Therefore, the results for washed samples should be considered with caution.

3. Results and discussion

A quantitative overview of weight change and corrosion depth data showed a clear distinction between the effects of different salt melts on the stainless steels and Kanthal APMT, see Fig. 1. The corrosion attack was ranked according to five different measurables, three of them are presented in Fig. 1. These measurables are outward-growing facetted crystal growth, compact oxide scale thickness, and internal attack by secondary oxidants such as nitridation, carburisation, or chlorination. The fourth parameter is the average number of large oxide nodules on each coupon in conjunction with a local internal corrosion attack feature. The fifth parameter is the mass change of the alloys after exposure, as shown in Fig. 2. However, mass changes must be considered with caution even though the experiments were diligently conducted.

Fig. 2 shows all the mass change data collected for 304L and Kanthal APMT at 800 °C in carbonate and chloride melts. No comparable mass change data for the nitrates' exposures will be reported here because the samples were only partially immersed in nitrate melts.

Exposures to carbonate melts caused mass gains for 304L and Kanthal APMT. The mass change trends indicated with dashed trendlines must be considered with the utmost caution due to the intense handling of the samples, i.e., quenching, rinsing, and drying after exposure. However, few assumptions will be made based on the mass change data in the context of our overall data collection. Kanthal APMT had a much lower mass gain, and the overall mass gain trendline also reflects sub-parabolicity. The last measurement after 1000 h, however, deviates from the indicated curve. A change in oxide morphology was found, which indicates a difference in aluminium consumption, as discussed in Section 3.2.2. Alloy 304L maintained steady-state behaviour after a fast-initial mass gain. Indications of a rapid corrosion-dissolution process supported by the steady-state progression of the mass change curve will be reported in Section 3.2.1.

Exposure to chloride melts, on the other hand, caused accelerating mass loss behaviour for both alloys. This behaviour was slower for Kanthal APMT samples.

3.1. *Corrosion performance of the alloys in solar salt*

We will discuss the results from alloys exposed to the commercially used Solar Salt blend in this section. A comparison of the time-evolution of XRD spectra for stainless steel 316H and Kanthal APMT, see Fig. 3, shows that no alloy-specific signal was detectable after 168 h for the 316H stainless steel, while this signal was present for Kanthal APMT, indicating the presence of a thin alumina scale at the surface of Kanthal APMT.

The diffraction pattern observed for alloy 316H after one week exposure in Solar Salt confirms the presence of sodium ferrite species, which is in agreement with prior publications (Kruizenga and Gill, 2014; Tzvetkoff and Kolchakov, 2004; Soleimani Dorcheh et al., 2016;

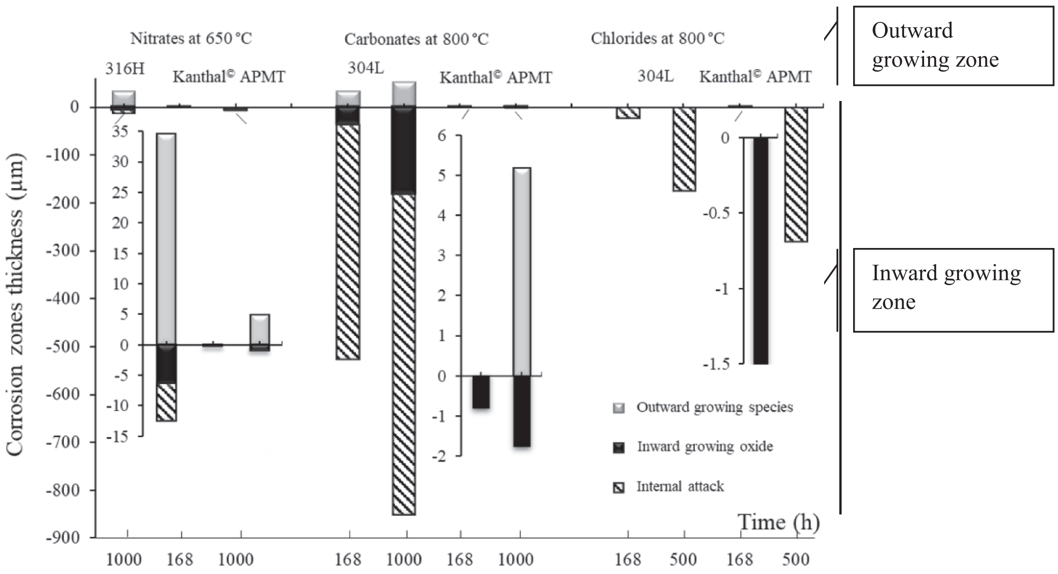

Fig. 1. Comparative schematic for all corrosion layer thickness measurements in this study. The differences between outward-growing and inward-growing species are distinguished. The horizontal axis is placed at the apparent initial material surface, where corrosion layer thickness equals zero.

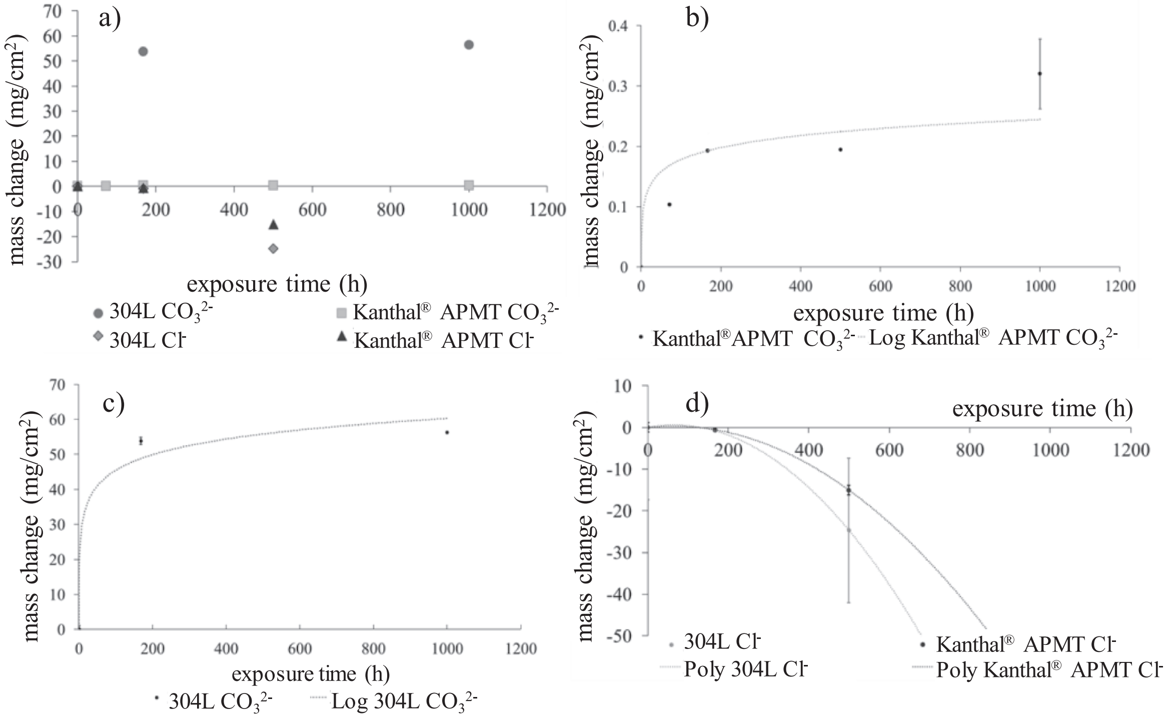

Fig. 2. a) Mass change plot for 304L and Kanthal® APMT in carbonate and chloride melts at 800 °C, (without error bars), b) mass gain of Kanthal® APMT in carbonates and trendline, c) mass gain of alloy 304L in carbonates and trendline, d) mass loss of 304L and Kanthal® APMT in chlorides and trendline. Different scales must be taken into consideration. b)-d) show error bars indicating the minimum and maximum around the plotted average value.

Fernández et al., 2015a).

After exposure, Kanthal APMT presented sodium aluminates and sodium ferrites. Corresponding potassium containing species were absent for both alloys.

3.1.1. *Microstructural evolution of alloy 316H in solar salt at 650 °C*

In this chapter, we discuss a metallographic cross-section of alloy 316H after 1000 h exposure in Solar Salt. Electron backscatter images and element maps, presented in Fig. 4, reveal the presence of four zones: i) a thick sodium ferrite scale with an average thickness of 40 μm. ii) an intersecting oxide zone enriched in manganese and nickel, iii) a chromium rich metal oxide interface iv) internal attack consisting of chromium nitride vail. The chromium enrichment is an attempt of the alloy to form a protective chromia scale. However, this attempt fails, which is evident when the precipitates in the suboxide region are analysed. Severe chromium depletion and chromium capture by the formation of chromium nitride render the overall performance of the oxide scale as non-protective. Alloy 316H developed a 7 μm thick chromia scale after exposure to Solar Salt for 1000 h at 650 °C. Alkali ferrite crystals grew rapidly outwards (25 μm average) on this sample. Internal nitridation with an average thickness of 6 μm was detected beneath the oxide layer.

3.1.2. *Microstructural evolution of alloy Kanthal APMT in solar salt at 650 °C*

In strong contrast to the 316H results, Kanthal APMT showed good corrosion resistance to Solar Salt at 650 °C for 168 h and 1000 h. In Fig. 5., Kanthal APMT samples show smooth sodium aluminate scales at the surface and locally occurring nodule formation that was identified as sodium ferrite, in agreement with the species identified in the XRD spectra, Fig. 3.

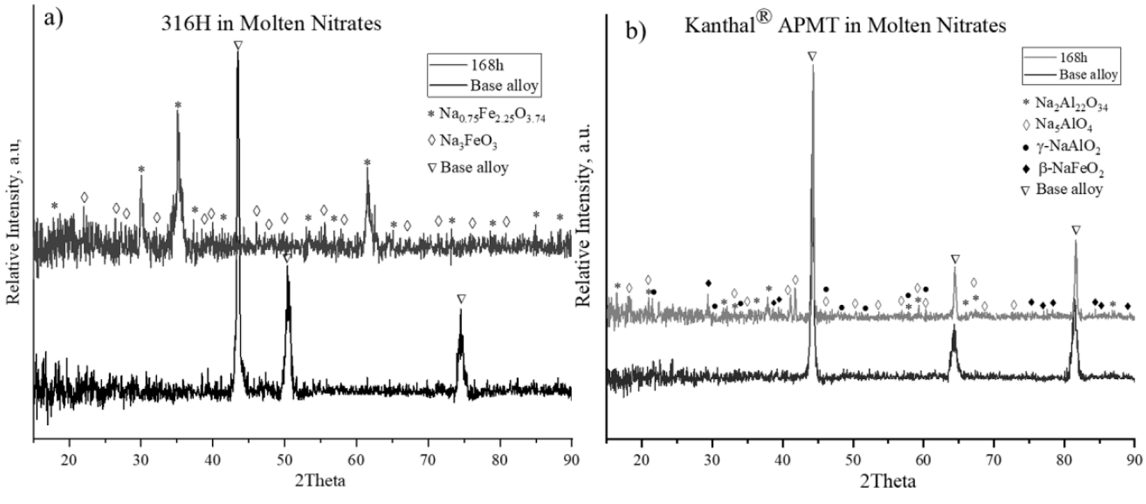

Fig. 3. XRD pattern for a) alloy 316H and b) Kanthal® APMT exposed to molten nitrate salt mixture at 650 °C for 168 h.

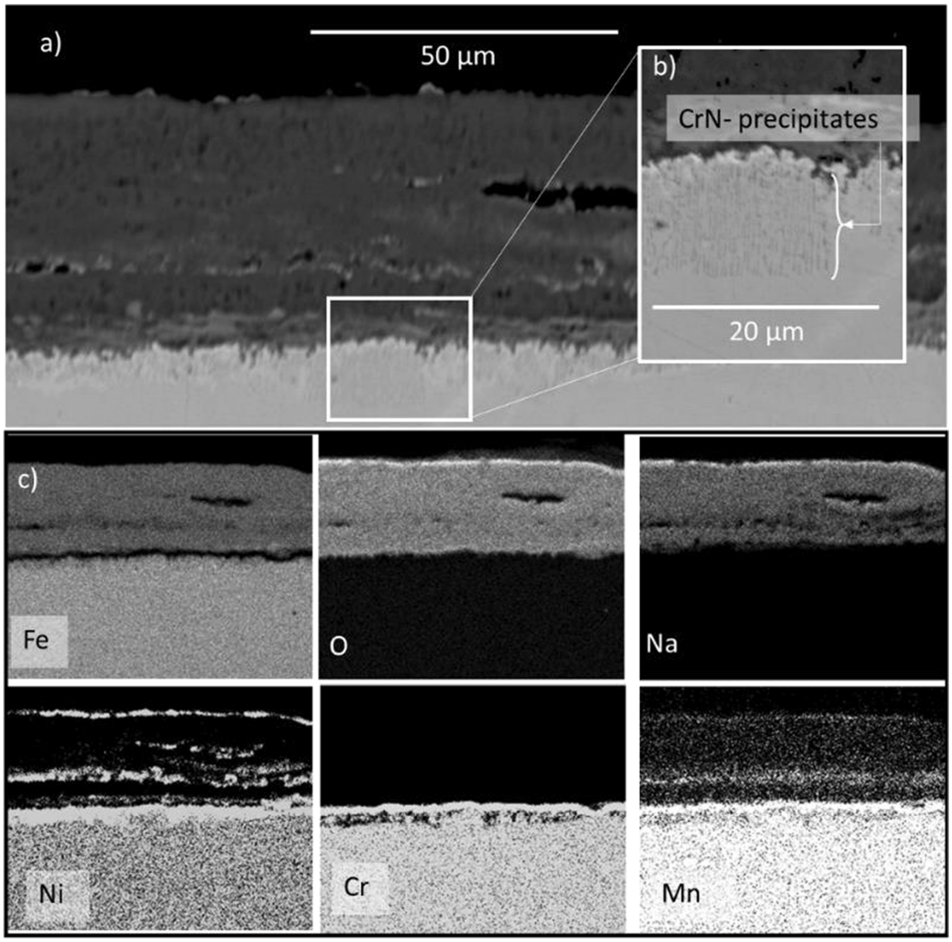

Fig. 4. a) Backscatter electron image of an alloy 316H cross section after 1000 h exposure to Solar Salt. b) Higher magnification of the suboxide zone highlighted in image a). c) Element maps of the oxide scale corresponding to image a).

An underlying alumina scale beneath scars sodium ferrite nodules indicates an early stage of sodium ferrite formation and inability for further growth of those nodules.

Internal nitridation, as found for 316H, was not detected in Kanthal APMT samples. This fact is crucial, since any direct contact of alkali nitrates with the alloy or the formation of a nitrogen-permeable oxide should be prevented.

Any nitrogen ingress into the FeCrAl alloy drains the aluminium activity by the formation of thermodynamically stable AlN precipitates, until undergoing a critical concentration sustaining oxide scale growth. In case a defect occurs during sodium aluminate formation, Eq. 1, internal precipitation will form aluminium nitride, Eq.4, over chromium nitride, Eq.5.

3.2. *Corrosion performance of the alloys in alkali carbonate melt*

XRD spectra for the surfaces of alloy 304L and Kanthal APMT samples and their time-dependent evolution are shown in Fig. 6 a and b. Note that XRD was the only method used to detect lithium species in the corrosion products.

The alloy signal from the 304L sample was no longer detectable after one week of exposure at 800 °C. Spectra for the 304L sample indicate spinel oxide and lithiated oxide species, as reported in previous studies (Cruchley et al., 2016; Sah et al., 2018). Kanthal APMT, on the other hand, maintained its alloy signal for at least 1000 h, indicating a significantly thinner and slow growing oxide scale. Interestingly, after 168 h the α-lithium aluminate signal initially found on the Kanthal APMT surfaces was accompanied by a γ-lithium aluminate signal after

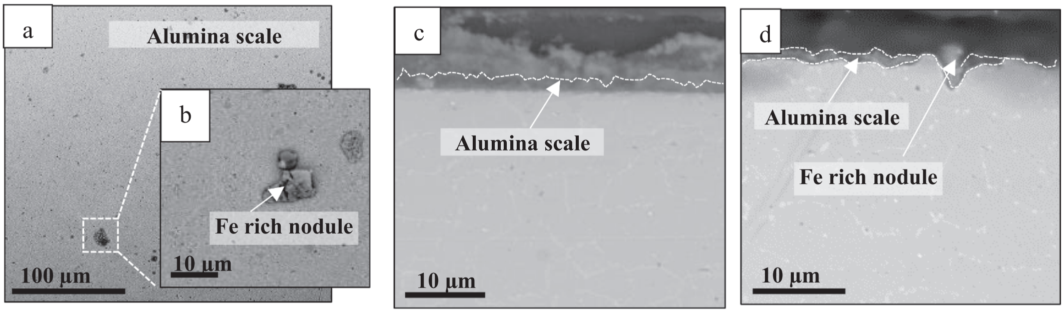

Fig. 5. Backscatter electron images of Kanthal® APMT samples after exposure to solar salt. a) and b) top view after 168 h. Cross section after c) 168 h and d) 1000 h.

1000 h of exposure.

3.2.1. Microstructural evolution of alloy 304L in 33 wt% Li_2CO_3 -32 wt% Na_2CO_3- 34 wt% K_2CO_3 at 800 °C

Key images are summarised in Fig. 7, including top view images and cross sections of alloy 304L exposed for 168 h and 1000 h at 800 °C in molten carbonates. The surface morphology of the 304L sample was similar after both exposure times; the alloy surface was completely covered by rapidly growing octahedral crystallites. This finding is in agreement with the literature (Attia et al., 2002; Sarvghad et al., 2017). Lithium ferrite crystals rapidly grew with time on the surface of the 304L samples: from 33 μm after 168 h to 52 μm after 1000 h on average. Li-containing corrosion products were expected to form, based on the basicity of alkali carbonates (Spiegel et al., 1997; Evans et al., 1977) and correlate well with the spectra in Fig. 6a. Sodium and potassium corrosion species were not identified in said spectra. One critical question is whether the carbon dioxide gas environment provides sufficient oxidation potential to oxidise metallic iron.

Underneath the alkali ferrite crystals, a multi-layer oxide scale was revealed, which is in agreement with previous studies (Attia et al., 2002; Sarvghad et al., 2017).

The internal oxide scale propagated more rapidly than the outer crystallite scale. This zone evidently grew linear with time, since its thickness increased from 35 μm to 180 μm by prolonging the exposure time by a factor of six. The internal oxidation zone's chemistry is heterogeneous, as can be seen in the Z-contrast in the electron backscatter images in Fig. 7. EDX spot analysis identified the darkest contrast as chromium-rich iron-chromium spinel. The medium shades contain mainly iron oxide, and the brightest spots contain high nickel fractions. None of the oxides offered protection; both of the oxide species allowed oxygen and carbon to permeate into the alloy causing carburisation ($Cr_{23}C_6$) beyond the internal oxidation zone, as shown in Fig. 7d and g. Based on the SEM/EDX analysis, the internal attack in form of carbide precipitation has reached a depth of ~490 μm after 168 h and throughout the sample after 1000 h.

The precipitation of chromium carbides drains chromium activity from the alloy, inhibiting outward diffusion towards the metal/oxide interface to contribute to the formation of a protective oxide scale. Chromium carbide precipitates also lead to changes in the microstructure and mechanical properties of the alloy.

Severe internal oxidation and carburisation would point towards a significant mass gain over time. On the contrary, mass gain appears stagnant in the plot Fig. 2c. One reason could be a substantial mass loss due to the dissolution of metal ions into the carbonate melt as indicated by the melts' colouring. Chromia reacts exothermically with lithium carbonate and carbon dioxide to form liquid hexavalent lithium chromate at 800 °C (Encinas-Sánchez et al., 2018).

Alloy 304L was doubly compromised in its ability to form a protective chromium-rich oxide scale by a severe internal attack via carburisation and the dissolution of hexavalent species into the carbonate melt.

3.2.2. Microstructural evolution of Kanthal APMT in 32.1 wt% Li_2CO_3 -33.4 wt% Na_2CO_3- 34.5 wt% K_2CO_3 at 800 °C

Kanthal APMT shows very different top view features in Fig. 8 compared to the 304L sample in Fig. 7. After 168 h exposure, a smooth surface with very small $LiAlO_2$ crystallites emerged (Fig. 8a). The reaction of aluminium and chromium with sodium and lithium carbonates is spontaneous. Among these reactions, lithium aluminate has the highest exothermicity.

After 1000 h, some significantly larger crystallites became locally visible see Fig. 8b. These crystals were identified as γ-$LiAlO_2$ as shown in Fig. 6b.

While after 168 h exposure, only one lithium aluminate phase, α-$LiAlO_2$, was detected (Fig. 6b), a second phase, γ-$LiAlO_2$, emerged after 1000 h of exposure, simultaneously with the appearance of large prismatic crystals. Several studies have been published on the thermal physical properties of the two lithium aluminate polymorphs (Danek et al., 2004; Heo et al., 2017; Bennett et al., 2003; Choi et al., 2010). α-$LiAlO_2$ is stable up to ~747–777 °C before the $\alpha \rightarrow \gamma$- $LiAlO_2$ phase transformation occurs. This transformation depends on different parameters e.g., operating temperature, environment, and exposure time. The transformation of α-$LiAlO_2$ to γ-$LiAlO_2$ may affect the corrosion resistivity of an alloy. Small α- $LiAlO_2$ crystallites form a protective film, while γ-$LiAlO_2$ grows large individual crystals (Heo et al., 2017). This feature renders the α- to γ-$LiAlO_2$ phase transformation undesirable. This transformation may also explain the larger window of uncertainty for the last mass change measurements after 1000 h in Fig. 2b. These measurements indicate an accelerating oxidation process.

The overall mass gain of Kanthal APMT was reduced by two magnitudes, compared to 304L, and no aluminium had been dissolved from the alloy into the melt after 1000 h. However, the overall impact of the phase transformation must be considered in long-term assessments.

Cross-section analysis was performed to test for an internal attack coinciding with the different lithium aluminate morphologies, Fig. 8c and 8d. The sample exposed for 168 h succeeded in forming a uniform, thin, and dense α-$LiAlO_2$ scale, with a thickness in the range of 0.5–3.2

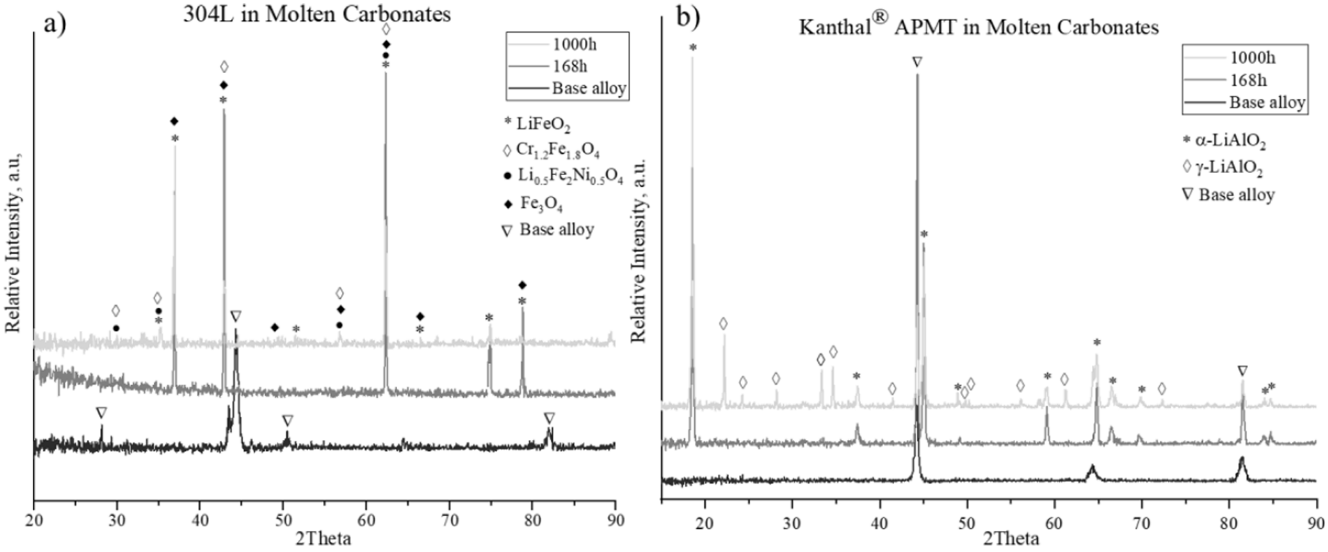

Fig. 6. XRD pattern of a) 304L and b) Kanthal® APMT after exposure to alkali carbonates at 800 °C for 168 h and 1000 h.

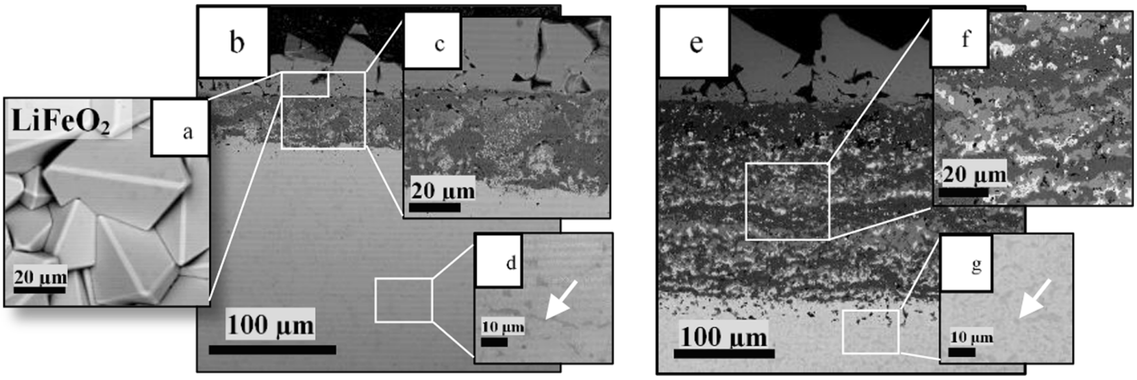

Fig. 7. a) SEM surface morphology of 304L alloy exposed to carbonate melt at 800 °C for 168 h, b) SEM cross section of 304L alloy exposed to carbonate melt at 800 °C for b) 168 h and e) for 1000 h. Higher magnification cross section shows: the internal oxidation zone for c) 168 h and f) 1000 h, and chromium carbide precipitates for d) 168 h and g) 1000 h.

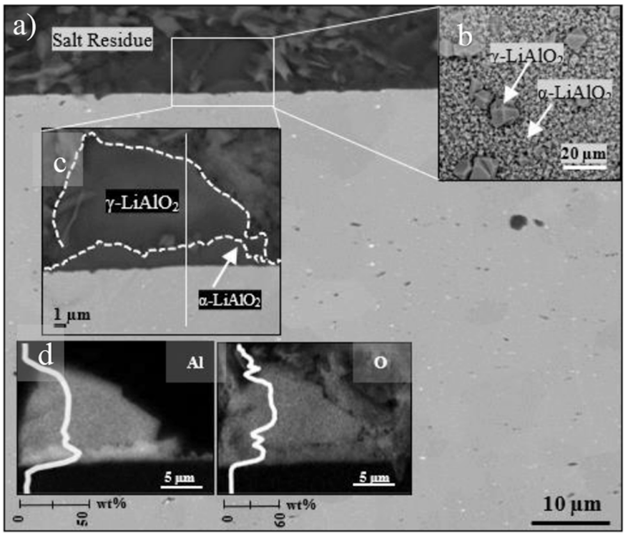

Fig. 8. a) Overview backscatter electron image of a Kanthal® APMT cross section exposed to molten carbonate salt mixture at 800 °C for 1000 h, b) top view image of the surface, c) higher magnification of the cross section, d) aluminum and oxygen element maps of position c) and corresponding lines cans.

µm. The α-$LiAlO_2$ scale thickness increased slightly after 1000 h, but the second morphology, γ-$LiAlO_2$, nucleated and formed larger crystals (about 6 µm high) on top of the underlying α-$LiAlO_2$ scale. Additional EDX element maps clearly show the transition front between the two aluminate morphologies. An additional line scan showed no aluminium depletion zone in the alloy's subsurface, for at least 1000 h exposure, and no indication of any internal attack.

3.3. Corrosion performance of the alloys in magnesium potassium chlorides at 800 °C

A comparison of the XRD spectra for the stainless steel 304L and Kanthal APMT after different exposure times are shown in Fig. 9. The only detectable corrosion species on 304L was magnesium oxide. $MgAl_2O_4$ and traces of a MgCrAl spinel oxide were found on Kanthal APMT. No metal chlorides were identified via XRD.

Only oxides with very high thermodynamic stability can form under such extreme conditions, other species dissolve into the chloride melt. Magnesium oxide and magnesium aluminate are such stable species (Ellingham, 1944).

Furthermore, the XRD spectra for the exposed Kanthal APMT had clear signals for a molybdenum-rich intermetallic phase, a so called Laves phase. The position and role of the Laves phase will be discussed more specifically in Section 3.3.2.

The mass change data in Fig. 2 indicates that both alloys underwent accelerating mass loss, more for 304L than for Kanthal APMT. The dissolution processes of alloy elements is anticipated, in agreement with previously published data (Ding, W.J. et al., 2019).

3.3.1. Microstructural evolution of alloy 304L in 65 wt% KCl- 35% wt% MgCl2 at 800 °C

Alloy 304L underwent immediate leaching of alloy species by the salt. Residual humidity in the salt can only stabilise magnesium oxide originating from the melt. After 168 h of exposure a thin MgO film was found on the 304L surface (Fig. 10). Alloy species, i.e., chromium, nickel, and iron, were detected in salt particles on top of the sample as shown in EDX maps (Fig. 10b). The loss of chromium into chloride melts has also been reported by Ding et al. (Liu et al., 2016; Ding et al., 2018b). Cavities reaching ~10 µm deep int the alloy's microstructure after 168 h, formed where metals have been leached into the melt. In return, these cavities were found filled with magnesium oxide. A deep and easily distinguishable depletion zone had formed after 500 h as shown in the Chromium EDX map in Fig. 10e. This zone reached several hundred µm into the alloy and contained only about 2% chromium (see line-scan Fig. 10e). Cavities within the depletion zone, filled with magnesium oxide, and traces of chlorides, were found more than 150 µm into the alloy. Similar results have been reported by Ding et al. (2018b).

Humidity has been identified as an impurity with the highest acceleration effect on the corrosion of stainless steels (Tian and Zhao, 2013; Ge et al., 2018; Copson, 1953; Ding et al., 2019c). Despite the additional drying sequence for the salts in inert gas prior to exposure, the impact of remaining humidity has proven substantial. This must be taken into account when considering the dimensions of the several thousand tons of salt required for a thermal storage reservoir in a CSP. Humidity control is a major economic factor.

3.3.2. Microstructural evolution of alloy Kanthal APMT in 64.41 wt% KCl-35.59% wt% $MgCl_2$ at 800 °C

Besides the $MgAl_2O$ identified via XRD, alumina particles were found by EDX top-view spot analysis (Fig. 11a).

Fig. 11b shows a bright Z-contrast in the subsurface region. Interestingly, this bright contrast was caused by molybdenum enrichment. This enrichment was sufficient to stabilise Laves phase precipitates.

The thermodynamic calculations confirm a two-phase regime at 800 °C comprising BCC and C14 Laves phase with the approximate composition $(Fe_{0.75}Cr_{0.25})_2Mo$.

No internal attack was detected after 168 h.

After 500 h, however, the chloride melt compromised the alloy

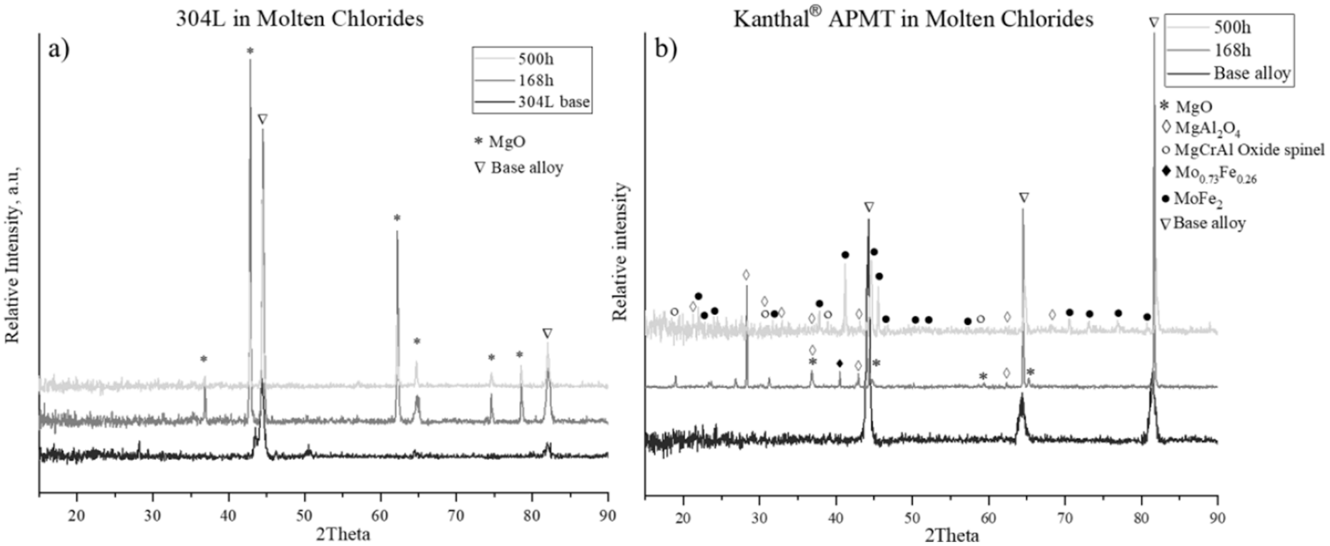

Fig. 9. XRD patterns for a) 304L and b) Kanthal® APMT alloy exposed to chloride melts at 800 °C for 168 h and 500 h.

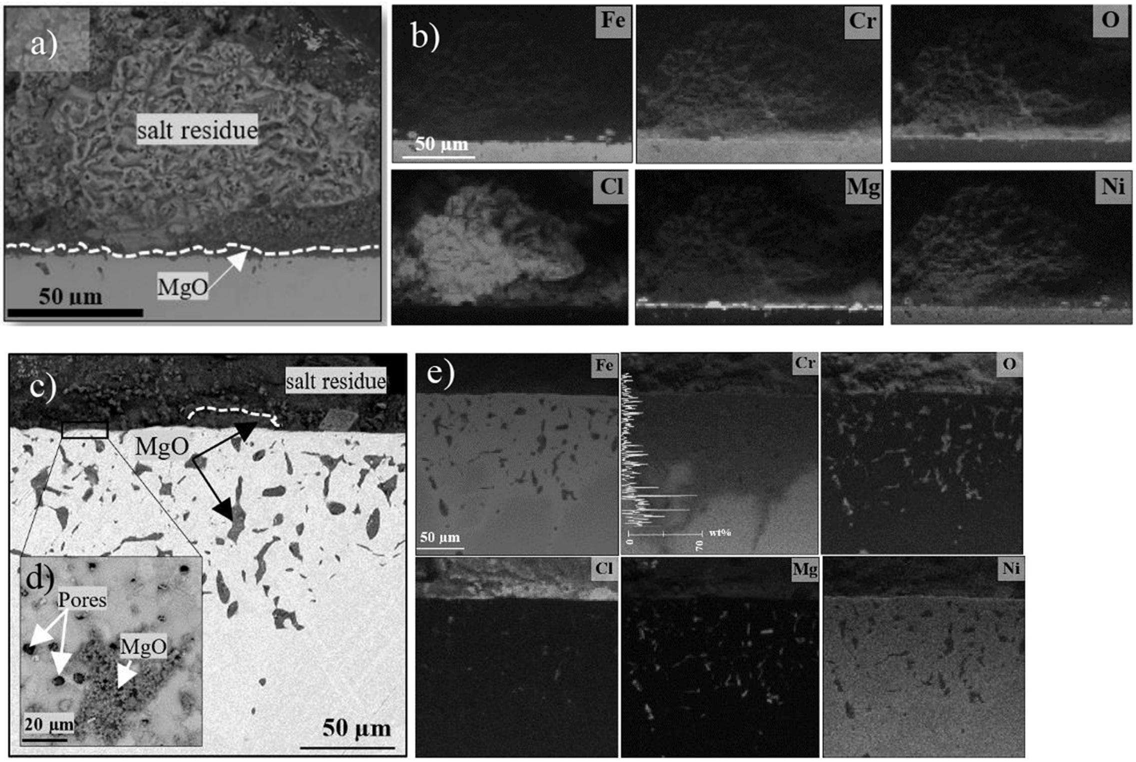

Fig. 10. Alloy 304L cross section after exposure to molten chlorides at 800 °C for a) 168 and c) 500 h, and corresponding EDX element maps b) and e). The chromium element map in e) is extended by a line scan to highlight chromium depletion. The higher magnification in the top view image d) shows magnesium oxide and pores distributed over the surface of the sample.

integrity by selectively leaching aluminium, creating a cavity network to a depth of 280 µm. Only fragments of alumina remained at the surface. The bare alloy and a pattern of pores was present at the surface. A deep-reaching depletion of aluminium was found in a cross-section analysis of the attacked material, see line scan in Fig. 11h. The remaining cavities were filled with magnesium oxide and chlorides. Aluminium leached most efficiently through the cavity network, leaving a molybdenum rich Laves phase rim around several individual cavities. After 500 h, such Laves phase rims around cavities are measured at the minimum distance of ~100 µm from the metal/salt interface. Therefore, it can be concluded that the Laves phase precipitates were transient in the overall leaching process and had already been dissolved in the upper region of the sample.

The overall mass loss for Kanthal APMT was lower than that for 304L. This was due to the lower degree of chromium leaching found for Kanthal APMT, however, the internal attack progressed deeper, compromising the integrity of the alloy.

In a previous exposure study by Gomez-Vidal *et al.*, Kanthal APMT was pre-oxidised before being brought into contact with the chloride melt. This procedure did not result in Laves phase precipitates (Gomez-Vidal et al., 2017b).

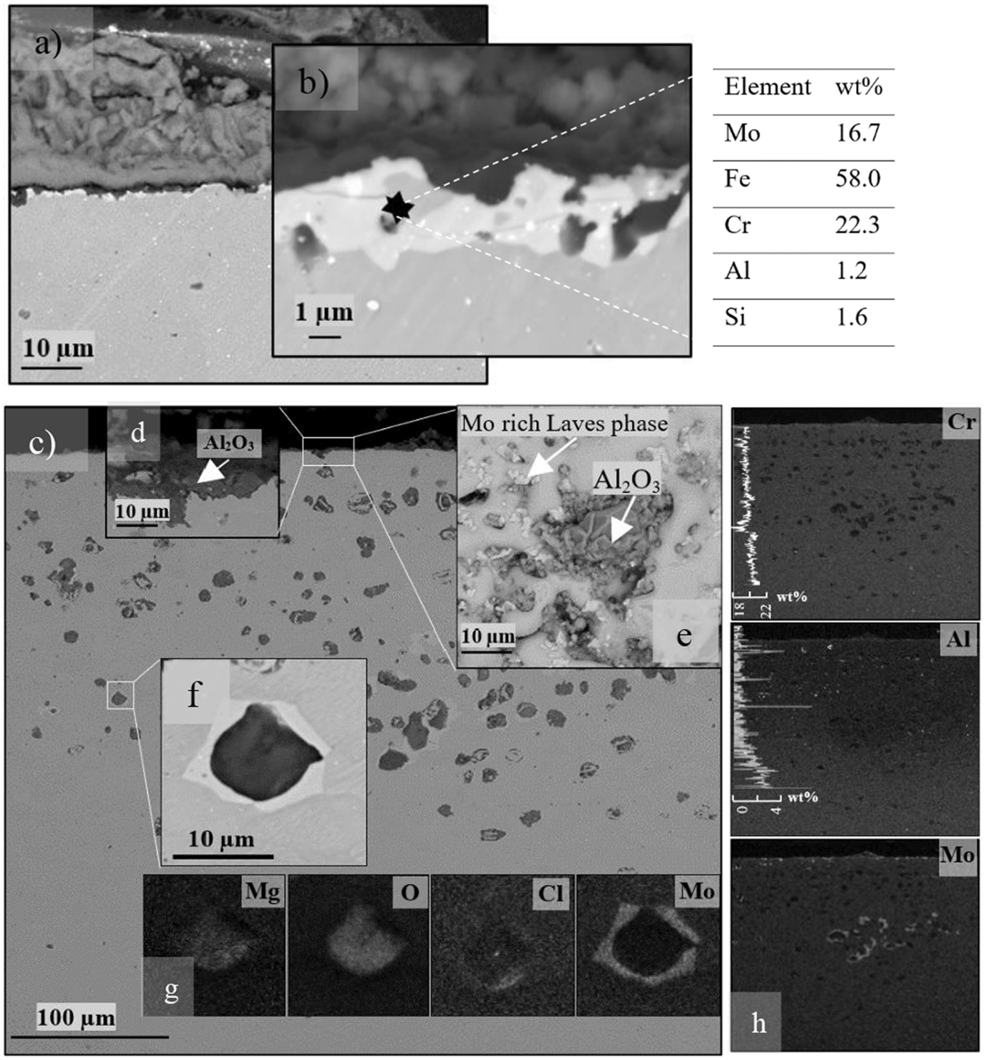

Element	wt%
Mo	16.7
Fe	58.0
Cr	22.3
Al	1.2
Si	1.6

Fig. 11. Kanthal® APMT cross section after exposure to molten chlorides at 800 °C for a) 168 and c) 500 h, and corresponding EDX element maps b) and g, h). The aluminum and chromium element maps in h) were extended with line scans to highlight aluminum depletion and the lower degree of chromium leaching. The higher magnification in the top view image e) shows magnesium oxide and pores distributed over the surface. The higher magnification cross section in d) shows a fragment of alumina scale remaining at the surface. f) shows Laves phase rims around voids.

4. Conclusions

Three eutectic melts that are currently under consideration for heat transfer fluid or a thermal energy storage medium, alkali nitrates, alkali carbonates, and chlorides were brought into contact with the stainless-steel alloy 304L or 316H and Kanthal APMT.

Aspects of oxidation, dissolution, and internal attack on the alloys were systematically compared.

Material degradation in contact with alkali nitrates was comparatively slow for the stainless steel and Kanthal APMT, which was anticipated because of the lower exposure temperature. It should, however, be noted that the stainless steel underwent gradual oxide scale growth, and nitrogen permeated into the bulk alloy, which caused chromium nitride precipitation in 316H alloy. This in turn significantly lowered the chromium activity of the alloy. Internal nitride precipitation, however, is not as severe as carburisation that occurs on alloy 304L in an alkali carbonates melt. Carbide precipitation reached several hundreds of micrometres deeper into the bulk alloy after the same exposure times, which altered the overall chemistry. Kanthal APMT, on the other hand, remained nearly unaffected when exposed to carbonates or to nitrates and did not suffer from an internal attack. However, under the influence of lithium ions from the carbonates melt, a slow conversion from the film-growing α-$LiAlO_2$ to the locally growing larger γ-$LiAlO_2$ crystallites occurred, and the long-term effect of this on aluminium consumption needs further evaluation. No internal scarburisation was observed for at least 1000 h.

Chlorides melt leached elements from both 304L and Kanthal APMT. Chromium and nickel were gradually leached from the stainless-steel alloy 304L into the melt, and the resulting cavities in the microstructure were filled with melt components. Kanthal APMT, however, resisted severe leaching of alloy elements during the first 168 h by forming magnesium aluminate on the sample surface. This resistance broke down after 500 h, resulting in the rapid leaching of aluminium, which reached deeper in Kanthal APMT than the depth of chromium leaching found for alloy 304L. Cavities created by the leaching were filled with magnesium oxide and chloride surrounded by a $(Fe_{0.75}Cr_{0.25})_2Mo$ Laves phase, indicating that molybdenum leached much slower than chromium and aluminium. Laves phase rims seemed to prevent Kanthal APMT from rapid chromium leaching, compared to alloy 304L, thus explaining the overall lower mass loss measured for Kanthal APMT.

The overall conclusion is that nitrates are the best choice as a calculated risk, since even the stainless steel that suffered an internal attack reacted comparably slow and predictably. Alkali carbonates degraded the stainless steel unacceptably fast through carburisation. Kanthal APMT is a very good alternative in this case provided that the α- to γ-transition of $LiAlO_2$ is slow and does not lead to any aluminium depletion for at least 1000 h. Chloride melts were detrimental to both alloys investigated. However, molybdenum proved to be a possible influencing element. Molybdenum formed a Laves phase barrier to chromium leaching, which however, did not prevent the rapid dissolution of aluminium from the alloy.

Declaration of Competing Interest

The authors declare that they have no known competing financial interests or personal relationships that could have appeared to influence the work reported in this paper.

Acknowledgments

This work was financially supported by Vinnova within the ALSTEr Project as part of the Jernkontoret initiative Metalliska Material. The Swedish Energy Agency continues to financially support our efforts within the thermal storage for SOLEL initiative under contract number 44653-1 (Jan-Erik Svensson) and as a partner in the High Temperature Corrosion Competence Centre (Lars-Gunnar Johansson).

References

Attia, A.A., Salih, S.A., Baraka, A.M., 2002. Corrosion and passivation behaviors of some stainless steel alloys in molten alkali carbonates. Electrochim. Acta 48 (2), 113–118.

Bennett, M.J., Newton, R., Nicholls, J.R., 2003. The behaviour of commercial FeCrAIRE alloys in nitrogen-oxygen - water vapour bioxidant environments. Mater. High Temp. 20 (3), 347–356.

Bradshaw, R.W., Goods, S.H., 2001. Corrosion resistance of stainless steels during thermal cycling in alkali nitrate molten salts. ; Sandia National Laboratories (SNL), Albuquerque, NM, and Livermore, CA (United States), p. Medium: ED; Size: 39 p.

Bradshaw, R.W., Clift, W.M., 2010. Effect of chloride content of molten nitrate salt on corrosion of A516 carbon steel. Sandia National Laboratories, Albuquerque, New Mexico 87185 and Livermore, California 94550, pp. 1–27.

Caitlin, M., Y., S., W., C., Maclaurin, G., Turchi, C., Mehos, M., 2019. The Potential Role of Concentrating Solar Power within the Context of DOE's 2030 Solar Cost Target National Renewable Energy Laboratory, p. https://www.nrel.gov/docs/fy19osti/71912.pdf.

Cheng, W.-J., Chen, D.-J., Wang, C.-J., 2015. High-temperature corrosion of Cr–Mo steel in molten LiNO3–NaNO3–KNO3 eutectic salt for thermal energy storage. Sol. Energy Mater. Sol. Cells 132, 563–569.

Choi, H.J., Lee, J.J., Hyun, S.H., Lim, H.C., 2010. Phase and microstructural stability of electrolyte matrix materials for molten carbonate fuel cells. Fuel Cells 10 (4), 613–618.

Copson, H.R., 1953. Corrosion of heating electrodes in molten chloride baths. J. Electrochem. Soc. 100 (6), 257.

Cruchley, Samuel, Evans, Hugh, Taylor, Mary, 2016. An overview of the oxidation of Ni-based superalloys for turbine disc applications: surface condition, applied load and mechanical performance. Mater. High Temp. 33 (4-5), 465–475. https://doi.org/10.1080/09603409.2016.1171952.

Danek, V., Tarniowy, M., Suski, L., 2004. Kinetics of the α → γ phase transformation in LiAlO2 under various atmospheres within the 1073–1173 K temperatures range. Journal of Materials Science 39 2429–2435.

de Miguel, M.T., Encinas-Sánchez, V., Lasanta, M.I., García-Martín, G., Pérez, F.J., 2016. Corrosion resistance of HR3C to a carbonate molten salt for energy storage applications in CSP plants. Sol. Energy Mater. Sol. Cells 157, 966–972.

Ding, W., Bauer, T., 2021. Progress in research and development of molten chloride salt technology for next generation concentrated solar power plants. Engineering 7 (3), 334–347.

Ding, W., Bonk, A., Bauer, T., 2018a. Corrosion behavior of metallic alloys in molten chloride salts for thermal energy storage in concentrated solar power plants: a review. Front. Chem. Sci. Eng. 564–576.

Ding, W., Bonk, A., Bauer, T., 2019. Molten chloride salts for next generation CSP plants: Selection of promising chloride salts & study on corrosion of alloys in molten chloride salts. AIP Conference Proceedings 2126(1), 200014.

Ding, W.J., Gomez-Vidal, J., Bonk, A., Bauer, T., 2019b. Molten chloride salts for next generation CSP plants: electrolytical salt purification for reducing corrosive impurity level. Sol. Energy Mater. Sol. Cells 199, 8–15.

Ding, W., Shi, H., Xiu, Y., Bonk, A., Weisenburger, A., Jianu, A., Bauer, T., 2018b. Hot corrosion behavior of commercial alloys in thermal energy storage material of molten MgCl2/KCl/NaCl under inert atmosphere. Solar Energy Materials and Solar Cells. Elsevier B.V. 22–30.

Ding, W., Shi, H., Jianu, A., Xiu, Y., Bonk, A., Weisenburger, A., Bauer, T., 2019a. Molten chloride salts for next generation concentrated solar power plants: mitigation strategies against corrosion of structural materials. Solar Energy Materials and Solar Cells. Elsevier B.V. 298–313.

Ellingham, J.T., 1944. Transactions and communications. J. Soc. Chem. Ind. 63 (5), 125–160.

Encinas-Sánchez, V., de Miguel, M.T., García-Martín, G., Lasanta, M.I., Pérez, F.J., 2018. Corrosion resistance of Cr/Ni alloy to a molten carbonate salt at various temperatures for the next generation high-temperature CSP plants. Sol. Energy 171, 286–292.

Encinas-Sánchez, V., de Miguel, M.T., Lasanta, M.I., García-Martín, G., Pérez, F.J., 2019. Electrochemical impedance spectroscopy (EIS): An efficient technique for monitoring corrosion processes in molten salt environments in CSP applications. Sol. Energy Mater. Sol. Cells 191, 157–163.

Evans, H.E., Hilton, D.A., Holm, R.A., 1977. Internal attack during the oxidation of nitrided stainless steels. Oxid Met. 11 (1), 1–21.

Fähsing, D., Oskay, C., Meißner, T.M., Galetz, M.C., 2018. Corrosion testing of diffusion-coated steel in molten salt for concentrated solar power tower systems. Surface and Coatings Technology. Elsevier B.V. 46–55.

Fernández, A.G., Lasanta, M.I., Pérez, F.J., 2012. Molten salt corrosion of stainless steels and low-Cr steel in CSP plants. Oxid. Met. 78 (5–6), 329–348.

Fernández, A.G., Rey, A., Lasanta, I., Mato, S., Brady, M.P., Pérez, F.J., 2014. Corrosion of alumina-forming austenitic steel in molten nitrate salts by gravimetric analysis and impedance spectroscopy. Mater. Corros. 267–275.

Fernández, A.G., Cortes, M., Fuentealba, E., Pérez, F.J., 2015a. Corrosion properties of a ternary nitrate/nitrite molten salt inconcentrated solar technology. Renew. Energy 177–183.

Fernández, A.G., Galleguillos, H., Fuentealba, E., Pérez, F.J., 2015b. Corrosion of stainless steels and low-Cr steel in molten Ca(NO3)2–NaNO3–KNO3 eutectic salt for direct energy storage in CSP plants. Sol. Energy Mater. Sol. Cells 141, 7–13.

Fernández, A.G., Pineda, F., Walczak, M., Cabeza, L.F., 2019. Corrosion evaluation of alumina-forming alloys in carbonate molten salt for CSP plants. Renew. Energy 140, 227–233.

Frangini, S., Loreti, S., 2006. The role of temperature on the corrosion and passivation of type 310S stainless steel in eutectic (Li + K) carbonate melt. J. Power Sources 800–804.

Ge, Z., Huang, Y., Ding, Y., 2018. Eutectic composition-dependence of latent heat of binary carbonates (Na2CO3/Li2CO3). Sol. Energy Mater. Sol. Cells 179, 202–206.

Gomes, A., Navas, M., Uranga, N., Paiva, T., Figueira, I., Diamantino, T.C., 2019. High-temperature corrosion performance of austenitic stainless steels type AISI 316L and AISI 321H, in molten Solar Salt. Solar Energy. Elsevier 408–419.

Gomez-Vidal, J.C., Tirawat, R., 2016. Corrosion of alloys in a chloride molten salt (NaCl-LiCl) for solar thermal technologies. Solar Energy Materials and Solar Cells. Elsevier 234–244.

Gomez-Vidal, J.C., Noel, J., Weber, J., 2016. Corrosion evaluation of alloys and MCrAlX coatings in molten carbonates for thermal solar applications. Solar Energy Materials and Solar Cells. Elsevier 517–525.

Gomez-Vidal, J.C., Fernandez, A.G., Tirawat, R., Turchi, C., Huddleston, W., 2017a. Corrosion resistance of alumina-forming alloys against molten chlorides for energy production. I: Pre-oxidation treatment and isothermal corrosion tests. Sol. Energy Mater. Sol. Cells 166, 222–233. https://doi.org/10.1016/j.solmat.2017.02.019.

Gomez-Vidal, J.C., Fernandez, A.G., Tirawat, R., Turchi, C., Huddleston, W., 2017b. Corrosion resistance of alumina forming alloys against molten chlorides for energy production. II: Electrochemical impedance spectroscopy under thermal cycling conditions. Sol. Energy Mater. Sol. Cells 166, 234–245.

Goods, S.H., Bradshaw, R.W., 2004. Corrosion of stainless steels and carbon steel by molten mixtures of commercial nitrate salts. J. Mater. Eng. Perform. 13 (1), 78–87.

Goods, S.H., Bradshaw, R.W., Prairie, M.R., Chavez, J.M., 1994. Corrosion of stainless and carbon steels in molten mixtures of industrial nitrates. Sandia National Lab. (SNL-CA), Livermore, CA (United States), 37 p.

Grosu, Y., Bondarchuk, O., Faik, A., 2018. The effect of humidity, impurities and initial state on the corrosion of carbon and stainless steels in molten HitecXL salt for CSP application. Sol. Energy Mater. Sol. Cells 174, 34–41.

Heo, S.J., Hu, B., Uddin, M.A., Aphale, A., Hilmi, A., Yuh, C.-Y., Surendranath, A., Singh, P., 2017. Role of exposure atmospheres on particle coarsening and phase transformation of LiAlO2. J. Electrochem. Soc. 164 (8), H5086–H5092.

Ho, C.K., Carlson, M., Garg, P., Kumar, P., 2016. Technoeconomic analysis of alternative solarized s-CO2 brayton cycle configurations. J. Sol. Energy Eng. 138 (5).

Hofmeister, M., Klein, L., Miran, H., Rettig, R., Virtanen, S., Singer, R.F., 2015. Corrosion behaviour of stainless steels and a single crystal superalloy in a ternary LiCl–KCl–CsCl molten salt. Corros. Sci. 90, 46–53.

IEA, 2010. Technology Roadmap - Concentrating Solar Power, IEA, Paris https://www.iea.org/reports/technology-roadmap-concentrating-solar-power.

Kruizenga, A., Gill, D., 2014. Corrosion of iron stainless steels in molten nitrate salt. Energy Procedia 49, 878–887.

Li, C.-j., Li, P., Wang, K., Molina, E.E., 2014. Survey of Properties of Key Single and Mixture Halide Salts for Potential Application as High Temperature Heat Transfer Fluids for Concentrated Solar Thermal Power Systems. pp. 133-157.

Li, H., Yang, X., Yin, X., Wang, X., Tang, J., Gong, J., 2021. Effect of chloride impurity on corrosion kinetics of stainless steels in molten solar salt for CSP application: experiments and modeling. Oxid. Met. 95 (3–4), 311–332.

Liu, M., Steven Tay, N.H., Bell, S., Belusko, M., Jacob, R., Will, G., Saman, W., Bruno, F., 2016. Review on concentrating solar power plants and new developments in high temperature thermal energy storage technologies. Renewable and Sustainable Energy Reviews. Elsevier 1411–1432.

Mehos, M., Turchi, C., Vidal, J., Wagner, M., Ma, Z., Ho, C., Kolb, W., Andraka, C., Kruizenga, A., 2017. Concentrating Solar Power Gen3 Demonstration Roadmap. National Renewable Energy Lab. (NREL), Golden, CO (United States), 140 p.

Meißner, T.M., Oskay, C., Bonk, A., Grégoire, B., Donchev, A., Solimani, A., Galetz, M.C., 2021. Improving the corrosion resistance of ferritic-martensitic steels at 600 °C in molten solar salt via diffusion coatings. Solar Energy Materials and Solar Cells 227.

Ni, C.S., Lu, L.Y., Zeng, C.L., Niu, Y., 2011. Electrochemical impedance studies of the initial-stage corrosion of 310S stainless steel beneath thin film of molten (0.62Li,0.38K)2CO3 at 650°C. Corros. Sci. 53 (3), 1018–1024.

Palacios, A., Navarro, M.E., Jiang, Z., Avila, A., Qiao, G., Mura, E., Ding, Y., 2020. High-temperature corrosion behaviour of metal alloys in commercial molten salts. Sol. Energy 201, 437–452.

Phillips, W., Karmiol, Z., Chidambaram, D., 2019. Effect of Metallic Li on the Corrosion Behavior of Inconel 625 in Molten LiCl-Li 2 O-Li Journal of The Electrochemical Society. pp. C162-C168.

Prieto, C., Fereres, S., Ruiz-Cabañas, F.J., Rodriguez-Sanchez, A., Montero, C., 2020. Carbonate molten salt solar thermal pilot facility: plant design, commissioning and operation up to 700 °C. Renew. Energy 151, 528–541.

Ravi Shankar, A., Mathiya, S., Thyagarajan, K., Kamachi Mudali, U., 2010. Corrosion and microstructure correlation in molten LiCl-KCl medium. Metall. Mater. Trans. A 41 (7), 1815–1825.

Sah, S.P., Tada, E., Nishikata, A., 2018. Corrosion behaviour of austenitic stainless steels in carbonate melt at 923 K under controlled CO2-O2 environment. Corrosion Science. Elsevier Ltd 310–317.

Sarvghad, M., Steinberg, T.A., Will, G., 2017. Corrosion of steel alloys in eutectic NaCl+ Na2CO3 at 700 °C and Li2CO3 + K2CO3 + Na2CO3 at 450 °C for thermal energy storage. Sol. Energy Mater. Sol. Cells 170, 48–59.

Sarvghad, M., Delkasar Maher, S., Collard, D., Tassan, M., Will, G., Steinberg, T.A., 2018a. Materials compatibility for the next generation of Concentrated Solar Power plants. Energy Storage Mater. 179–198.

Sarvghad, M., Steinberg, T.A., Will, G., 2018b. Corrosion of stainless steel 316 in eutectic molten salts for thermal energy storage. Sol. Energy 198–203.

Selman, M.S.Y.a.J.R., 1999. Oxidation-lithiation of nickel, iron and cobalt in contact with molten carbonate. Solid State Ionics 124(1), 149–160.

Soleimani Dorcheh, A., Durham, R.N., Galetz, M.C., 2016. Corrosion behavior of stainless and low-chromium steels and IN625 in molten nitrate salts at 600 °C. Solar Energy Materials and Solar Cells. Elsevier 109–116.

Spiegel, M., Biedenkopf, P., Grabke, H.J., 1997. Corrosion of iron base alloys and high alloy steels in the Li2CO3-K2CO3 eutectic mixture. Corros. Sci. 39 (7), 1193–1210.

Steinmann, W.D., 2015. Thermal energy storage systems for concentrating solar power (CSP) technology. Adv. Therm. Energy Storage Syst. 511–531.

Tian, Y., Zhao, C.Y., 2013. A review of solar collectors and thermal energy storage in solar thermal applications. Appl. Energy 104, 538–553.

Tzvetkoff, T., Kolchakov, J., 2004. Mechanism of growth, composition and structure of oxide films formed on ferrous alloys in molten salt electrolytes—a review. Mater. Chem. Phys. 87 (1), 201–211.

Vignarooban, K., Xu, X., Arvay, A., Hsu, K., Kannan, A.M., 2015. Heat transfer fluids for concentrating solar power systems - a review. Applied Energy. Elsevier Ltd 383–396.

Walczak, M., Pineda, F., Fernández, Á.G., Mata-Torres, C., Escobar, R.A., 2018. Materials corrosion for thermal energy storage systems in concentrated solar power plants. Renew. Sustain. Energy Rev. 86, 22–44.

Wu, Y.-T., Ren, N., Wang, T., Ma, C.-F., 2011. Experimental study on optimized composition of mixed carbonate salt for sensible heat storage in solar thermal power plant. Sol. Energy 85 (9), 1957–1966.

Yamamoto, Y., Takeyama, M., Lu, Z.P., Liu, C.T., Evans, N.D., Maziasz, P.J., Brady, M.P., 2008. Alloying effects on creep and oxidation resistance of austenitic stainless steel alloys employing intermetallic precipitates. Intermetallics 16 (3), 453–462.

Yin, J.M., Zheng, Q.Y., Peng, Z.R., Zhang, X.R., 2019. Review of supercritical CO2 power cycles integrated with CSP. Int. J. Energy Res. 44 (3), 1337–1369.

Zhao, Y., Li, P., Jin, H., 2017. Heat transfer performance comparisons of supercritical carbon dioxide and NaCl–KCl–ZnCl2 Eutectic Salts for Solar s-CO2 Brayton Cycle. Energy Procedia 142, 680–687.

Paper I (b)

Additional data and experimental setups used for the study on alloys in contact to high temperature eutectic melts for thermal storage

E. Hamdy, J. N. Olovsjö, and C. Geers

Bibliography

E. Hamdy, J.N. Olovsjö, and C. Geers, "Additional data and experimental setups used for the study on alloys in contact to high temperature eutectic melts for thermal storage " 2021, Accepted.

Data in Brief 38 (2021) 107446

Contents lists available at ScienceDirect

Data in Brief

journal homepage: www.elsevier.com/locate/dib

Data Article

Additional data and experimental setups, for a comparative study of alloys in contact to eutectic melts for thermal storage

Esraa Hamdy[a,*], Johanna Nockert Olovsjö[b], Christine Geers[a]

[a] *Energy and Materials, Chalmers University of Technology, Gothenburg, Sweden*
[b] *Kanthal AB, Hallstahammar, Sweden*

ARTICLE INFO

Article history:
Received 8 July 2021
Revised 23 September 2021
Accepted 29 September 2021
Available online 4 October 2021

Keywords:
Experimental setups
Impurities
Reaction enthalpies
Post-exposure analyses
Alloy thickness loss
Phase stability

ABSTRACT

Three different eutectic salt mixtures have been brought into contact with three different high temperature alloys to assess corrosion damages for next-generation CSPs. This article contains additional material to support findings and assessments reported on our main article in the Solar Energy Journal [https://doi.org/10.1016/j.solener.2021.06.069]. Five sections, A-E, provide data to ensure reproducibility and confidence in our claims in the main article. A newly designed experimental setup for high temperature exposures is described as well as impurities within used chemicals. Material thickness measurements document alloy consumption by eutectic salts. Reaction enthalpies are listed illustrating individual metal species in contact with salt species at relevant temperatures. Thermodynamic single point equilibrium calculations have extended environmentally induced Laves phase precipitation found for alloy Kanthal APMT in contact with molten chlorides.

DOI of original article: 10.1016/j.solener.2021.06.069

* Corresponding author.
E-mail address: esraah@chalmers.se (E. Hamdy).

https://doi.org/10.1016/j.dib.2021.107446

Specifications Table

Subject	Materials Chemistry
Specific subject area	Experiments and analysis of high temperature alloys in contact with molten salts for thermal storage applications
Type of data	Table Image Graph Figure
How data were acquired	Chemical specifications by and impurity analysis by the suppliers Calibrated optical camera of the Phenom ProX table-top SEM setup to determine specimen thickness loss Software: Factsage 7.3 were used [1] Energy-dispersive X-ray spectroscopy (EDX) using a JEOL JSM-7800F Prime Software: Thermodynamic equilibrium calculation (Thermocalc Software, Database TCFE:Steels/Fe-Alloys v8.0 [2]
Data format	Raw sample thickness measurements Raw EDX measurement Input from Software Databases
Parameters for data collection	Alloy coupons were exposed at 650°C or 800°C, depending on the salt melt used and quenched after completion. All post-exposure analyses have been performed in ambient conditions using standard settings of the instruments listed for data acquisition. EDS point analyses were used as input for thermodynamical phase stability calculations of precipitates found in the alloy microstructures after exposure. Corrosion reaction enthalpies for relevant phases found by XRD and potential corrosion reactions were calculated by FactSage databases and software.
Description of data collection	This DIB manuscript contains additional information to support the findings shown in the Solar Energy article [DOI: 10.1016/j.solener.2021.06.069]. The data collection is basing on duplicates to ensure minimum reproducibility.
Data source location	Institution: Chalmers University of Technology City/Town/Region: Gothenburg Country: Sweden
Data accessibility	With the article
Related research article	E. Hamdy, J. N. Olovsjö, and C. Geers, "Perspectives on selected alloys in contact with eutectic melts for thermal storage: Nitrates, carbonates and chlorides," Solar Energy, vol. 224, pp. 1210-1221, 2021/08/01/ 2021, doi: https://doi.org/10.1016/j.solener.2021.06.069.

Value of the Data

- Experiments in molten salts are very sensitive for chemical impurities, melt loss due to evaporation, vessels and general setup qualities. Thus, a detailed description of our experimental conditions is essential to reach the necessary degree of reproducibility and applicability. Furthermore, we offer insight into our thermodynamic assessment routine on how to qualify our observations on environmentally introduced microstructural changes in our alloys.
- This additional data collection allows metallurgists, engineers and chemists working with thermal storage utilities to understand alloy consumption and microstructural changes in a more detailed way.
- This additional data complementing our main comparative study [DOI: https://doi.org/10.1016/j.solener.2021.06.069] shall provide guidance for alloy selections for thermal storage utilities utilising molten salts.
- Another interesting thought is using specific microstructural markers to assess the durability of an alloy in future plants by, e.g., electrochemical or ultrasonic online operation analysis. This data would, in this case, help significantly with the data interpretation and risk assessment.

1. Data Description

The additional data provided in this article is divided into five main sections; (A) sections provide detailed descriptions of the experimental procedure followed in our main study [3]. Section A1 gives the alloys preparation recipe that has been used. Table A1 and section A2 provide the reported chemical impurities of the employed salts in their respective datasheet. The chlorides purification process is thoroughly described in section A3. Section A4 comprehensively describes our newly built experimental setup of the corrosion and corrosion tests procedure. A5 summarises how the metallic samples are treated after exposure. Whereas section A6 describe different parameters and conditions used during the characterisation analysis.

Section (B) and Table B1 show the metal thickness changes of the exposed samples with a differential clarification between sample thickness, including oxide scales and the remaining metal thickness.

Section (C) gives an overview of Gibb's reaction enthalpies for metals (Al, Cr and Fe) reacting with respective alkali nitrate and alkali carbonate melts as investigated in the main article [3]. The output raw data files generated by Factsage 7.3 databases used to calculate Gibb's reaction enthalpies in Tables C1 and C2 are provided in the supplementary section.

Section (D) provides thermodynamic single-point calculations confirming the presence of Laves phase precipitates observed in Kanthal® APMT samples exposed to molten $MgCl_2$/KCl at 800 °C, cf the supplementary files for the raw output data calculated by Thermocalc Software, Database TCFE:Steels/Fe-Alloys v8.0.

Finally, section (E) gives a summarised technical features of alloy Kanthal® APMT.

2. Experimental Design, Materials and Methods

2.1. A1 - Alloy preparation

The procedure for sample preparation was as follows: metal coupons of initial measurements 15 × 15 × 2 mm were ground using up to 1200-grit SiC abrasive paper, followed by subsequent polishing with suspensions containing 9, 3, and 1 µm diamonds to a mirror-like finish. The polished samples underwent a three-step cleaning procedure with deionised water, acetone, and ethanol using an ultrasonic bath at room temperature. Afterwards, the coupons were dried using an air gun, then dipped into the salt mixture in alumina crucibles.

2.2. A2 - Salts chemical composition and impurities

Eutectic mixtures were prepared using the following salts: $NaNO_3$ (Alfa Aesar 99.0%), KNO_3 (Alfa Aesar 99.0%), Li_2CO_3 (VWR chemicals 99.0%), Na_2CO_3 (EMSURE anhydrous, 99.9%), K_2CO_3 (ThermoFisher Scientific 99.8%), KCl (Alfa Aesar 99.0%), $MgCl_2$ (Alfa Aesar anhydrous 99.0%). Suppliers provide the impurities concentrations in the salts. Table A1 summarises the impurities measured in the salts and has been reported in the salts' chemical datasheets.

2.3. A3 - Chlorides' purification process

The stepwise thermal purification process utilised in this work Ref. [main article] was based on previous studies [4–6]. The purification process conducted in this study followed these steps; (i) The chloride mixture was first dried at 100 °C for at least five hours. (ii) Afterwards, the temperature was increased to 200 °C and after a two-hour dwell time. (iii) The temperature was increased even further to 300°C and kept for another two hours. (iv) The setup was left to cool down to room temperature, then samples were dipped into the salt-containing crucible. (v)

Table A1
Impurities concentrations and chemical compositions of each salt

Salt	Moisture	Chloride (Cl^-)	Phosphate (PO_4^{3-})	Silicate (as SiO_2)	Total sulfur (as SO_4^{2-})	Calcium (Ca^{2+})	Magnesium (Mg^{2+})	Others
$NaNO_3$	detected	0.0006%	1.2 ppm	-	0.0020%	0.0008%	0.0005%	Heavy metals (e.g., $Pb^{2+/4+}$), $Fe^{2+/3+}$ 1 ppm for each
KNO_3	detected	0.002%	5 ppm	-	0.003%	0.005%	0.002%	Heavy metals 5 ppm, $Fe^{2+/3+}$ 3 ppm, IO_3^- 5 ppm, NO_2 0.001%, Na^+ 0.005%
Li_2CO_3	detected	≤0.02%	-	-	≤0.05%	0.01%		Heavy metals (e.g., $Pb^{2+/4+}$) ≤20 ppm, $Fe^{2+/3+}$ 3 ppm
Na_2CO_3	Loss on drying ≤1.0%	≤0.002%	≤0.001%	≤0.002%	≤0.005 %	≤0.005 %	≤0.0005%	Heavy metals (e.g., $Pb^{2+/4+}$), $Fe^{2+/3+}$, $N^{3-/3+/5+}$, Al^{3+}, K^+
K_2CO_3	0.113%	KCl 0.0043%	-	-	K_2SO_4 12 ppm	-	-	KOH 0.106%, Na^+ 0.20%, $Fe^{2+/3+}$ 0.40 ppm
KCl	detected	Chlorate & Nitrate ≤0.003 %	≤5 ppm		≤0.001%	≤0.002%	≤0.001%	Ba^{2+} ≥ 0.001%, Br^- ≤0.01%, I^- ≤0.002%, $Fe^{2+/3+}$ ≤3 ppm, Na^+ ≤0.005%, Heavy metals (e.g., $Pb^{2+/4+}$) ≤5 ppm
$MgCl_2$	Detected 0.97%	NaCl 36 ppm $CaCl_2$ 47 ppm	-	-	-	-	-	MgO (100 ppm)

Table B1
Change in metal thickness after being exposed to different salt melts.

	Conditions				
Sample thickness after exposure	Gas	Temperature (°C)	Total exposure time (h)	Salt Melts	Measured metal thickness change (µm)
316H 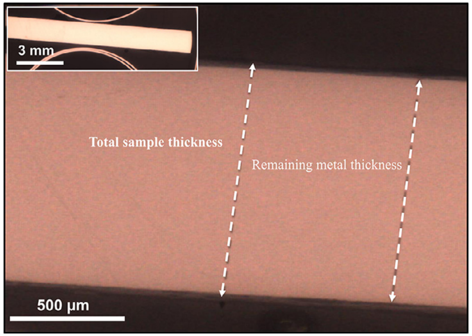 	Filtered air	650	1000 h	(60 wt% $NaNO_3$-40 wt% KNO_3)	Zero metal thickness loss
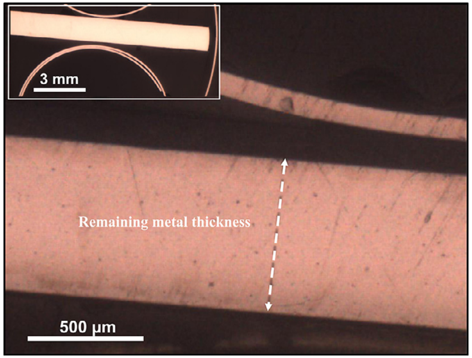 Kanthal® APMT					Zero metal thickness loss

(*continued on next page*)

Table B1 (*continued*)

	Conditions				
Sample thickness after exposure	Gas	Temperature (°C)	Total exposure time (h)	Salt Melts	Measured metal thickness change (µm)
304L 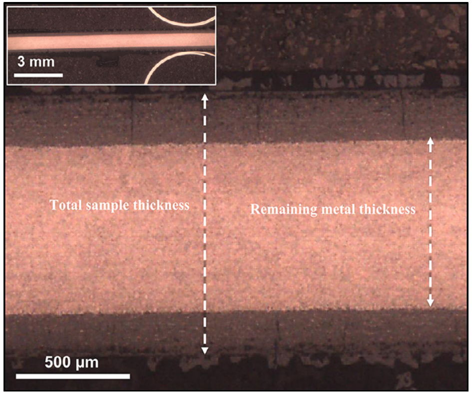	CO_2	800	1000 h	(32.1 wt% Li_2CO_3 -33.4 wt% Na_2CO_3-34.5 wt% K_2CO_3)	400 µm metal thickness loss
Kanthal® APMT 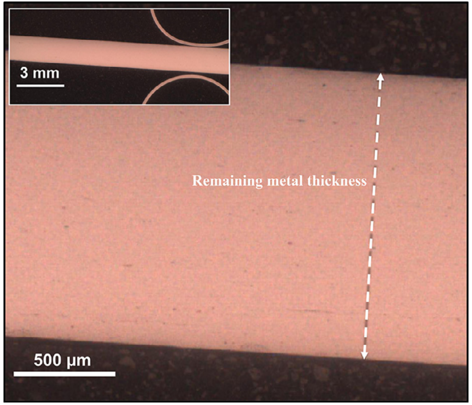					Zero metal thickness loss

(*continued on next page*)

Table B1 (*continued*)

	Conditions				
Sample thickness after exposure	Gas	Temperature (°C)	Total exposure time (h)	Salt Melts	Measured metal thickness change (µm)
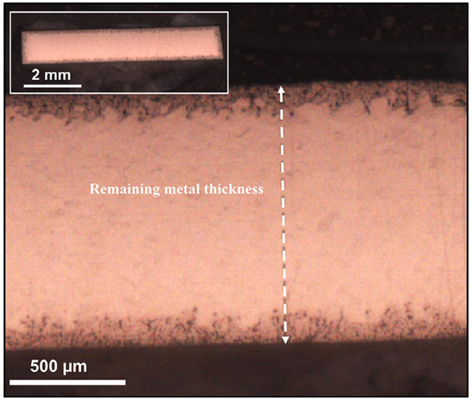 304L	Ar		500 h	(65 wt% KCl-35% wt% $MgCl_2$)	10–40 µm metal thickness loss
Kanthal® APMT 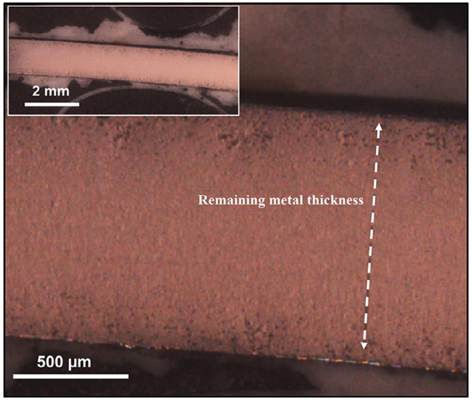					10 µm metal thickness loss

Table C1
Selected reaction energies between nitrates (650°C) and relevant alloy elements correlating with experimental observations. Databases from Factsage 7.3 were used [1].

No	Equation	ΔG_{923K}kJ /[mol metal]
Eq.1	$Al\ (s) + NaNO_3\ (l) \rightarrow NaAlO_2\ (s) + NO\ (g)$	−676
Eq.2	$Cr\ (s) + NaNO_3\ (l) \rightarrow NaCrO_2\ (s) + NO\ (g)$	−376
Eq.3	$Fe\ (s) + NaNO_3\ (l) \rightarrow NaFeO_2\ (s) + NO\ (g)$	−258
Eq.4	$8\ Al\ (s) + 3\ NaNO_3\ (l) \rightarrow 3\ NaAlO_2\ (s) + Al_2O_3\ (s) + 3\ AlN\ (s)$	−539
Eq.5	$8\ Cr\ (s) + 3\ NaNO_3\ (l) \rightarrow 3\ NaCrO_2\ (s) + Cr_2O_3\ (s) + 3\ CrN\ (s)$	−299
Eq.6	$23\ Fe\ (s) + 4\ NaNO_3\ (l) \rightarrow 4\ NaFeO_2\ (s) + Fe_3O_4\ (s) + 4\ Fe_4N\ (s)$	−88

Table C2
Selected reaction energies between carbonates (800°C) and relevant alloy elements correlating with experimental observations. Databases from Factsage 7.3 were used [1].

No	Equation	ΔG_{1073K}kJ /[mol metal]
Eq.7	$2\ Fe\ (s) + Na_2CO_3\ (l) + 2\ CO_2\ (g) \rightarrow 2\ NaFeO_2\ (s) + 3\ CO\ (g)$	+22
Eq.8	$2\ Fe\ (s) + Li_2CO_3\ (l) + 2\ CO_2\ (g) \rightarrow 2\ LiFeO_2\ (s) + 3\ CO\ (g)$	−7
Eq.9	$2\ Al\ (s) + Li_2CO_3\ (l) + 2\ CO_2\ (g) \rightarrow 2\ LiAlO_2\ (s) + 3\ CO\ (g)$	−414
Eq.10	$2\ Al\ (s) + Na_2CO_3\ (l) + 2\ CO_2\ (g) \rightarrow 2\ NaAlO_2\ (s) + 3\ CO\ (g)$	−393
Eq.11	$2\ Cr\ (s) + Na_2CO_3\ (l) + 2\ CO_2\ (g) \rightarrow 2\ NaCrO_2\ (s) + 3\ CO\ (g)$	−99
Eq.12	$69\ Cr\ (s) + 23\ Na_2CO_3\ (l) + 40\ CO_2\ (g) \rightarrow 46\ NaCrO_2\ (s) + Cr_{23}C_6\ (s) + 57\ CO\ (g)$	−70

Later, the vessels are purged with Ar for 12 h and heated up to 120 °C for at least 12 h. (vi) Finally, the temperature is raised to 750 °C and kept for one hour before starting the exposure at 800 °C.

2.4. A4 - Corrosion tests procedure and experimental setups

In this study, two setups were employed, a horizontal silica tube furnace and the Nabertherm setup. In this section, detailed corrosion tests procedure for each setup are provided.

(i) Horizontal tube furnace

This setup was used for partial immersion corrosion tests of alloys exposed to nitrates melt. After following the cleaning procedure of the alloy sample (coupon), the coupon is dipped into an alumina crucible filled with the salts' mixture. Before exposure and to prevent contamination, samples were purged in filtered air for at least five hours. After exposure, the salt was drained from the metal coupons using a heat gun. The heating gun method was done to avoid leaching corrosion products by washing the coupons with water. However, using a heat gun was not possible for samples exposed to carbonates and chlorides because of the significantly higher melting points of carbonates and chlorides than the nitrates melt, as shown in Table 2 in our main article [3]. The crucibles were limited in volume and had to be refilled with salt every 72 h, and the samples were only partially immersed in salt. Consequently, a new setup was built to address these limitations.

(ii) Vertical vessel setup

The second setup used for complete immersion experiments was a top-loader furnace (model top 60 Nabertherm). The Nabertherm furnace was purchased and redesigned in the workshop to comply with carbonate and chloride exposures in controlled gas environments. The furnace lid holds were designed to contain two cylindrical vessels, as shown in figure A. The inner diameter for each cylinder is 80 mm with 250 mm height, and they were constructed from stainless steel 253MA.

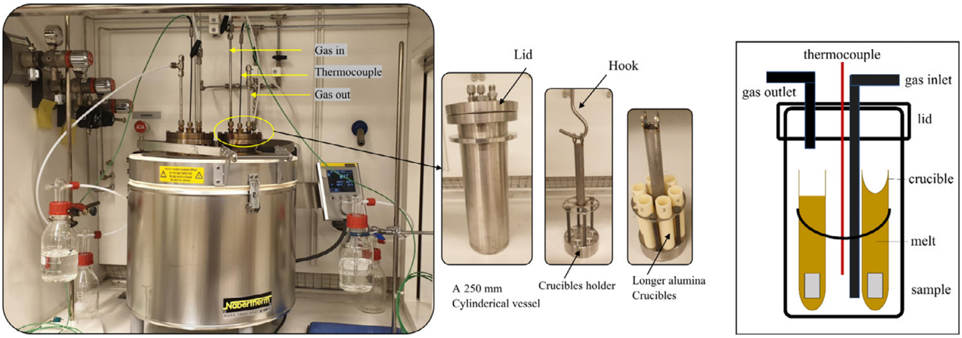

Fig. 1. (i) New laboratory setup built for the carbonate and chloride exposures (ii) cylindrical vessel components iii) schematic diagram of the cylindrical vessel.

Aluminium-diffusion coated using a powder pack cementation process has been applied to increase both vessels' durability [7]. The vessel's lid was designed to allow gas flow in and out of the vessel and mount a thermocouple for calibration. A 75 mm diameter sample holder was machined with slots to accommodate six alumina crucibles, as shown in Fig. 1. The purpose of designing two cylindrical vessels is to duplicate the number of samples that can be tested. Each cylindrical vessel enables investigating six samples/alloys under the same conditions.

Prior to exposure, the flow rate was calibrated with a Bios Definer 220M, and the gas line was extended through the vessel lid so that the gas could flow below the crucibles. The temperature was kept above 100 °C before exposure for at least five hours to ensure the absence of water vapour in the system. The system was purged for at least 5 h and 12 h for the carbonate and chloride exposures, respectively, to avoid contamination. CO_2 was utilised as the gas flow to suppress the decomposition of the carbonate melts. The coupons were placed vertically in alumina crucibles that had been filled with the salt mixture.

2.5. A5 - Sample post-exposure treatment

After exposure, alloy samples have been treated in two ways depending on the characterisation technique required. Since the vertical setup was designed to provide duplicate samples, one sample was washed with water, then weighed before and after the exposure using a SartoriusTM balance with microgram resolution. Instead of washing, the duplicate sample was left with a corrosive salt film on its surfaces after pouring off the residual melt. The procedure for the melts removal from the duplicate sample followed the upcoming steps: the temperature was lowered and maintained at 50 °C higher than the eutectic melting point for the mixture after the required exposure was completed. Holding the temperature at 50 °C higher than the eutectic melting point enabled us to pour off the salts while they were in their molten phase. Only a minor amount remained on the sample surfaces, and this salt was collected as well. The second cylindrical vessel provided a duplicate sample that was treated differently. The surface of the duplicate sample was rinsed with water to allow for mass change measurements. Each exposure was conducted twice.

According to the standard methods [8], the sample washing procedure was conducted: (i) Samples were sonicated for ten minutes at room temperature. (ii) After five minutes, sonication was interrupted. (iii) If there was salt remaining, the sample was gently brushed to remove the salts remaining, (iv) the sonication process was resumed to assure a complete dissolution of the salts. Results based on washed samples, e.g., XRD analysis and weight change values, require careful consideration. Weight change values have not been considered reliable data for corrosion evaluation, but only as an additional data point for the overall evaluation performance.

2.6. A6 - Characterisation techniques

Washed samples were weighed and characterised with scanning electron microscopy (SEM) and energy-dispersive X-ray spectroscopy (EDX) using a JEOL JSM-7800F Prime or Phenom ProX Desktop SEM equipped with an EDX detector. The electron beam was operated at an accelerating voltage of 15 kV, and collected EDX spectra. A Siemens D5000 powder diffractometer with grazing-incidence geometry was used for XRD surface analysis.

Unwashed samples were subjected to cross-section investigation. Cross-sections of the exposed samples were prepared by dry cutting with a low-speed diamond saw, followed by broad ion beam (BIB) milling with a Leica TIC 3X instrument. This device is equipped with three argon-ion guns for sputtering. The guns were operated at 8V, and the total sputtering time was seven hours. Before milling, the samples were sputter-coated with gold, and a thin polished silicon wafer was affixed to the surface to protect the oxide scale during milling.

2.7. B - Metal thickness changes

Table B1 summarises metal thickness changes to 316H, 304L, and Kanthal® APMT exposed to nitrate, carbonate, and chloride melts in this section. A calibrated optical camera of the Phenom ProX table-top SEM setup was employed to determine specimen thickness loss. It is essential to distinguish between the overall sample thickness, including oxide scales and the remaining metal thickness.

2.7.1. Nitrates

Alloy 316H and Kanthal® APMT exposed to 60 wt% $NaNO_3$- 40 wt% KNO_3 have not shown any loss in metal thickness; this agrees with their high corrosion resistance to the nitrate melts as reported in the main article's chapter 3.1.[3]

2.7.2. Carbonates

Despite the increase in total thickness of the 304L sample due to rapidly outward growing oxides, almost 400 µm of 304L metal thickness was lost. It is noteworthy that the remaining thickness of metallic components in 304L has been internally attacked and completely carburised, which alters the overall alloy chemistry. In comparison, Kanthal APMT thickness has not changed after being exposed to the carbonate melt.

2.7.3. Chlorides

The metal thickness loss in 304L and Kanthal APMT, corroded by the 65 wt% KCl- 35% wt% $MgCl_{2,}$ has been assigned to metallic elements leaching, and this could be observed as cavities in the bulk alloy. Unlike 304L exposed to carbonate melt, the cavities have not changed the chemistry of both alloys. Hence, the measured metal thickness for alloy 304L and Kanthal APMT included internally attacked zones comprising of MgO filled cavities. The metal thickness loss measured for 304L and Kanthal APMT was up to 10–40 µm and 10 µm, respectively.

2.8. C – Reaction enthalpies

Overview of Gibb's reaction enthalpies for metals (Al, Cr and Fe) reacting with sodium nitrate at 650 °C in Table C1 and an equivalent overview in Table C2 for metals reacting with carbonates in a CO_2 gas atmosphere at 800°C. The data has been normalised to per mol metal reacting with salt, which means that, e.g., the reaction enthalpy of Eq. (4) has been divided by 8. This provides direct comparability between all reactions. Factsage 7.3 databases were used to generate the data.

Table D1

Thermodynamic equilibrium calculation (Thermocalc Software, Database TCFE:Steels/Fe-Alloys v8.0[2]) for the suboxide scale composition indicated in Fig. 11 (b) in the main article [DOI: 10.1016/j.solener.2021.06.069] normalised to 1 mol. (a,b) Laves phase elemental composition and (c) sublattices occupation at equilibrium at 800°C. d) Theoretical temperature dependent equilibrium phase composition plot for EDX measured composition (a) normalised to 1 mol (Thermocalc Software package and database TCFE: Steels/Fe-Alloys v8.0). (Thermocalc Software, Database TCFE:Steels/Fe-Alloys v8.0 [2])

(a) Measured input values			(b) Elemental composistion of the Laves phase C14#1 Constituents of the Laves phase		
Element	Mole Fraction	Mass Fraction	Element	Mole Fraction	Mass Fraction
Mo	0.1	0.167	Mo	0.333	0.469
Al	0.03	0.014	Fe	0.484	0.396
Cr	0.25	0.227	Cr	0.170	0.130
Si	0.024	0.012	Si	0.013	0.006
Fe	0.596	0.580	Al	1.44E-06	5.7E-07

Output: Thermocalc single point calculation at 800°C:	
BCC	68 mass% (73.3 mol%)
Laves phase C14#1	32 mass% (26.7 mol%)

(c) Sublattice constitution for Laves phase C14#1 $(Al,Cr,Fe,Mo,Si)_2(Al,Cr,Fe,Mo,Si)$

Sublattice 1:		Sublattice 2:	
Constituent	Site Fraction	Constituent	Site Fraction
Fe	0.725	Mo	0.998
Cr	0.254	Cr	0.002
Si	0.020	Fe	3.10E-04
Mo	3.28E-04	Al	2.12E-06
Al	1.10E-06	Si	4.54E-08

(d) Temperature dependent phase composition plotted for EDX input values from (a).

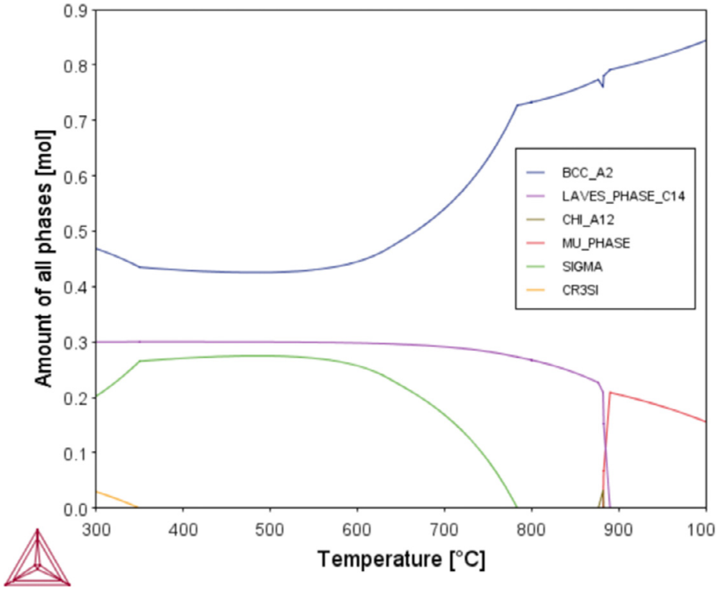

2.9. D – Thermodynamic single-point analysis of Laves phase precipitates

The exposure of a FeCrAl alloy, Kanthal® APMT, to molten $MgCl_2$/KCl presents with molybdenum rich precipitates in the suboxide region (Fig. 11b, [3]). EDS spot analyses on several precipitates were used to create input compositional data (Table D1a) for a Thermocalc single point equilibrium calculation [2]. The output file indicates a two-phase region consisting of 68 wt% BCC and 32 wt% Laves phase (A_2B). The major fraction of molybdenum constitutes the B-sublattice in the Laves phase forming approximately $(Fe_{0.75}Cr_{0.25})_2Mo$, see Table D1b,c).

Part d) in Table D1 shows a uni-axial equilibrium calculation which extends the single point calculation by the dimension of temperature. Laves phase is thermodynamically stable up to 900 °C. Interestingly, the formation of a ternary sigma phase is possible below 800 °C, reducing the fraction of the BCC phase but not Laves phase.

2.10. E – Description of alloy Kanthal® APMT

Kanthal® APMT is a powder metallurgically produced alumina forming ferritic stainless steel. The alloy is available in several product forms. Kanthal APMT has excellent oxidation properties in air and good stability at high temperatures. At lower temperatures (i.e., below 1000 °C), it is microstructurally stable. Some product might experience secondary recrystallisation at temperatures above 1000 °C. The high resistance of the alloy to oxidation and carburisation makes it useful in many demanding environments at elevated temperatures [9–11]. Kanthal APMT might not be cost-competitive with other conventional stainless steels, as its cost is roughly 20 times more expensive per kg than 304L and 316 alloys. Nevertheless, Kanthal APMT is considered a promising candidate for the next generation of CSP plants due to the following. (i) its high corrosion resistance in different molten salts compared to 304L and 316H alloys. (ii) the necessity to deviate from stainless steels due to unacceptable material loss and catastrophic failure risks.

Ethics Statement

Hereby, the authors assure that the manuscript adheres to Ethics in publishing standards.

CRediT Author Statement

Esraa Hamdy: Conducting exposure experiments, improving setup design, sample analyses, main author of this article; **Johanna Nockert Olovsjö:** Sample material advisor and main project partner for supplying Kanthal® APMT, prototype vessel production, co-authoring this article; **Christine Geers:** Conducting exposure experiments, improving setup design, sample analyses, thermodynamic calculations, co-authoring this article.

Declaration of Competing Interest

The authors declare that they have no known competing financial interests or personal relationships that could have appeared to influence the work reported in this paper.

Acknowledgments

This work was financially supported by Vinnova within the ALSTEr Project as part of the Jernkontoret initiative Metalliska Material. The Swedish Energy Agency continues to financially support our efforts within the thermal storage for SOLEL initiative under contract number 44653-1 (Jan-Erik Svensson) and as a partner in the High Temperature Corrosion Competence Centre (Lars-Gunnar Johansson).

Supplementary Materials

Supplementary material associated with this article can be found in the online version at doi:10.1016/j.dib.2021.107446.

References

[1] C.W. Bale, et al., Factsage thermochemical software and databases - recent developments, Calphad 33 (2009) 17.
[2] J.O. Andersson, et al., Thermo-calc and DICTRA, computational tools for materials science, Calphad 26 (2002) 273–312.
[3] E. Hamdy, J.N. Olovsjö, C. Geers, Perspectives on selected alloys in contact with eutectic melts for thermal storage: nitrates, carbonates and chlorides, Sol. Energy 224 (2021) 1210–1221.
[4] W. Phillips, Z. Karmiol, D. Chidambaram, Effect of metallic Li on the corrosion behavior of inconel 625 in molten LiCl-Li 2 O-Li, J. Electrochem. Soc. 166 (2019) C162–C168.
[5] J.C. Gomez-Vidal, et al., Corrosion resistance of alumina-forming alloys against molten chlorides for energy production. I: Pre-oxidation treatment and isothermal corrosion tests, Sol. Energy Mater. Sol. Cells 166 (2017) 222–233.
[6] W. Ding, T. Bauer, Progress in research and development of molten chloride salt technology for next generation concentrated solar power plants, Engineering 7 (3) (2021) 334–347.
[7] C. Oskay, et al., Scale formation and degradation of diffusion coatings deposited on 9% Cr steel in molten solar salt, Coatings 9(10) (2019) 687.
[8] ASTM G1-03(2017)e1, Standard Practice for Preparing, Cleaning, and Evaluating Corrosion Test Specimens, ASTM International, West Conshohocken, PA, 2017.
[9] M. Sarvghad, et al., Materials compatibility for the next generation of concentrated solar power plants, Energy Storage Mater. 14 (2018) 179–198.
[10] B. Jönsson, et al., High temperature properties of a new powder metallurgical FeCrAl alloy, Mater. Sci. Forum 461-464 (2004) 455–462.
[11] P. Steinmetz, I. G. Wright, G. Meier, A. Galerie, B. Pieraggi, R. Podor, High Temperature Corrosion and Protection of Materials 6, Illustrated, Trans Tech Publications Ltd, Zurich, Switzerland, 2004.

Paper II

Differentiation in corrosion performance of alumina forming alloys in alkali carbonate melts

E. Hamdy, M. Strach, J. N. Olovsjö, and C. Geers

Bibliography

E. Hamdy, M. Strach, J. N. Olovsjö, and C. Geers, "Differentiation in corrosion performance of alumina forming alloys in alkali carbonate melts," Corrosion Science, p. 109857, 2021/09/20/ 2021, doi: https://doi.org/10.1016/j.corsci.2021.109857.

Corrosion Science 192 (2021) 109857

Contents lists available at ScienceDirect

Corrosion Science

journal homepage: www.elsevier.com/locate/corsci

Differentiation in corrosion performance of alumina forming alloys in alkali carbonate melts

Esraa Hamdy [a,*], Michal Strach [b], Johanna Nockert Olovsjö [c], Christine Geers [a]

[a] *Energy and Materials, Chemistry and Chemical Engineering, Chalmers University of Technology, Gothenburg, Sweden*
[b] *Chalmers Materials Analysis Laboratory, Physics, Chalmers University of Technology, Gothenburg, Sweden*
[c] *Kanthal AB, Hallstahammar, Sweden*

ARTICLE INFO

Keywords:
Lithium aluminate
Alumina forming alloys
Molten carbonates
High temperature corrosion
Phase transition

ABSTRACT

Alkali carbonate melts are promising high temperature thermal storage media. In this work five alumina forming alloys have been exposed to a ternary LiNaK carbonate melt and CO_2 at 800 °C. The corrosion propagation was found to depend on the formation of a slow-growing $LiAlO_2$ scale. Furthermore, the two polymorphs contributing to the $LiAlO_2$ phase were monitored for up to 1000 h: a dense α-$LiAlO_2$ scale and γ-$LiAlO_2$ crystallites. We suggest a growth stress assisted formation of α-$LiAlO_2$ relaxing into the outwards growing γ-$LiAlO_2$ phase. This implies a deceleration of the α-$LiAlO_2$ scale growth towards a steady state-thickness.

1. Introduction

New generations of climate-neutral energy technologies, such as concentrated solar power (CSP) with thermal storage capacities, surpass current temperature limitations by utilising high temperature heat transport and storage media with superior thermal stability [1–5]. While reaching for increased energy conversion efficiency and grid stability, material challenges due to high temperature corrosion risks lack data on long-term performance, especially when it comes to selected molten salt mixtures in contact with metal components. These eutectic melts comprise commonly ternary alkali carbonates or binary chloride mixtures. The first pilot plant operating with ternary carbonates comprising lithium-, sodium, and potassium carbonates (LiNaK) operates at 700 °C [1].

Metal components are made of high temperature resistant alloys providing structural strength as well as containment of the salt, while growing a passivating oxide scale at the surface, preventing corrosion by molten species. Formation and slow growth of a passivating oxide scale are crucial for alloy components' overall performance and, subsequently, the entire power plant. Chromium oxide on stainless steels and aluminium oxide on ferritic alumina forming alloys are common candidates to establish a high temperature corrosion protection in next-generation thermal storages utilising alkali carbonates at 700 °C or higher. However, a chromium oxide scale has proven insufficient to protect an alloy against internal oxidation and rapid carburisation, causing material embrittlement [6,7]. On the other hand, studies on alumina forming alloys showed that slow-growing alkali aluminate scales do not permeate carbon [8,9]. In this aspect, alumina forming alloys are superior to all chromia forming steels. In a previous study [7], we report specifically on the time-resolved performance of the alumina forming Kanthal® APMT at 800 °C immersed in LiNaK carbonates. Lithium ions have shown to be the predominant alkali species incorporated into oxides growing on high-temperature alloys [7,10,11]. After 72 h, the surface was covered by an α-lithium aluminate layer. After a few hundred hours, larger crystallites have been observed and identified as γ-lithium aluminate.

In the spirit of identifying the higher temperature operation limit, this research was conducted at 800 °C.

The solid-state synthesis of $LiAlO_2$ and characterisation of its two polymorphs α and γ has been published by Lehmann and Hasselbarth in 1961. In air, the low-temperature modification, α-$LiAlO_2$, transforms into γ-$LiAlO_2$ at 600 °C or higher [12]. In several studies, reacting lithium carbonate with alumina powder in different environments revealed that the upper-temperature limit for α-$LiAlO_2$ formation is in the range of 747–777 °C [13–16].

Evans et al. introduced in 1978 a concept for the stress assisted formation of a duplex oxide scale comprising two polymorphs, i.e., tetragonal and monoclinic zirconia on zircaloy-2 [17]. In the present study, the same concept is adopted to express the growth of both α- and γ-$LiAlO_2$ at 800 °C. In Evans's case, a stress stabilised tetragonal zirconia

---

* Corresponding author.
E-mail address: esraah@chalmers.se (E. Hamdy).

https://doi.org/10.1016/j.corsci.2021.109857
Received 19 July 2021; Received in revised form 13 September 2021; Accepted 14 September 2021
Available online 20 September 2021

morphology forms at the metal/oxide interface under compressive stress until relaxing into a monoclinic lattice. The magnitude of the compressive stress allows tetragonal ZrO_2 to form at a significantly lower temperature than its ambient pressure phase transition point, as indicated in the T-P-phase diagram [18]. Detailed investigations are still regularly published to understand and predict a limiting scale thickness [19,20], also referred to as steady-state thickness, due to its technological importance for nuclear applications [19]. Evans et al. emphasised in 1978 that the concept of a stress stabilised inner oxide scale is universal under the condition of two possible polymorphs. We believe that the α- to γ-$LiAlO_2$ transformation is one of these examples, which leads to the assumption of a limiting steady-state thickness of the α-$LiAlO_2$ inner oxide layer.

It should be mentioned that the density of γ-$LiAlO_2$ is 25% lower compared to α-$LiAlO_2$. The crystal structure visualisation in Fig. 1 [21, 22] highlights the layered packing of lithium and aluminium ion polyhedrons along the c-axis for α-$LiAlO_2$, while γ-$LiAlO_2$ comprises alternating Li/Al tetrahedrons [22].

In this study, the corrosion processes on the alumina forming alloys Kanthal® APMT, Kanthal® AF, Nikrothal® PM58, and two newly developed alloys, Fe10Cr4Al base, in LiNaK carbonate melt at 800 °C will be described.

2. Experimental

Specimens of five alumina forming alloys have been prepared and investigated in this study. The alloys have relatively similar aluminium content. The nominal compositions of Kanthal® AF and Kanthal® APMT are almost identical, Fe20Cr5Al however, the latter differs in Mo and Mn content (Table 1.).

The newly developed Kanthal® EF100 and 101, Fe10Cr4Al, differ in Si content. Nikrothal® PM58 is an alumina-forming austenitic alloy.

A salt mixture of 32.1 wt% Li_2CO_3, 33.4 wt% Na_2CO_3 and - 34.5 wt% K_2CO_3 was prepared and have been purchased from VWR chemicals (99.0%), EMSURE anhydrous (99.9%), and ThermoFisher Scientific (99.8%), respectively.

The salt preparation method, chemical composition and concentration of each salt impurities are stated in [23]. A unique setup was built to provide a full immersion of coupons into the salt melt during exposures. A detailed description of the setup built is given in a previous publication [23]. The isothermal exposures were conducted at 800 ± 5 °C under flowing CO_2. Upon each experiment, two duplicate samples are produced and are differently treated, as will be discussed further, depending on the characterisation technique. Each exposure was repeated at least two times for each material.

Metal coupons of initial measurements 15 × 15 × 2 mm were prepared to a mirror-like finish (1 μm diamond polish). The polished samples were thoroughly cleaned and dried, then immersed in the prepared salt mixture. Detailed procedure of metal coupons preparation is provided in a former publication [23].

2.1. Post-exposure surface analysis

After exposure, samples were differently treated based on the type of investigations required. For example, samples subjected to surface investigations, X-ray diffraction (XRD) analysis, and mass change measurements have been rinsed with water by an ultrasonic cleaner at room temperature, see [23]. After weighing the washed samples, surface investigations were conducted by scanning electron microscopy (SEM) and energy-dispersive X-ray spectroscopy (EDX) using a JEOL JSM-7800F Prime or Phenom ProX Desktop SEM with an EDX detector. The Siemens D5000 powder diffractometer equipped with a Cu source, a secondary Si monochromator, and a point detector with grazing-incidence geometry was used for XRD surface analysis. Li containing species were exclusively detectable through XRD.

Rietveld refinement on the acquired XRD patterns was performed using the TOPAS V6 software. Rietveld refinement on the phases included zero-error corrections, polarisation factor, a fundamental parameters approach for instrumental profile simulation, preferred orientation correction based on spherical harmonics, corresponding emission profile, and polynomial simulated background. The structures used in the refinement were trigonal R-3 M for the α-$LiAlO_2$ phase, tetragonal P41212 for the γ-$LiAlO_2$ phase, and cubic Im-3 m for the FeCrAl substrate phase.

It has to be noted that the applied model does not include absorption effects in the layered structure. Signal from the inner oxide layer will be decreased by the growing outer scale, affecting the measured peak intensities. In addition, the penetration depth in the used grazing incidence geometry cannot be determined without exact incidence angle values and densities (packing) of the probed layers. Hence, the obtained phase fractions provide only qualitative insights and require additional parameters obtained by microscopic inspection of cross-sections.

2.2. Post-exposure cross-section analysis

For cross-sectional investigations, samples were not rinsed. After pouring out the melt, a thin salt film stays on the top of the sample. Cross-sections of the exposed samples were prepared via dry cutting with a low-speed diamond saw, followed by broad ion beam (BIB) milling with a Leica TIC 3X instrument.

3. Results

In this section, the corrosion behaviour of the selected alumina forming alloys will be discussed based on mass change measurements, XRD and Rietveld analysis, and microscopic investigations (surface morphology and cross-sectional analysis).

3.1. Mass change measurements of alumina forming alloys exposed to alkali carbonate melts

Corrosion performance is evaluated quantitatively by measuring the

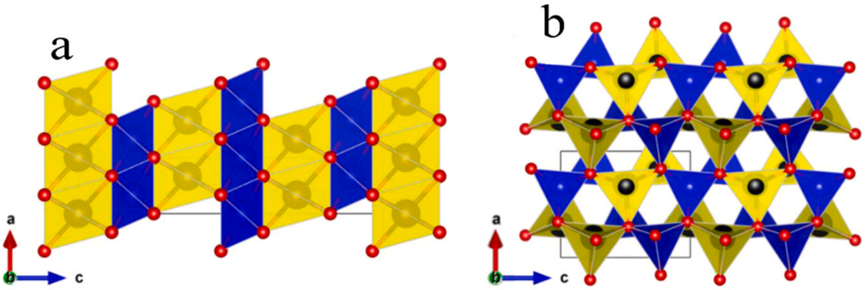

Fig. 1. Three-dimensional polyhedral visualisation of a) α-$LiAlO_2$ and b) γ-$LiAlO_2$ crystal structures, where red, yellow and blue spheres represent oxygen, lithium and aluminium atoms [21,22].

Table 1
Nominal alloy compositions.

Alloy	Fe	Ni	Cr	Al	Si	Mn	Mo	Others
Kanthal®APMT	balance	X	21	5	0.7	0.4	3	RE; C 0.08
Kanthal® AF	balance	X	21	5.3	0.7	X	X	RE; C 0.08
Kanthal® EF101	balance	< 0.5	11–14	3.2–4.2	1.2	< 0.7	X	RE; C 0.08
Kanthal® EF100	balance	< 0.5	9.5–13	3.8–4.2	< 0.5	< 0.7	X	RE; C 0.08
Nikrothal® PM58	18	Balance	19	5	0.4	X	X	RE

mass change of the samples after being rinsed with water [23]. Due to the rinsing procedure, the soluble oxide species are dissolved; therefore, the mass change values must be interpreted cautiously. $LiAlO_2$ was not found to dissolve by this procedure. Nevertheless, the mass change plot, besides other analyses, can give an indication on the scale formation and growth kinetics. As shown in Fig. 2, all alumina forming alloys have shown relatively similar mass gain values. After 72 h, the mass gain obtained shows that Kanthal® EF 101 has the lowest mass gain, followed by Kanthal® APMT and Kanthal® AF, which have relatively similar mass change values; Nikrothal® PM58 has the highest mass gain, while the Kanthal® EF 100 has shown a mass loss.

The mass change data will be used in Table 2. to estimate α/γ-$LiAlO_2$ phase transformation ratios, in comparison to the Rietveld data.

3.2. "Normal" formation and transformation of $LiAlO_2$

In this study, the selected alloys will be categorised into two groups based on their formation and transformation behaviour of $LiAlO_2$: i) "normal" and ii) "deviating". The “normal” formation and transformation of $LiAlO_2$ is incorporating no ternary cationic species from the alloy and is therefore chemically very similar to the synthesis products already described by Lehmann and Hasselbarth [12]. The “deviating” behaviour described in the next chapter involves at least one more metal ion in the scale formation. Fig. 3. shows the XRD patterns of the Kanthal® EF 101 after exposure to alkali carbonate melts at 800 °C. After short-term exposure (72 h and 168 h), only one phase of $LiAlO_2$ has been identified, i.e. α-$LiAlO_2$. After longer exposures (500 h and 1000 h), another lithium aluminate phase, γ-$LiAlO_2$ emerged. These findings are similar for Kanthal® APMT and Kanthal® AF. In Table 2. the α/γ $LiAlO_2$ phase ratios are quantified by Rietveld analysis.

Fig. 4. displays the relatively similar surface morphology of Kanthal® APMT, Kanthal® AF, and Kanthal® EF 101. After short-term exposure (72/168 h), small crystals, identified as α-$LiAlO_2$, completely covered the surface. After longer exposure times (500 h/1000 h), the larger γ-$LiAlO_2$ phase started to emerge.

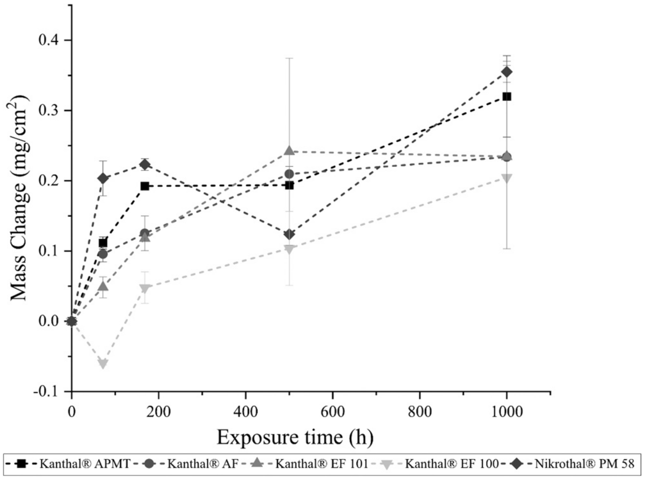

Fig. 2. Overall mass change behaviour of the selected alumina forming alloys immersed in alkali carbonate at 800 °C after different exposure times.

Fig. 5 shows an example of the characteristic double-layer structure composed of a compact inner α- $LiAlO_2$ scale and outer γ-$LiAlO_2$ crystals, on Kanthal® EF 101. The average scale thicknesses of the "normal" behaving $LiAlO_2$ forming alloys have been measured and tabulated in Table 2. Kanthal® APMT shows the thickest α-$LiAlO_2$ scale among the "normal" behaving alloys.

The measured mass gain, $\Delta m_{(measured)}$, for the "normal" $LiAlO_2$ formers represents the uptake of lithium and oxygen into the scale. The amount of substance (n) for $LiAlO_2$ is obtained by correcting the measured mass gain for the aluminium contribution from the alloy (41% of the molar mass M_{LiAlO2}) divided by the total M_{LiAlO2}, Eq. 1. The α-$LiAlO_2$ phase in the "normal" scenario forms a rather homogeneous scale at the surface with a mean thickness X(α). The mean thickness X(α) derived from cross-sectional analyses multiplied by sample area and theoretical density of α-$LiAlO_2$ from the crystallographic database [22] allows us to determine an approximate total mass of α-$LiAlO_2$ and consequently an amount of substance, n(α).

$$n(LiAlO_2\ total) = n(\alpha) + n(\gamma) = \frac{\Delta m(measured)\cdot 1.69}{M(LiAlO_2)} \qquad (1)$$

For each sample of the "normal" $LiAlO_2$ formers, the α/γ-phase ratio was determined using Eq. 1, combining gravimetry and microscopy. Rietveld refinement for each powder diffractogram has been used as an alternative quantification of α/γ-$LiAlO_2$ ratios for comparison.

The α/γ phase ratios derived by Rietveld refinement contain information on the increasing coverage of the sample surfaces by γ- $LiAlO_2$. The ratios determined by combined microscopy and gravimetric measurements allow for a quantification of the α- $LiAlO_2$ scale contribution to the total mass gain. All values are tabulated in Table 2. It is noteworthy that the mass gain and scale thickness used in the calculations are for two different coupons. However, they have been exposed simultaneously under the same conditions.

Plotting scale thicknesses and the α/γ-phase ratio (Rietveld) in Fig. 6. reveals the growth of α- and γ-$LiAlO_2$ phase over time. It is noteworthy to point out that the α/γ ratios derived by Rietveld analysis plotted in Fig. 6 seem to indicate a deceleration or even reducing γ-$LiAlO_2$ fraction after 500 h for Kanthal APMT and Kanthal EF101, while the average thickness is steadily increasing. The top view images in Fig. 4. show that the individual γ-$LiAlO_2$ crystals grow significantly with time but the overall number of nucleation sites does not increase. This can have an effect on the Rietveld phase fraction slope in Fig. 6. The rapid increase of size and phase fraction of γ-$LiAlO_2$ may lead to Al depletion in the bulk alloy. Thus, line scan analysis has been performed on all 1000 h exposure samples and did not substantiate that concern (Fig. 5.d). The α-$LiAlO_2$ scale growth decelerates over time.

Summarising the observations for the "normally" behaving $LiAlO_2$ forming alloys, minor deviations can be found for each parameter, i.e., as surface roughness, crystals size and scale thickness.

3.3. "Deviating" formation and transformation of $LiAlO_2$

The corrosion behaviour of the Kanthal® EF 100 and Nikrothal® PM 58 deviates from the "normal" α- $LiAlO_2$ forming alloys, particularly after short-term exposures. In the case of Kanthal® EF 100, the alloy surface was completely covered with $LiFeO_2$ crystals after 72 h, as shown in Fig. 7.c and confirmed with XRD, Fig. 8. After 168 h, however, all traces

Table 2
Mean scale thicknesses (X) for α- and γ-$LiAlO_2$, mass change Δm, gravimetrically and microscopically derived α/γ-phase ratio (calc. Eq. 1) and Rietveld derived phase ratios (α to γ % Rietveld). The n.a. (not available) error data in the table is attributable to duplicate sample loss in the repeated experiment due to alumina crucible breakdown during cooling.

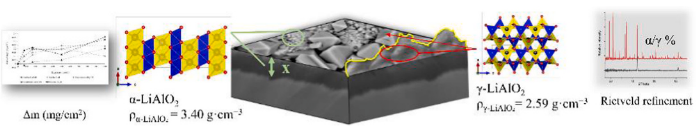

Exposure Time		Δm (mg/cm^2)	$X_{measured}$ (μm)	α to γ % calc.	α to γ % Rietveld
Kanthal® APMT					
72 h	α	0.11±0.008	0.30 (Max 0.6)	97.33	100
	γ		-	2.67	0
168 h	α	0.19±n.a	0.75 (Max 2.4)	77.05	100
	γ		-	22.95	0
500 h	α	0.19±0.002	0.95 (Max 3.2)	96.40	63.9 ± 0.9
	γ		1.60 (Max 2.3)	3.60	36.1± 0.9
1000 h	α	0.32±0.06	1.80 (Max 3.2)	93.67	78.1 ± 1.1
	γ		5.2 (Max 8.8)	6.33	21.9± 1.1
Kanthal® AF					
72 h	α	0.10±0.01	0.45 (Max 0.7)	93.79	100
	γ		-	6.21	0
168 h	α	0.13±0.02	0.5 (Max 0.7)	65.93	85.5±2.5
	γ		0.42 (Max 0.6)	34.07	14.5±1.9
500 h	α	0.21±0.01	0.6 (Max 0.7)	47.96	70±1
	γ		0.85 (Max 4.4)	52.04	30±1
1000 h	α	0.23±0.13	1.13 (Max 1.8)	33.59	9.8±2.5
	γ		3.0 (Max4.3)	66.41	90.2±2.4
Kanthal® EF 101					
72 h	α	0.05±0.01	0.45 (Max 1.2)		100
	γ		-		0
168 h	α	0.12±n.a	0.47 (Max 0.6)	75.84	64±0.9
	γ		0.75 (Max 1.25)	24.16	36±0.9
500 h	α	0.24±0.13	0.52 (Max 0.7)	27.13	18±5
	γ		1.4 (Max 2.7)	72.87	82±5
1000 h	α	0.23±n.a	0.6 (Max 1.1)	51.06	20.2±3.8
	γ		1.7 (Max 3.5)	48.94	79.8±3.3

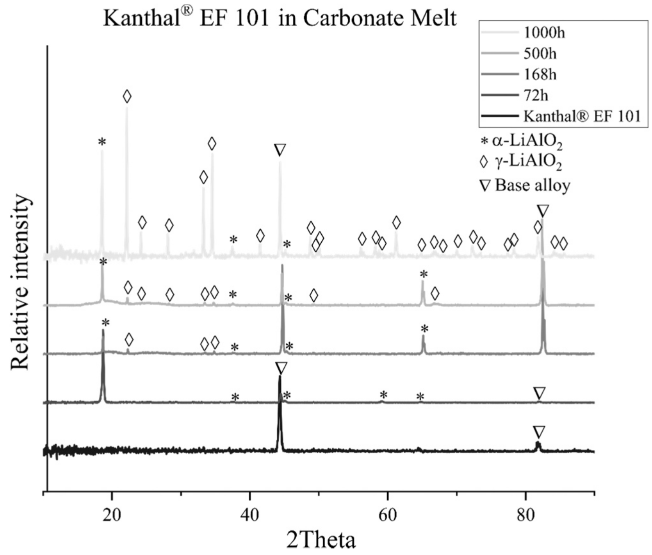

Fig. 3. XRD patterns of Kanthal® EF 101 after exposure to alkali carbonates in CO_2 at 800 °C for 72 h,168 h, 500 h and 1000 h.

of $LiFeO_2$ have disappeared due to dissolution into the carbonate melt (Fig. 7d and g). This observation is in agreement with the observed mass loss, cf. Fig. 2. Instead, small crystals of α-$LiAlO_2$ are formed. Furthermore, after longer exposure times (500 h/1000 h), γ-$LiAlO_2$ crystals started to grow similarly to the "normally" behaving alloys. Due to the initial mass loss induced by the transient α-$LiFeO_2$, the coupled gravimetric/microscopic determination of the α/γ-$LiAlO_2$ phase ratio via Eq. 1 was not applicable here. However, α/γ-$LiAlO_2$ phase ratios have been obtained by Rietveld refinement of the XRD patterns obtained after 168 h, 500 h and 1000 h exposures. The Rietveld data and mean scale thicknesses are shown for comparison in Fig. 6. Indeed, the slow growth of the thin α-$LiAlO_2$ scale and scarce nucleation of γ-$LiAlO_2$ crystallites at the surface lead us to classify Kanthal® EF 100 as one of the "normally" behaving $LiAlO_2$ forming alloys after overcoming a deviating early stage.

At 800 °C the austenitic alloy Nikrothal® PM58 forms $Li(Cr,Al)O_2$ in contrast to the protective α-$LiAlO_2$ scale that has been reported for exposures at 750 °C [24]. Fig. 9. shows XRD and microscopic analysis results of Nikrothal® PM58 after exposure to alkali carbonate melts for at least 1000 h. Cross-section and EDX analyses revealed that Nikrothal® PM58 developed pegs in the suboxide zone filled with mainly $Li(Cr,Al)O_2$ and some fractions of aluminium enriched scale as well as nickel and iron-rich particles. In Fig. 9.c–e, point analysis on the surface reveal that Fe and Ni particles have been transported to the oxide/melt interface

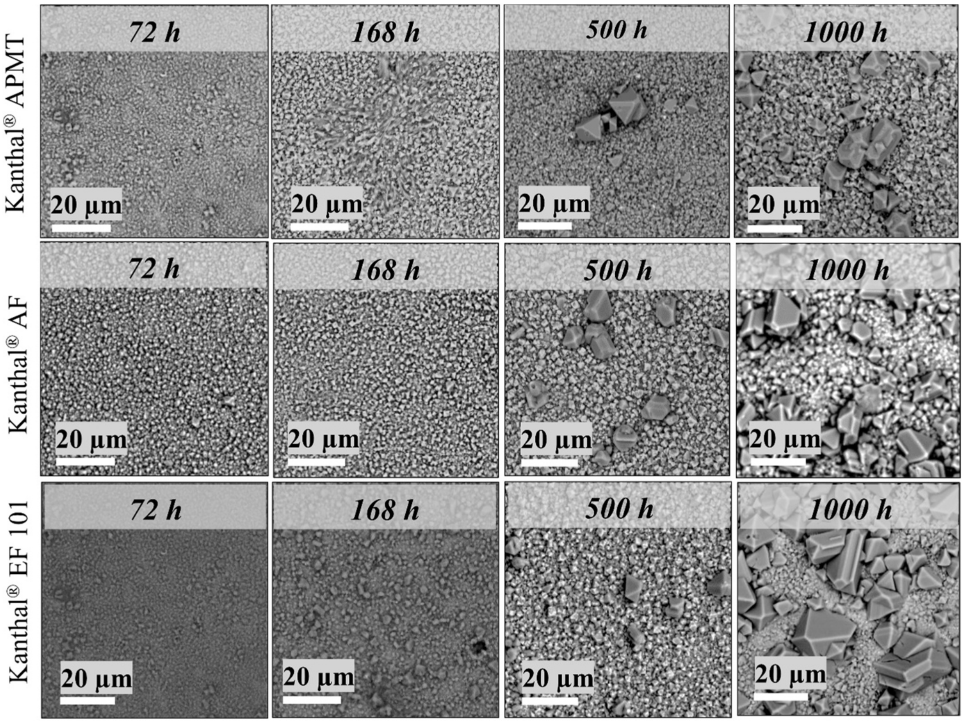

Fig. 4. Top view electron microscopic images for "normal behaving alloys" only $LiAlO_2$ species exposed to carbonate melts at 800 °C after different exposure times. Larger crystals present γ- $LiAlO_2$, small crystals are attributed to α- $LiAlO_2$.

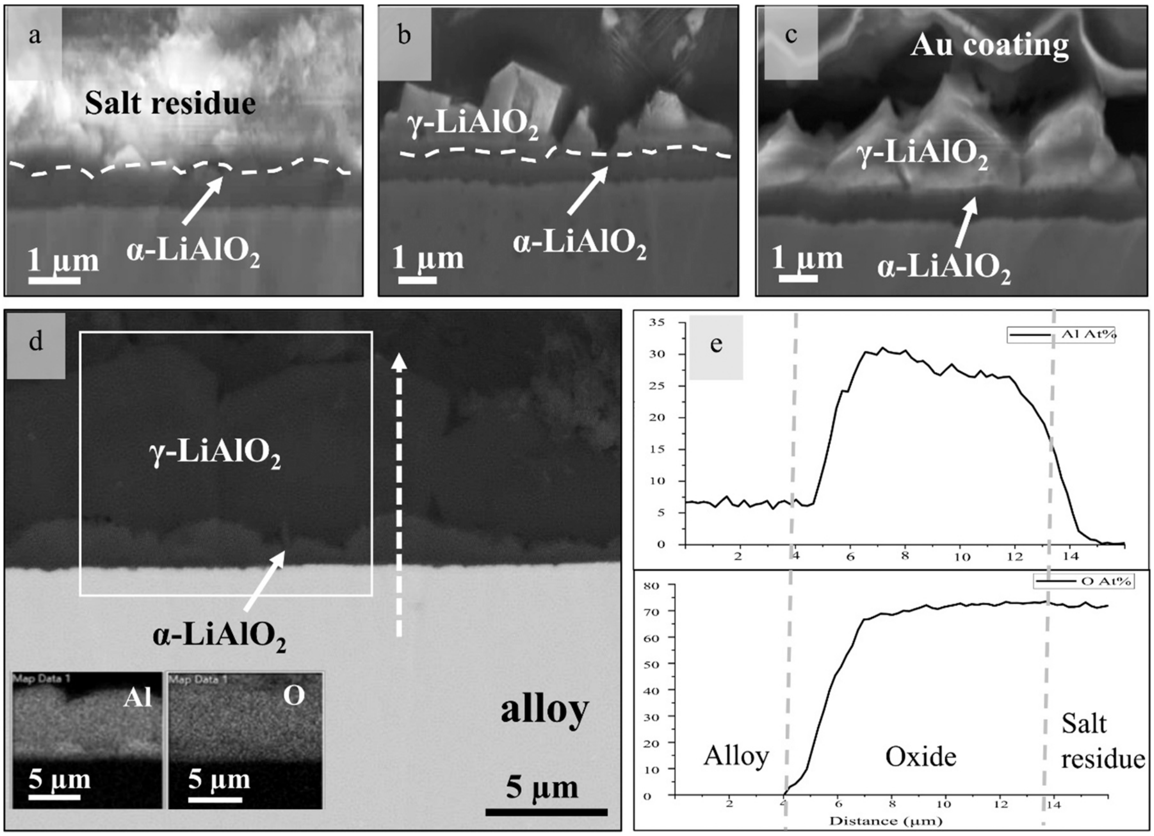

Fig. 5. Cross-section of Kanthal® EF 101 immersed in LiNaK carbonate at 800 °C after a) 72 h, b) 168 h, c) 500 h and d) 1000 h and EDS mapping of Al and oxygen through crystals, e) line scans of Al and oxygen through crystals and in the bulk alloy.

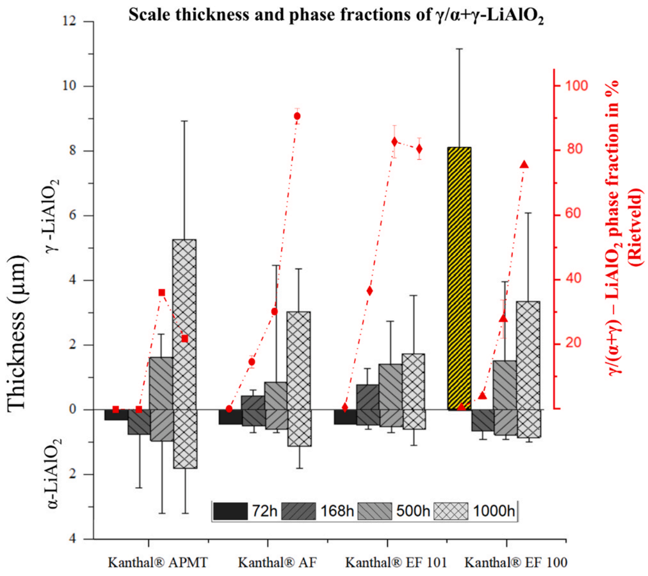

Fig. 6. Thickness values for α- and γ-$LiAlO_2$ of the four ferritic FeCrAl alloys and the corresponding results of Rietveld analysis, Column in yellow represents $LiFeO_2$ cf. Section 3.3.

and can easily leach into the alkali carbonate melt. An aluminium depletion zone in the suboxide region has been detected, reaching roughly 14 µm into the alloy. Just beneath the oxide, the aluminium content was lowered by 1.2 wt% compared to the nominal composition (see Fig. 9.f).

4. Discussion

From the experimental results, two fundamental oxidation behaviours of alumina formers in alkali carbonate melts can be distinguished. One we call the "normal" lithium aluminate formation with an initially forming inner α-$LiAlO_2$ and an outer γ-$LiAlO_2$ phase. No other cationic

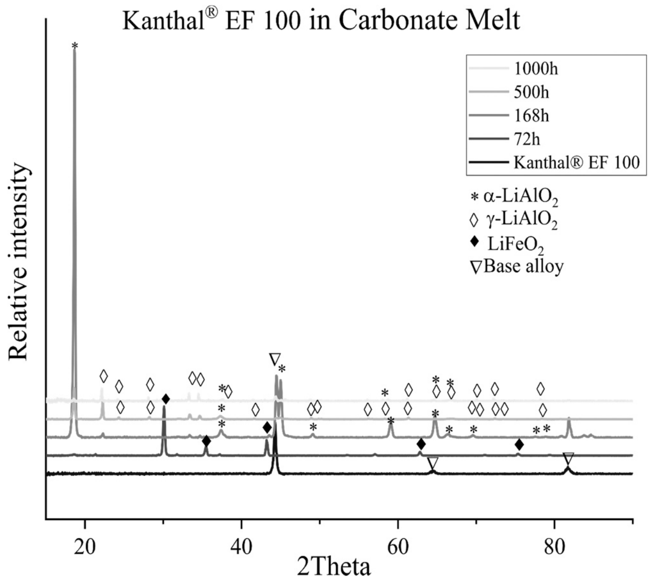

Fig. 8. XRD patterns for Kanthal® EF 100 after exposure to alkali carbonates in CO_2 at 800 °C for 72 h,168 h, 500 h and 1000 h.

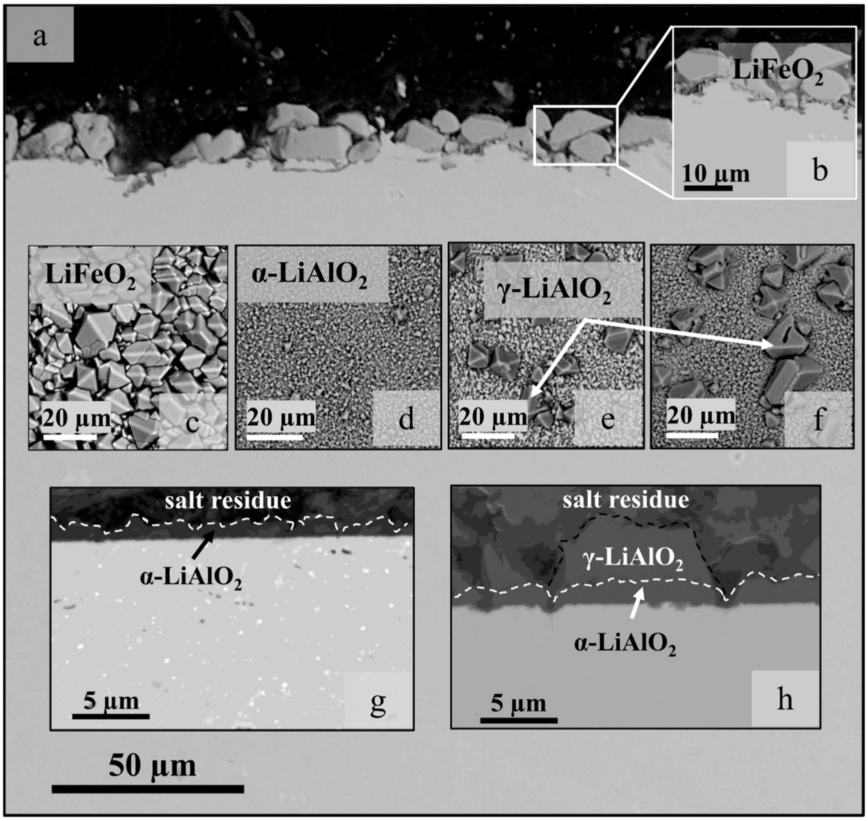

Fig. 7. Top view of Kanthal® EF 100 exposed to alkali carbonate melts at 800 °C, a, b) Cross section after 72 h. Top-view image of c) 72 h, $LiFeO_2$ covers the surface, d) 168 h, only α-$LiAlO_2$ covers the surface, e) 500 h, γ-$LiAlO_2$ crystallites appear, f) 1000 h, γ-$LiAlO_2$ crystallites size increased. Cross-section after g) 168 h, h) 1000 h.

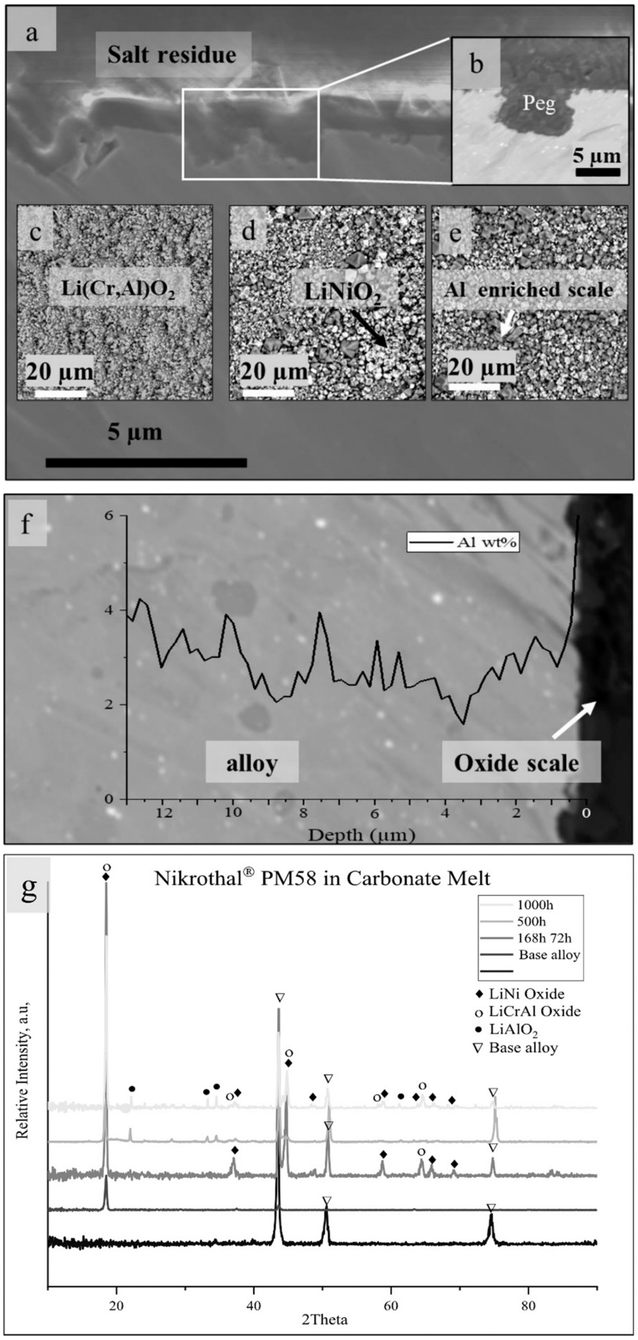

Fig. 9. Nikrothal® PM58 exposed to alkali carbonate melts at 800 °C, Cross-section after a) 1000 h in SEM contrast, b) peg after 1000 h in backscatter contrast. Top-view image after c) 72 h, $Li(Cr,Al)O_2$ covers the surface, d) 500 h, presence of nickel and iron-rich particles, e) 1000 h, Al enriched scale fractions, f) line scan for the suboxide zone after 1000 h, g) XRD patterns for Nikrothal® PM58 after exposure to alkali carbonates in CO_2 at 800 °C for 72 h,168 h, 500 h and 1000 h.

species is interfering or detected on the scale. Every other behaviour has been denominated "deviating" oxidation of alumina forming alloys in contact with alkali carbonates involving transient oxide formation and pegging.

4.1. "Normal" $LiAlO_2$ formation and transformation

"Normal" $LiAlO_2$ formation was observed for the alloys Kanthal® AF, Kanthal® APMT and Kanthal® EF 101. Exposure experiments in alkali carbonates at 800 °C revealed formation of a covering α-$LiAlO_2$ scale after 72 h. This homogeneous α-$LiAlO_2$ scale protects the bulk alloy against internal oxidation and carburisation.

Worth noting, α-$LiAlO_2$ is thermodynamically not favoured at 800 °C [13]; hence it is important to offer an understanding why the α-$LiAlO_2$ scale is present at this temperature and grows with time. At this point, we want to remind the reader of Evans' et al. oxidation mechanism for phase stabilisation under compressive growths stress [17]. α-$LiAlO_2$ has a significantly higher theoretical density compared to the γ-modification. Therefore, the growing α-$LiAlO_2$ scale is able to accommodate not only a higher amount of oxygen but also lithium ions in the same volume compared to γ-$LiAlO_2$ and thereby absorbing growth stresses. From a corrosion control point of view, α-$LiAlO_2$ is the preferential crystal morphology because it forms a dense scale that maintains a slow and gradual oxidation process.

However, in this study, we found the γ-$LiAlO_2$ morphology signal after 168 h in the XRD patterns for all ferritic alumina forming alloys in conjunction with larger faceted crystallites at the surface. γ-$LiAlO_2$ crystallites are free-standing at the melt/oxide interphase and do not experience compressive growth stresses.

The amount of both $LiAlO_2$ modifications increases with time, whereby α-$LiAlO_2$ is the only phase initially, while γ-$LiAlO_2$ takes quickly over, as shown in Fig. 6. Since the formation and growth of α-$LiAlO_2$ depends on the presence of compressive stresses, we, therefore, expect to find a steady-state behaviour of the inner scale. The stress relaxation will define the limiting inner α-scale thickness at the gas/oxide interface into the thermodynamically stable γ-modification. In this study, we have not reached the limiting α-scale thickness yet; however, its scale growth rate already significantly declines after 1000 h, while the γ-crystallites keep growing. Rietveld refinement also confirmed an increasing surface coverage of γ-$LiAlO_2$ with time.

The α-$LiAlO_2$ steady-state thickness is expected to be temperature-dependent. At temperatures below 750 °C, α-$LiAlO_2$ is the thermodynamically dominating morphology and therefore, γ-$LiAlO_2$ nucleation is unexpected.

Due to the fast growth and individual crystallinity, γ-$LiAlO_2$ limits the lifetime of the alloy in the melt in two ways. On the one hand, the absence of the covering α-$LiAlO_2$ scale and consequently poor diffusion barrier increases accessibility of corrosion species to the metal surface. On the other hand, the faster growth of γ-$LiAlO_2$ crystallites accelerates the depletion of aluminium from the alloy eventually compromising the formation of a protective α-$LiAlO_2$ scale.

4.2. "Deviating" $LiAlO_2$ formation and transformation

Two of the alumina forming alloys, Kanthal® EF 100 and Nikrothal® PM58, investigated in this study, have not shown the here called "normal" $LiAlO_2$ scale evolution.

As shown in the results for 800 °C, Kanthal® EF 100 presents with an external lithium ferrite, $LiFeO_2$, after 72 h. After 168 h, the $LiFeO_2$ phase has disappeared, presumably due to dissolution, and a "normal" $LiAlO_2$ scale has formed and remained at least until the end of the experiment. Lacking the beneficial silicon content, Kanthal® EF 100 rapidly grows initially a covering $LiFeO_2$ scale. After reaching a sufficiently high thickness (~8.0 µm after 72 h), oxygen and lithium activities are low enough to nucleate a slow-growing $LiAlO_2$ at the metal/scale interface, decreasing the growth significantly. $LiFeO_2$ is leachable into the melt and has dissolved completely after 168 This $LiAlO_2$ undergoes further α- to γ- transformation as described in the former section on "normal" $LiAlO_2$ formation.

This result is very similar to observations made by comparing the oxidation behaviour of Kanthal® EF 100 and Kanthal® EF 101 in dry air [25].

Even though the chemical composition for both alloys is very similar, differing exclusively in silicon content, Kanthal® EF 101 grows reliably on an aluminium oxide scale in the referenced case in dry air while

Kanthal® EF 100 rapidly grows iron oxide instead [25].

Of note, the newly developed Kanthal® EF 100 and Kanthal® EF 101 have been used in former publications under names “model alloy 198″ and “ model alloy 197″, respectively.

The silicon contribution to the protective alumina scale formation is addressed as 3rd element effect. In our study here, the 3rd element effect of silicon as alloying element extends even beneficially for the reliable formation of α- $LiAlO_2$ in carbonate melts.

Nikrothal® PM58 deviates in another way from all other exposed alumina forming alloys investigated in this study. As austenitic alumina forming alloy, aluminium diffusion towards the metal/scale interface is a priori slower than for the four ferritic alloys [26], as seen in the flat aluminium profile in the suboxide region (Fig. 9.f). As described in Section 4.1. on "normal" $LiAlO_2$ formation, an intact α-$LiAlO_2$ can only be maintained by a steady-state supply of aluminium to the metal/scale interface. A covering α-$LiAlO_2$ scale could not be detected after exposure to alkali carbonates at 800 °C. This result strongly contrasts with an earlier study also undertaken in the same lab revealing that a protective slow-growing scale was formed and sustained at 750 °C for at least 740 h [24]. This observation indicates a strong correlation with the temperature dependence of $LiAlO_2$ phase transition investigated by [13], where the lower limit for γ-$LiAlO_2$ formation was indeed 750 °C.

5. Conclusions

All ferritic alumina forming alloys investigated in this study formed a dense and adherent α-$LiAlO_2$ scale after max. 168 h at 800 °C, fully immersed in alkali carbonates under flowing CO_2. This scale grows slowly and protects the alloy from internal oxidation and carburisation, which are common major corrosion problems for chromia forming high temperature alloys in contact with carbonates or CO_2.

However, the α-$LiAlO_2$ forms initially due to growth stress. On top of the α-$LiAlO_2$ scale, the thermodynamically stable γ-$LiAlO_2$ nucleates and rapidly grows non-protective crystals. Up to 1000 h of exposure, no detrimental aluminium depletion from the alloys was reached. The austenitic alloy Nikrothal® PM58 does not grow the preferable α-$LiAlO_2$ at 800 °C due to the relatively slow diffusion of aluminium from the alloy towards the alloy/melt interface.

CRediT authorship contribution statement

Esraa Hamdy: Conducting exposure experiments, sample analyses, main author of this article. **Michal Strach:** Using Rietveld refinement method, TOPAS V6 software, α/γ-$LiAlO_2$ phase fraction calculations, co-authoring this article. **Johanna Nockert Olovsjö:** Sample material advisor and main project partner for materials supplying at Kanthal, co-authoring this article. **Christine Geers:** Conducting exposure experiments, sample analyses, co-authoring this article.

Declaration of Competing Interest

The authors declare that they have no known competing financial interests or personal relationships that could have appeared to influence the work reported in this paper.

Data Availability

The raw/processed data required to reproduce these findings will be made available upon request. Additional data of a previous publication can be found [23].

Acknowledgements

This work was financially supported by Vinnova within the ALSTEr Project as part of the Jernkontoret initiative Metalliska Material. The Swedish Energy Agency financially supported our efforts within the thermal storage for SOLEL initiative under contract number 44653-1 (Jan-Erik Svensson) and as a partner in the High Temperature Corrosion Competence Centre (Lars-Gunnar Johansson).

References

[1] C. Prieto, S. Fereres, F.J. Ruiz-Cabañas, A. Rodriguez-Sanchez, C. Montero, Carbonate molten salt solar thermal pilot facility: Plant design, commissioning and operation up to 700 °C, Renew. Energy 151 (2020) 528–541.

[2] M. Mehos, C. Turchi, J. Vidal, M. Wagner, Z. Ma, C. Ho, W. Kolb, C. Andraka, A. Kruizenga. Concentrating Solar Power Gen3 Demonstration Roadmap, in, National Renewable Energy Lab, NREL), Golden, CO (United States, 2017.

[3] W. Ding, A. Bonk, T. Bauer, Corrosion behavior of metallic alloys in molten chloride salts for thermal energy storage in concentrated solar power plants: A review, Frontiers of Chemical Science and Engineering (2018) 564–576, https://doi.org/10.1007/s11705-018-1720-0.

[4] M. Liu, N.H. Steven Tay, S. Bell, M. Belusko, R. Jacob, G. Will, W. Saman, F. Bruno, Review on concentrating solar power plants and new developments in high temperature thermal energy storage technologies. Renewable and Sustainable Energy Reviews, Elsevier,, 2016, pp. 1411–1432.

[5] M. Walczak, F. Pineda, Á.G. Fernández, C. Mata-Torres, R.A. Escobar, Materials corrosion for thermal energy storage systems in concentrated solar power plants, Renew. Sustain. Energy Rev. 86 (2018) 22–44.

[6] T.D. Nguyen, J.Q. Zhang, D.J. Young, Microstructures of chromia scales grown in CO_2, Mater. High. Temp. 32 (1–2) (2015) 16–21.

[7] E. Hamdy, J.N. Olovsjö, C. Geers, Perspectives on selected alloys in contact with eutectic melts for thermal storage: nitrates, carbonates and chlorides, Sol. Energy 224 (2021) 1210–1221.

[8] H. Hattendorf, C.G.M. Hermse, R.M. IJzerman, The influence of alloying elements on metal dusting behavior of nickel chromium alloys and their statistical correlation, Mater. Corros. 70 (8) (2019) 1385–1399.

[9] P. Szakálos, M. Lundberg, R. Pettersson, The role of discontinuous precipitation in metal dusting, Mater. Sci. Forum 461–464 (2004) 561–570.

[10] M. Spiegel, P. Biedenkopf, H.J. Grabke, Corrosion of iron base alloys and high alloy steels in the Li2CO3-K2CO3 eutectic mixture, Corros. Sci. 39 (7) (1997) 1193–1210.

[11] H.E. Evans, D.J. Norfolk, T. Swan, Perturbation of parabolic kinetics resulting from the accumulation of stress in protective oxide layers, J. Electrochem. Soc. 125 (1978) 1180–1185.

[12] H.-A. Lehmann, H. Hesselbarth, Zur Kenntnis der Lithiumaluminate. I. Über eine neue Modifikation des LiAlO2, Z. für Anorg. und Allg. Chem. 313 (1–2) (1961) 117–120.

[13] V. Danek, M. Tarniowy, L. Suski, Kinetics of the α → γ phase transformation in LiAlO2 under various atmospheres within the 1073–1173 K temperatures range. J. Mater. Sci. 39 (2004) 2429–2435.

[14] S.J. Heo, B. Hu, M.A. Uddin, A. Aphale, A. Hilmi, C.Y. Yuh, A. Surendranath, P. Singh, Role of exposure atmospheres on particle coarsening and phase transformation of LiAlO2, J. Electrochem. Soc. 164 (8) (2017) H5086–H5092.

[15] A. Aguero, M.C. Garcia, R. Muelas, A. Sanchez, F.J. Perez, D. Duday, M.P. Hierro, C. Gomez, Al slurry coatings for molten carbonate fuel cells separator plates, High Temp. Corros. Prot. Mater. 5 (2001) 759–766, https://doi.org/10.4028/www.scientific.net/MSF.369-372.759.

[16] H.J. Choi, J.J. Lee, S.H. Hyun, H.C. Lim, Phase and microstructural stability of electrolyte matrix materials for molten carbonate, Fuel Cells 10 (4) (2010) 613–618.

[17] H.E. Evans, D.J. Norfolk, T. Swan, Perturbation of parabolic kinetics resulting from the accumulation of stress in protective oxide layers, J. Electrochem. Soc. 125 (7) (1978) 1180–1185.

[18] P. Bouvier, E. Djurado, G. Lucazeau, T. Le Bihan, High-pressure structural evolution of undoped tetragonal nanocrystalline zirconia, Phys. Rev. B 62 (13) (2000) 8731–8737.

[19] W. Harlow, A.C. Lang, B.J. Demaske, S.R. Phillpot, M.L. Taheri, Thickness-dependent stabilization of tetragonal ZrO2 in oxidized zirconium, Scr. Mater. 145 (2018) 95–98.

[20] D.J. Spengler, A.T. Motta, R. Bajaj, J.R. Seidensticker, Z. Cai, Characterization of Zircaloy-4 corrosion films using microbeam synchrotron radiation, J. Nucl. Mater. 464 (C) (2015) 107–118.

[21] K. Momma, F. Izumi, VESTA 3 for three-dimensional visualization of crystal, volumetric and morphology data, J. Appl. Crystallogr. 44 (6) (2011) 1272–1276.

[22] A.-M., Lejus, *Sur la formation à haute température de spinelles non stoechiométriques et de phases dérivées dans plusieurs systèmes d'oxydes à base d'alumine et dans le système alumine-nitrure d'aluminium*. 1964, Masson et Cie: Paris.

[23] E., Hamdy, J.N. Olovsjö, and C. Geers, *Additional data and experimental setups used for the study on alloys in contact to high temperature eutectic melts for thermal storage* 2021: Data in Brief. Revisions submitted.

[24] E., Landberg, et al., *New alumina-forming steels for future energy production with focus on solar power*. 2016: Jernkontoret, Stockholm.

[25] V. Asokan, J. Eklund, S. Bigdeli, T. Jonsson, The influence of Si on the primary protection of lean FeCrAl model alloys in O2 and O2+H2O at 600 °C—A microstructural investigation, Corros. Sci. 179 (2021), 109155.

[26] D.J. Young, in: D.J. Young (Ed.), Chapter 5 - Oxidation of Alloys I: Single Phase Scales, in High Temperature Oxidation and Corrosion of Metals, second ed., Elsevier, 2016, pp. 193–260.